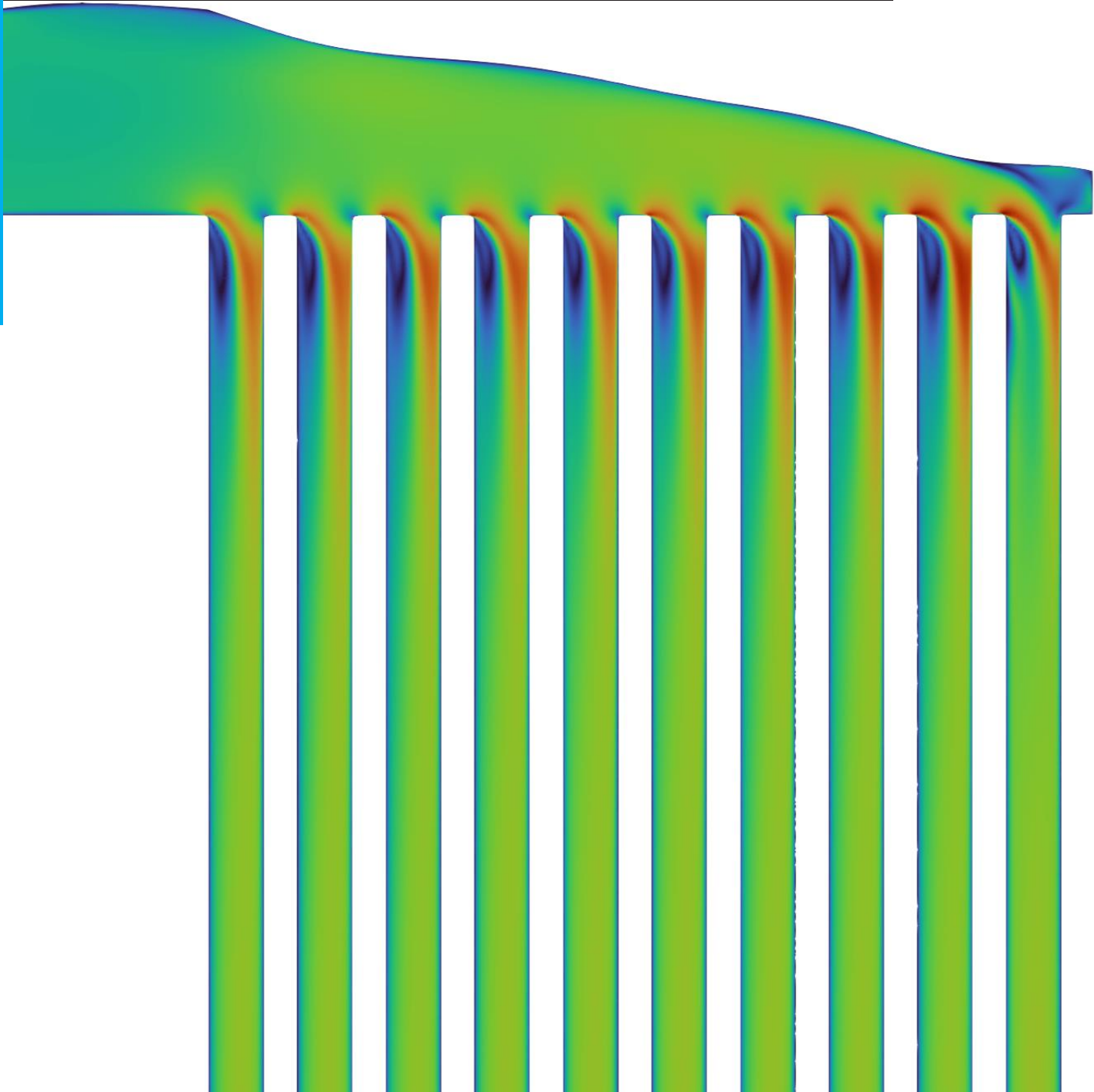


# 3D Shape Optimization of Consecutive Manifolds using Free Form Deformation and Adjoint-Based Methods.

L. van der Mark

Technische Universiteit Delft



# 3D SHAPE OPTIMIZATION OF CONSECUTIVE MANIFOLDS USING FREE FORM DEFORMATION AND ADJOINT-BASED METHODS.

by

**L. van der Mark**

in partial fulfillment of the requirements for the degree of

**Master of Science**  
in Aerospace Engineering

at the Delft University of Technology,  
to be defended publicly on Wednesday March 6, 2024 at 14:00.

Supervisor:	Dr. ir. C.M. DeServi	TU Delft / VITO
	Dr. ir. N. Anand	VITO
Thesis committee:	Dr. ir. M. Pini	TU Delft
	Prof. Dr. K. Hooman	TU Delft

An electronic version of this thesis is available at <http://repository.tudelft.nl/>.

# PREFACE

This work concludes my 7.5-year journey at the TU Delft Faculty of Aerospace Engineering. I look back at this period with great pleasure and pride. It has been a transformative period, and I am immensely grateful to all who have contributed to shaping the person I am today.

I extend my heartfelt gratitude to several individuals who have played pivotal roles along this path. Firstly, I am indebted to Carlo and Nitish for their exceptional guidance and support throughout my thesis. Their mentorship has been invaluable, and I am truly grateful. Next, I express my deepest appreciation to my family and friends for their unwavering support and encouragement. Lastly, I must acknowledge my fiancée, Sabine. Her enduring patience, boundless love, and unwavering support have been my rock throughout this thesis journey. I am profoundly grateful for her presence in my life.

To everyone who has contributed to my growth and development during my time at TU Delft, whether through teaching, motivation, or inspiration, I offer my heartfelt thanks. Your impact has been profound, and I carry your lessons with me as I embark on the next chapter of my journey.

*L. van der Mark  
Delft, March 2024*

# CONTENTS

<b>List of Figures</b>	<b>iii</b>
<b>List of Tables</b>	<b>iv</b>
<b>I Literature Review</b>	<b>1</b>
<b>1 Manifolds</b>	<b>2</b>
1.1 Bifurcating v. Consecutive . . . . .	2
1.2 Dividing v. Combining . . . . .	3
1.3 Parallel, Reverse and Centre flowing manifolds . . . . .	3
<b>2 Design Methods</b>	<b>5</b>
2.1 Design Method by London . . . . .	5
2.1.1 Derivation of the Pressure Distribution in the Combining Manifold . . . . .	5
2.1.2 Derivation of the Shape Equation for Dividing Parallel Flow Manifold . . . . .	6
2.1.3 Derivation of the Shape Equation for Dividing Reverse Flow Manifold. . . . .	7
2.2 Analytical Flow Model . . . . .	7
2.2.1 Derivation of Generalized Second-Order Differential Equation. . . . .	8
2.2.2 Analytical Design Guidelines . . . . .	10
2.3 Discrete Flow Model . . . . .	11
<b>3 Trends in manifold optimisation</b>	<b>13</b>
3.1 Sensitivity of Geometric and Flow Characteristics. . . . .	13
3.1.1 Area Ratio . . . . .	13
3.1.2 Width Ratio . . . . .	14
3.1.3 Aspect Ratio. . . . .	16
3.1.4 Shape . . . . .	16
3.1.5 Reynolds Number . . . . .	18
3.2 Optimised Manifolds. . . . .	19
<b>4 Conclusion</b>	<b>23</b>
<b>II Research Paper</b>	<b>24</b>
<b>Bibliography</b>	<b>69</b>

# LIST OF FIGURES

1.1	Schematic of bifurcating manifold (a) and consecutive manifold (b).[1] . . . . .	2
1.2	Schematic drawing of a dividing manifold (a) and a combining manifold (b). . . . .	3
1.3	Schematic of parallel flow manifold (a), a reverse flow manifold (b), and a centre flowing manifold. . . . .	4
2.1	Control volume used in the derivation of the analytical flow model of Bajura and Jones [2]. . . . .	8
2.2	Equivalent resistive network for a parallel manifold system [3]. . . . .	12
3.1	Flow rate through parallel channels for three different area ratios [4]. . . . .	14
3.2	Pressure coefficient in dividing header for different area ratios [4]. . . . .	14
3.3	Flow uniformity for three different area ratios [5]. . . . .	14
3.4	Geometry used by Choi et al. to analyse the effect of width ratio [6]. . . . .	15
3.5	Flow rate through parallel channels for different width ratios [6]. . . . .	15
3.6	Pressure coefficient for dividing and combining manifold for different width ratios [6].	15
3.7	Normalized flow rate through parallel channels for different width ratios [7]. . . . .	16
3.8	Effect of aspect ratio on flow uniformity based on the results of Kim et al.[8]. . . . .	16
3.9	Three manifold shapes used to compare for performance [9]. . . . .	17
3.10	Flow distribution per channel for constant cross-section manifold with $D_H = 0.7mm$ [10]. . . . .	17
3.11	Flow distribution per channel for tapered manifold with $D_H = 0.7mm$ [10]. . . . .	17
3.12	Tapering methods used by Tong et al.[11]. . . . .	18
3.13	Mass flow distribution for three different Reynolds numbers in a manifold with an aspect ratio of 8 and a width ratio of 4 [6]. . . . .	19
3.14	Results parametric study of Yang et al.[12]. . . . .	19
3.15	Optimal shapes for different channel widths and the number of channels [3]. . . . .	20
3.16	Optimised shapes from Jackson et al.[13]. . . . .	20
3.17	Optimisation procedure used by Kim [14]. . . . .	21
3.18	Results obtained from optimisation procedure performed by Kim [14]. . . . .	22

# LIST OF TABLES

2.1	Nondimensional values used by Bajura and Jones [2]. . . . .	9
2.2	Parameters for Equation 2.24 as given by Bajura and Jones [2]. . . . .	9

# I

## LITERATURE REVIEW

# 1

## MANIFOLDS

Manifolds are devices which are used to either divide a flow into several smaller flows or combine several small flows into one larger flow. Manifolds come in several different shapes and can be used for a lot of different use cases, some of these use cases include engines, fuel cells, and heat exchangers. This section will first discuss the difference between bifurcating and consecutive manifolds. Then the difference between dividing and combining manifolds is discussed. Finally, the difference between parallel and reverse flow manifolds is discussed.

### 1.1. BIFURCATING V. CONSECUTIVE

There are two main form factors of manifolds that can be chosen during a design process, that is the bifurcating or consecutive manifold. The bifurcating manifold is shaped such that the flow is divided into two equal streams at each stage until the required amount of smaller streams is achieved, or vice-versa for a combining manifold, see [Figure 1.1a](#). The consecutive manifold is shaped such that the flow is divided into the amount of required smaller streams in one stage or combined at once to form the larger stream, see [Figure 1.1b](#).

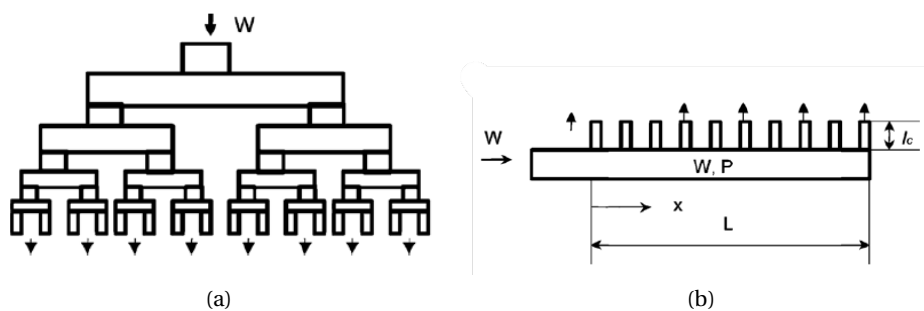


Figure 1.1: Schematic of bifurcating manifold (a) and consecutive manifold (b).[\[1\]](#)

Liu et al. [\[15\]](#) performed several experimental studies on different designs of bifurcating manifolds. From their results, it can be concluded that in general bifurcating manifolds have a very good flow uniformity over all channels. Furthermore, Amador et al. [\[16\]](#) showed that flow uniformity in bifurcating manifolds is not dependent on the flow rate for large Reynolds numbers. However, as both Amador et al. [\[16\]](#) and Wang [\[1\]](#) point out, the bifurcating manifold size and pressure drop both become larger with an increasing number of channels. This causes the bifurcating manifold to be inconvenient for a lot of use cases.

The consecutive manifold on the other hand is commonly used due to its simplicity and smaller form. However, the main disadvantage of the consecutive manifold is its worse performance with respect to flow uniformity [1]. Several approaches have been developed over the years to achieve flow uniformity, more information about these methods will be given in the next section. In this research, a consecutive manifold design will be considered as this is the most commonly used design.

## 1.2. DIVIDING V. COMBINING

There are two main types of manifolds, that is, dividing and combining manifolds, see Figure 1.2. The dividing manifold also called the inlet manifold, is the manifold where the main fluid flow is divided into several channel flows. The combining manifold also called the outlet manifold, is the manifold where the channel flows are combined into a main fluid flow.

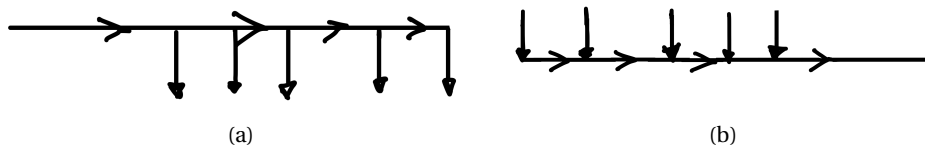


Figure 1.2: Schematic drawing of a dividing manifold (a) and a combining manifold (b).

For a dividing manifold, the main fluid stream will continuously lose mass flow along the length of the manifold due to the lateral channels. The loss of mass flow will cause a deceleration of the fluid flow if the cross-section of the manifold is constant. If friction effects are small in the manifold, the pressure will rise along the length due to the loss of flow. However, friction effects could cause the pressure to drop, hence a set of flow parameters could be chosen such that the pressure in the manifold remains uniform [2]. In the combining manifold the exact opposite is observed, i.e., mass flow is added to the manifold through the lateral channels. This causes the flow to accelerate in the direction of the flow, causing a pressure drop in the manifold. Moreover, the pressure drops due to friction effects present in the manifold [2].

## 1.3. PARALLEL, REVERSE AND CENTRE FLOWING MANIFOLDS

The combining and dividing manifold are often combined in sets, these sets can have different flow patterns such as parallel, reverse or centre flow. In the parallel manifold the incoming flow and outgoing flow have the same flow direction, see Figure 1.3a. In the reverse flow the incoming and outgoing flow have opposite directions, Figure 1.3b, and in the centre flow the flow comes into the manifold centre and leaves in the centre, see Figure 1.3c. In literature sometimes letters are given to these flow configurations where the letters represent the flow pattern; parallel manifolds are coupled with the Z, reverse flow manifolds are coupled with the U and centre flowing manifolds with the I[17]. Some papers also make a distinction between the placement of the inlet and outlet to the manifold, that is if the in- and outlet are in line with the manifold or normal to the manifold [18].

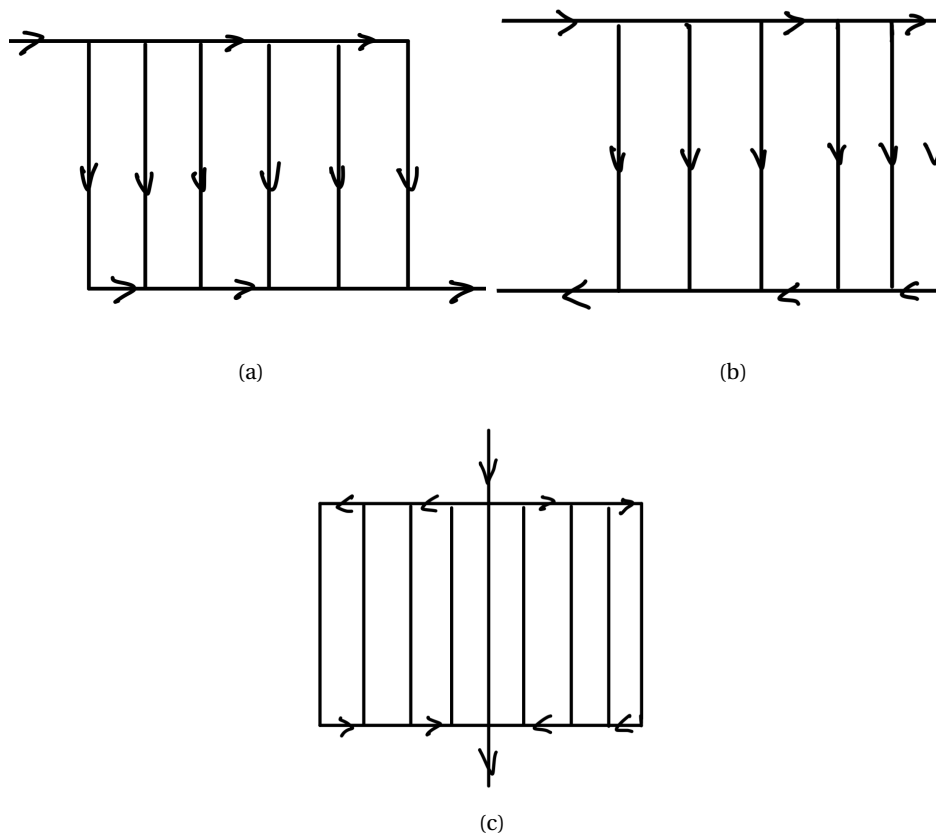


Figure 1.3: Schematic of parallel flow manifold (a), a reverse flow manifold (b), and a centre flowing manifold.

Xia et al. [19] performed numerical simulations on parallel, reverse and centre flow manifolds, with rectangular cross-sections of constant area. These simulations show that for such cases the parallel flowing manifold results in the worst mass-flow distributions across the parallel channels. Furthermore, Anbumeenakshi and Thansekhar [20] demonstrated through experiments that positioning the inlet at a  $90^\circ$  angle from the flow direction in the manifold leads to a less prominent jet flow effect, consequently resulting in improved mass flow distribution. Combining these results, it can be concluded that a parallel flow manifold with the in and outlet inline with the flow will result in the worst mass flow distribution.

# 2

## DESIGN METHODS

When designing a manifold two different objectives could be taken into account, to minimise the non-uniformity in the heat exchanger (HEX) core/ lateral channels or to minimise the pressure drop over the manifold [21]. To reach these objectives several design methods/ guidelines for manifold sizing have been formulated over the years. In this section first the design method of London et al. [22] will be discussed. Then the analytical method set up by Bajura and Jones [2], including the more recent revision by Yang et al. [12] will be discussed. Finally, the discrete design method as formulated by Wang and Wang [23] and Pan et al. [3] will be discussed.

### 2.1. DESIGN METHOD BY LONDON

The design method by London et al. [22] uses Bernoulli's equation to derive a pressure profile in the dividing manifold that matches the profile of the combining manifold. Then the required shape to achieve this pressure distribution is derived. These derivations are performed for both a parallel and centre flow manifold system. This section will discuss the derivation for both these systems. Finally, both derivations are based on the set of assumptions and conditions listed below.

#### **Assumptions:**

1. The fluid flow in both headers has a separate constant density. That is, the flow in each manifold is incompressible, but the density may change in the HEX core.
2. The inlet manifold velocity profile is uniform at  $x = 0$ , and a function of  $x$  only in the rest of the manifold.
3. The combining manifold velocity profile is two-dimensional.
4. For both the dividing and combining manifold the pressure is assumed to be a function of  $x$  only.
5. The flow in the manifolds is inviscid.

#### **Conditions:**

1. The area of the combining manifold is constant along the length of the manifold.
2. The mass flow through the HEX core is uniform.
3. To achieve condition 2 the pressure profile of the dividing manifold should match the pressure profile of the combining manifold.

#### 2.1.1. DERIVATION OF THE PRESSURE DISTRIBUTION IN THE COMBINING MANIFOLD

As mentioned above, to determine the shape of the dividing manifold the pressure profile in the dividing manifold has to match the pressure profile in the combining manifold. To find the pressure profile in the combining manifold, first, the Bernoulli equation for an incompressible flow should

be derived, as in Equation 2.1. Where  $P(x)$  is the pressure at any point  $x$  along the streamline and  $P(t)$  the pressure at the origin of the streamline in the combining manifold. Moreover,  $u$  and  $v$  are the velocities in  $x$  and  $y$ -direction respectively;  $v_m$  is the flow velocity in the HEX core;  $\rho_o$  is the density in the combining manifold and  $g_c$  the gravitational constant.

$$P(x) + \frac{\rho_o}{2g} (u^2 + v^2) = P(t) + \frac{\rho_o}{2g} v_m^2 \quad (2.1)$$

From the continuity equation, applied to the stream tube bounded by the streamline Equation 2.2 can be derived.

$$-(udy) = v_m dt \quad (2.2)$$

Substituting Equation 2.2 into Equation 2.1 Equation 2.3 is obtained.

$$-dy = v_m \sqrt{\frac{\rho_o}{2g}} \frac{dt}{\sqrt{P(t) - P(x)}} \quad (2.3)$$

Heyda [], integrated Equation 2.3 for several wall contours of the combining manifold. The result for the assumed 'box'-shape manifold is given in Equation 2.4. This is the obtained pressure distribution in the combining manifold and can be used for both the parallel and reverse flow manifold systems. Where  $u_{o,ave}$  is the average flow velocity in the outlet;  $x$  is the coordinate position along the length of the manifold;  $L$  is the length of the manifold;  $h_o$  is the velocity head of the outlet manifold and  $X$  is the normalized position along the manifold.

$$P(0) - P(x) = \frac{\pi^2}{4} \rho_o \frac{u_{o,ave}^2}{2g} \left(\frac{x}{L}\right)^2 = \frac{\pi^2}{4} h_o X^2 \quad (2.4)$$

### 2.1.2. DERIVATION OF THE SHAPE EQUATION FOR DIVIDING PARALLEL FLOW MANIFOLD

Using the resulting pressure profile of the combining manifold and matching this to the pressure profile of the combining manifold (as in Equation 2.5), Equation 2.6 is obtained.

$$P_i - P(x) = \frac{\rho_i}{2g} (u^2 - u_i^2) \quad (2.5) \quad P_i - P(x) = \frac{\pi^2}{4} h_o X^2 \quad (2.6)$$

Then from continuity the relations as presented in Equation 2.7 can be derived. Where  $u_i$  is the flow velocity at the inlet;  $z_i$  is the height of the manifold at the inlet;  $u$  the flow velocity in the manifold;  $z_{wall}$  the height of the manifold at any point  $x$ .

$$\begin{aligned} u_i z_i &= u z_{wall} + v_m x \rightarrow u z_{wall} = v_m (L - x) \\ u_i z_i \rho_i &= u_{o,ave} y_o \rho_o \end{aligned} \quad (2.7)$$

Combining Equation 2.5, Equation 2.6 and Equation 2.7 as shown below the shape equation presented in Equation 2.8 is obtained.

$$\begin{aligned}
\frac{\rho_i}{2g} (u^2 - u_i^2) &= \frac{\pi^2}{4} h_o X^2 \\
\frac{\rho_i}{2g} (u^2 - u_i^2) &= \frac{\pi^2}{4} \frac{\rho_o u_{0,ave}^2}{2g} X^2 \\
(u^2 - u_i^2) &= u_{0,ave}^2 \frac{\rho_o \pi^2}{\rho_i 4} X^2 \\
\left( \left( \frac{v_m L}{z_{wall}} (1-X) \right)^2 - u_i^2 \right) &= \left( \frac{u_i z_i \rho_i}{y_o \rho_o} \right)^2 \frac{\rho_o \pi^2}{\rho_i 4} X^2 \\
\left( \frac{y_o}{u_i z_i} \right)^2 \left( \left( \frac{v_m L}{z_{wall}} (1-X) \right)^2 - u_i^2 \right) &= \frac{\rho_i \pi^2}{\rho_o 4} X^2 \\
\frac{(1-X)^2}{Z^2} - \left( \frac{y_o}{z_i} \right)^2 &= \frac{\rho_i \pi^2}{\rho_o 4} X^2 \\
Z^2 &= \frac{(1-X)^2}{\frac{\rho_i \pi^2}{\rho_o 4} X^2 + \left( \frac{y_o}{z_i} \right)^2} \tag{2.8}
\end{aligned}$$

### 2.1.3. DERIVATION OF THE SHAPE EQUATION FOR DIVIDING REVERSE FLOW MANIFOLD

The derivation of the shape function for the dividing reverse flow manifold is for a large part similar to the previous derivation. However, due to the change in coordinate systems, due to the reverse flow configuration Equation 2.6 becomes Equation 2.9. It can quite easily be shown how this change results in the shape function presented in Equation 2.10.

$$P(x) - P_i = \frac{\pi^2}{4} h_o [1 - (1-X)^2] \tag{2.9} \quad Z^2 = \frac{(1-X)^2}{\left( \frac{y_o}{z_i} \right)^2 - \frac{\rho_i \pi^2}{\rho_o 4} [1 - (1-X)^2]} \tag{2.10}$$

This change in the shape equation results in the option of imaginary values for  $Z$ . Hence the condition in Equation 2.11 has to be satisfied.

$$\left( \frac{y_o}{z_i} \right)^2 \geq \frac{\rho_i \pi^2}{\rho_o 4} [1 - (1-X)^2] \tag{2.11}$$

The condition above implies that multiple shapes for the dividing manifold would be possible. However, the maximum of the  $z_i/y_o$  fraction should be used, as smaller values will cause more losses in the system. This implies that the shape of the dividing header has a constant cross-section, as given by Equation 2.12.

$$Z^2 = \frac{4}{\pi^2} \frac{\rho_o}{\rho_i} \tag{2.12}$$

## 2.2. ANALYTICAL FLOW MODEL

One of the main issues with using a Bernoulli-based design method, as explained above, is the number of assumptions that have to be made to derive these relatively simple equations. However, if these assumptions are not made the choice of streamline becomes ambiguous [2]. A method to avoid this ambiguity is to perform an analytical control volume analysis of the flow in the manifold. Bajura and Jones [2] performed such an analysis, resulting in a generalized second-order differential equation of the normalized mass flow rate. Yang et al. [12] used this second-order differential equation to set up design guidelines to achieve optimal mass flow distribution in a dividing manifold. This section will first discuss the derivation of the generalized second-order differential equation and then discuss how the design guidelines were achieved. The assumptions made by Bajura and

Jones [2] and Yang et al. [12] are listed below.

**Assumptions:**

1. It is assumed that the flow is not completely turning 90° when entering the flow channels, hence resulting in an x and y component of the channel flow.
2. The cross-sectional area of all channels is assumed constant along the dividing manifold.
3. The cross-sectional area of the manifold is assumed constant.
4. It is assumed that the lateral channels are evenly distributed along the channel.

**2.2.1. DERIVATION OF GENERALIZED SECOND-ORDER DIFFERENTIAL EQUATION**

In Figure 2.1 the control volume used in the derivation can be seen. For this control volume, it can be shown that the momentum equation can be written as in Equation 2.13 [2].

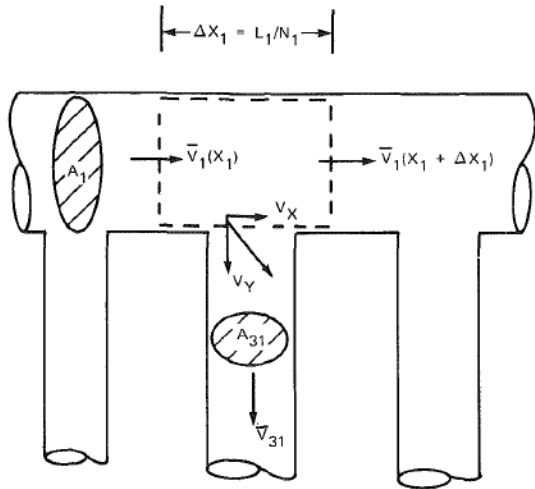
$$\bar{V}_{31} A_{31} = -A_1 \frac{d\bar{V}_1}{dx_1} \frac{L_1}{N_1} \quad (2.13)$$


Figure 2.1: Control volume used in the derivation of the analytical flow model of Bajura and Jones [2].

Moreover, an axial flow momentum correction factor as in Equation 2.14; a lateral flow momentum correction factor as in Equation 2.15; an overall momentum correction factor as in Equation 2.16 and the wall shear stress as in Equation 2.17 can be defined.

$$\beta_{d,1} = \frac{1}{\bar{V}_1^2 A_1} \int_{A_1} V_1^2(A_1) dA_1 \quad (2.14) \quad \gamma_{d,1} = \frac{1}{\bar{V}_1 \bar{V}_{31} A_{31}} \int_{A_{31}} V_x(A_{31}) V_y(A_{31}) dA_{31} \quad (2.15)$$

$$\theta_1 = 2\beta_{d,1} - \gamma_{d,1} \quad (2.16) \quad T_1 = \frac{f_1 \rho \bar{V}_1^2}{8} \quad (2.17)$$

Then the momentum equation for the control volume analysis, expressed using the terms presented above, can be written as in Equation 2.18. Where  $\bar{P}$  is the average pressure over the cross-sectional area at location  $x$ ;  $f$  the Moody friction factor [24];  $\mathcal{P}$  the perimeter of the manifold;  $A_1$  the area of the manifold;  $\beta$  the axial flow momentum correction factor;  $\theta$  the overall momentum correction factor; and  $\bar{V}$  the average flow speed in the manifold.

$$\frac{1}{\rho} \frac{d\bar{P}_1}{dx_1} + \left( \frac{f_1 \mathcal{P}_1}{8A_1} + \frac{d\beta_1}{dx_1} \right) \bar{V}_1^2 + \theta_1 \bar{V}_1 \frac{d\bar{V}_1}{dx_1} = 0 \quad (2.18)$$

Similarly, the momentum equation for parallel flow combining manifold can be derived, resulting in Equation 2.19. Where the subscript 2 represents the values for the combining manifold.

$$\frac{1}{\rho} \frac{d\bar{P}_2}{dx_2} + \left( \frac{f_2 \mathcal{P}_2}{8A_2} + \frac{d\beta_1}{dx_2} \right) \bar{V}_2^2 + \theta_2 \bar{V}_2 \frac{d\bar{V}_2}{dx_2} = 0 \quad (2.19)$$

Through a control volume analysis over the length of an entire lateral channel, it can be shown that the velocity gradient  $d\bar{V}_1/dx_1$  can be obtained through Equation 2.20. Where  $H$  is the lateral flow resistance coefficient.

$$\frac{d\bar{V}_1}{dx_1} = -\frac{N_1 A_{31}}{A_1 L_1} \sqrt{\frac{2}{\rho H}} \sqrt{\Delta\bar{P}_{12}} \quad (2.20)$$

Then subtracting the momentum equation of the combining manifold, Equation 2.19, from the moment equation of the dividing manifold, Equation 2.18, and nondimensionalizing using Table 2.1, Equation 2.21 is obtained. Moreover, nondimensionalizing Equation 2.20 results in Equation 2.22.

Table 2.1: Nondimensional values used by Bajura and Jones [2].

$$\begin{array}{l} x = x_1/L_1 = x_2/L_2 \quad Q = \bar{V}_1 A_1 / Q_0 \\ V = \bar{V}_1 / V_{10} \quad \Delta P = \Delta\bar{P}_{12} / \rho \bar{V}_{10}^2 \end{array}$$

$$\frac{d(\Delta P)}{dx} = -\left[ \frac{f_1 L_1 \mathcal{P}_1}{8A_1} - \frac{f_2 L_2 \mathcal{P}_2}{8A_2} \left(\frac{A_1}{A_2}\right)^2 + \frac{d\beta_1}{dx} - \frac{d\beta_2}{dx} \right] V^2 - \left[ \theta_1 - \theta_2 \left(\frac{A_1}{A_2}\right)^2 \right] V \frac{dV}{dx} \quad (2.21)$$

$$\frac{d\bar{V}}{dx} = -\frac{N_1 A_{31}}{A_1} \sqrt{\frac{2}{H}} \sqrt{\Delta\bar{P}} \quad (2.22)$$

Then combining Equation 2.21 and Equation 2.22 a second-order differential equation can be obtained for the dimensionless volumetric flow rate, as presented in Equation 2.23.

$$\frac{H}{A_r^2} Q' Q'' + \left[ \frac{d\beta_1}{dx} - \frac{d\beta_2}{dx} \right] Q^2 + \left[ \frac{f_1 L_1 \mathcal{P}_1}{8A_1} - \frac{f_2 L_2 \mathcal{P}_2}{8A_2} \left(\frac{A_1}{A_2}\right)^2 \right] Q^2 + \left[ \theta_1 - \theta_2 \left(\frac{A_1}{A_2}\right)^2 \right] Q Q' = 0 \quad (2.23)$$

Bajura and Jones [2] generalized the obtained second-order differential equation to the form of Equation 2.24. Where the parameters  $\phi_1$ ,  $\phi_2$ ,  $M_1$  and  $M_2$  are listed in Table 2.2 for the different manifold types. For all possible manifold configurations the boundary conditions are the same, see Equation 2.25. That is, at the start of the manifold ( $x=0$ ) the normalized mass flow is equal to one and at the end of the manifold ( $x=1$ ) the velocity, and therefore the normalized mass flow, is zero.

$$Q' Q'' + \phi_1 Q^2 + 2\phi_2 Q + M_1 Q Q' + M_2 Q' = \phi_2 \quad (2.24)$$

$$\begin{array}{l} Q(x=0) = 1 \\ Q(x=1) = 0 \end{array} \quad (2.25)$$

Table 2.2: Parameters for Equation 2.24 as given by Bajura and Jones [2].

Parameters	Dividing Manifold	Combining Manifold	Reverse Flow Manifold	Parallel Flow Manifold
$\phi_1$	$\frac{A_r^2}{H} \frac{f_1 L_1}{2D_1}$	$\frac{A_r^2}{H} \frac{f_2 L_2}{2D_2}$	$\frac{A_r^2}{H} \left[ \frac{f_1 L_1}{2D_1} + \frac{f_2 L_2}{2D_2} \left(\frac{D_1}{D_2}\right)^4 \right]$	$\frac{A_r^2}{H} \left[ \frac{f_1 L_1}{2D_1} - \frac{f_2 L_2}{2D_2} \left(\frac{D_1}{D_2}\right)^4 \right]$
$\phi_2$	0	0	0	$\frac{A_r^2}{H} \left[ \frac{f_2 L_2}{2D_2} \left(\frac{D_1}{D_2}\right)^4 \right]$
$M_1$	$\frac{A_r^2}{H} \theta_1$	$\frac{-A_r^2}{H} \theta_2$	$\frac{A_r^2}{H} \left[ \theta_1 - \theta_2 \left(\frac{D_1}{D_2}\right)^4 \right]$	$\frac{A_r^2}{H} \left[ \theta_1 - \theta_2 \left(\frac{D_1}{D_2}\right)^4 \right]$
$M_2$	0	0	0	$\frac{A_r^2}{H} \theta_2 \left(\frac{D_1}{D_2}\right)^4$

### 2.2.2. ANALYTICAL DESIGN GUIDELINES

The form of the analytical solution presented above does not yet allow for an easy design method of manifold systems. Yang et al. [12] derived an algebraic solution to the differential equation of a dividing manifold. Then the solution was used to analyze several manifold designs to define a guideline for the best mass flow distribution within the scope of the assumptions.

Implementing the correct parameters in the generalized differential equation for a dividing manifold yields Equation 2.26. Yang et al. [12] rewrite this as Equation 2.27, where  $\alpha$  is defined as Equation 2.28 and  $\beta$  as Equation 2.29.

$$Q'Q'' + \frac{A_r^2 fL}{H 2D} Q^2 + \frac{(1-\gamma_d)A_r^2}{H} QQ' = 0 \quad (2.26) \quad \frac{d}{dx} \left[ \left( \frac{dQ}{dx} \right)^2 + \beta^2 Q^2 \right] + \alpha^2 Q^2 = 0 \quad (2.27)$$

$$\alpha = \left( \frac{A_r^2 fL}{2DH} \right)^{1/2} \quad (2.28) \quad \beta = \left( \frac{(1-\gamma_d)A_r^2}{H} \right)^{1/2} \quad (2.29)$$

The method to obtain  $Q'$ , i.e., the change of normalized volumetric flow rate through the manifold. For more information on the derivation of these equations the reader is referred to the paper of Yang et al. [12]. To find the value of  $Q'$  Equation 2.30 is used.

$$Q' = Q'(0) \exp [K(R) - K(1/Q'(0))] \quad (2.30)$$

The first step solving for Equation 2.30 is to find  $J(0)$  in Equation 2.31 using Equation 2.32.

$$x = J(R) - J(0) + \beta \quad (2.31)$$

$$J(R) = \frac{2}{\gamma} \left\{ \ln \left[ R + \frac{2}{3\gamma} - (A+B) \right]^C + \ln \left[ R^2 + \left( \frac{4}{3\gamma} + A+B \right) R + \frac{4}{9\gamma^2 + (A+B)\frac{2}{3\gamma}} A^2 + B^2 - AB \right]^{-C/2} \right. \\ \left. - \frac{\sqrt{3}(A+B)C}{A_B} \arctan \left[ \frac{2}{\sqrt{3}(A-B)} R + \frac{2}{\sqrt{3}(A-B)} \left( \frac{2}{3\gamma} + \frac{A+B}{2} \right) \right] + \ln \left[ \frac{\sqrt{3}(A-B)}{2} \right]^C \right\} \quad (2.32)$$

Using the results of  $J(0)$  and taking  $x = 0$ , Equation 2.31 and Equation 2.32 can be combined to find the value of  $R(x=0)$ . Then, from the definition of  $R$ , Equation 2.33 can be obtained. Using this result and Equation 2.34,  $K(1/Q'(0))$  is obtained.

$$R(x=0) = \frac{1}{Q'(0)} \quad (2.33)$$

$$K(R) = \ln \left[ R + \frac{2}{3\gamma} - (A+B) \right]^{-2D/\gamma} + \ln \left[ \frac{\sqrt{3}(A-B)}{2} \right]^{1+2D/\gamma} \\ + \ln \left[ R^2 + \left( \frac{4}{3\gamma} + A+B \right) R + \frac{4}{9\gamma^2} + \frac{2}{3\gamma} (A+B) + A^2 + B^2 - AB \right]^{D/\gamma-1/2} \\ + \frac{1}{\sqrt{3}(A-B)} \left[ \frac{2}{3} + \frac{\gamma}{2} (A+B) + 3D(A+B) \right] \arctan \left[ \frac{2}{\sqrt{3}(A-B)} \left( R + \frac{2}{3\gamma} + \frac{A+B}{2} \right) \right] \quad (2.34)$$

Know  $Q'$  in Equation 2.30 can be found, by finding the corresponding  $J(R)$  for a given  $x$ . Then using Equation 2.32 can be used to find  $R$ , which can be used to find  $K(R)$ . Finally the parameters  $A$ ,  $B$ ,  $C$  and  $D$  in Equation 2.32 and Equation 2.34 can be found using Equation 2.35, where  $\gamma = \frac{\alpha^2}{\beta^3}$ .

$$\begin{aligned}
A &= \sqrt[3]{-\frac{8}{27} \frac{1}{\gamma^2} - \frac{1}{\gamma} + \left(\frac{16}{27} \frac{1}{\gamma^4} + \frac{1}{\gamma^2}\right)^{1/2}} \\
B &= \sqrt[3]{-\frac{8}{27} \frac{1}{\gamma^2} - \frac{1}{\gamma} - \left(\frac{16}{27} \frac{1}{\gamma^4} + \frac{1}{\gamma^2}\right)^{1/2}} \\
C &= \frac{1}{3(A^2 + B^2 + AB)} \\
D &= \frac{\gamma}{2} \left[ (A+B)^2 + \frac{2}{3\gamma}(A+B) - \frac{8}{9\gamma^2} \right] C
\end{aligned} \tag{2.35}$$

The method discussed above was used to calculate the theoretical mass flow distributions of several design configurations. From this analysis, it was found that for a dividing manifold design a  $\gamma=1.44$  results in an optimal design. More information on the results of this analysis can be found in [section 3.2](#).

### 2.3. DISCRETE FLOW MODEL

The discrete flow model is comparable to the analytical flow model, as the main goal is to solve the second-order differential equation of the volume flow in a manifold. However, instead of solving the differential equation in one step, as done by Yang et al. [12], the discrete method divides the manifold into equal control volumes and solves each control volume step-by-step [23].

Two main approaches to solving the flow conditions of the separate pieces are described in the literature. The first approach is to find the hydro- and thermodynamic properties of the flow through existing relations between these properties, with a combination of analytical equations as described by Wang and Wang [23]. The second method is to replace the divisions of the manifold and lateral channels with an equivalent resistive network, as described by [3]. The latter will be discussed in more detail in this subsection, due to the relative ease of use. It must however be noted that this particular implementation is for microchannel designs. Hence due to particular assumptions which can be made for such design, the method becomes much simpler. However, it is believed that the basic principles of the method can also be applied to larger-scale problems. Moreover, the first method has a lot in common with the method of [12], however, becomes more tedious and difficult for large problems. The assumptions used in the method are listed below.

#### Assumptions:

1. The flow is considered laminar.
2. The flow is considered to be incompressible.
3. Local resistances are ignored.

The first step in the design procedure is dividing the manifold system into equivalent flow resistances and flow rates, as in [Figure 2.2](#). The flow resistance for each section can be found through Ohm's law, as in [Equation 2.36](#). Where the resistance ( $R$ ) is defined as [Equation 2.37](#). Where  $L$  is the manifold length;  $\mu$  is the viscosity;  $\lambda_{NC}$  is the non-circular coefficient;  $D_h$  the hydraulic diameter and  $A$  the cross-sectional area of the tube at this location.

From [Figure 2.2](#) it can be seen that the system exists out of  $N-1$  lateral channels. From this, it can be shown that  $N-1$  equations of the form presented in [Equation 2.38](#) can be expressed.

$$\Delta P = RQ \quad (2.36)$$

$$R = \frac{32\mu L \lambda_{NC}}{D_h^2 A} \quad (2.37)$$

$$\begin{aligned} R_{in}(j)Q_{in}(j) + R_c(j)Q_c(j) = \\ R_c(j-1)Q_c(j-1) + R_{out}(j-1)Q_{out}(j-1) \end{aligned} \quad (2.38)$$

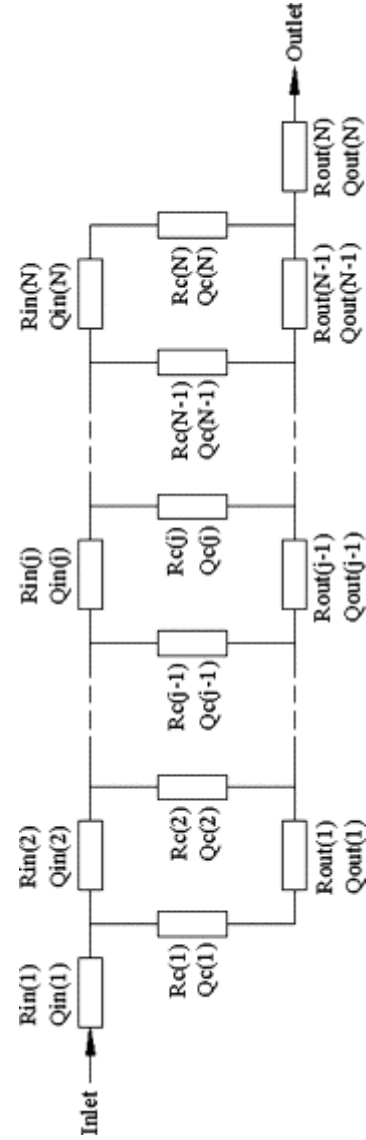


Figure 2.2: Equivalent resistive network for a parallel manifold system [3].

Furthermore, the conditions as presented in Equation 2.39 can be defined for the dividing manifold. Similarly, the conditions in the outlet manifold can be defined as in Equation 2.40. Assuming the dimensions of the manifolds and channels are known, the equivalent resistance scheme can be solved for as there is an equal number of equations and unknowns.

$$Q_{in}(j) = Q_c(j) + Q_{in}(j+1)$$

$$Q_{in}(1) = Q_T$$

$$Q_{in}(N) = Q_c(N)$$

(2.39)

$$Q_{out}(j) = Q_c(j) + Q_{out}(j-1)$$

$$Q_{out}(N) = Q_T$$

(2.40)

# 3

## TRENDS IN MANIFOLD OPTIMISATION

In the previous section, three different design methods have been discussed which have been thoroughly researched over the past 50 years. However, it has not yet been discussed how these design methods are currently used to optimise the manifold design. As mentioned before, the main objective of optimising the manifold's design is to achieve uniform flow through all parallel channels. Secondary to a uniform flow is the minimisation of the pressure drop over the manifold, as this will usually be fully accounted for as a loss [21]. In this section, first, the sensitivities of several geometrical parameters in the manifold design with respect to flow uniformity and pressure drop will be discussed. Secondly, the sensitivities of the Reynolds number will be discussed. Finally, recent works with respect to shape optimisation of manifolds will be discussed.

### 3.1. SENSITIVITY OF GEOMETRIC AND FLOW CHARACTERISTICS

Here, the effect of the geometrical characteristics of the manifold design with respect to flow uniformity and pressure drop will be discussed. First, the area ratio will be discussed, which is the ratio of the total cross-sectional area of all parallel channels to the cross-sectional area of the manifold, see Equation 3.1. Where  $n$  is the number of channels;  $A_c$  is the cross-sectional area of the channels and  $A_m$  is the cross-sectional area of the manifold. Then the effect of the width ratio will be discussed, which is the ratio of the combining manifold width to the dividing manifold width, see Equation 3.2. Where  $W_{m,c}$  is the width of the combining manifold and  $W_{m,d}$  is the width of the dividing manifold. After which the effect of the aspect ratio of the manifold is discussed, which is defined as the manifold width over the manifold length, see Equation 3.3.

$$R_{\text{area}} = \frac{nA_c}{A_m} \quad (3.1) \quad R_{\text{width}} = \frac{W_{m,c}}{W_{m,d}} \quad (3.2) \quad R_{\text{aspect}} = \frac{W_{m,d}}{L_m} \quad (3.3)$$

#### 3.1.1. AREA RATIO

Choi et al. [4] researched the effect of the area ratio for parallel flow manifolds in cooling modules. In their research, they performed a numerical simulation for an area ratio of 4, 8 and 16, with an inlet Reynolds ( $Re$ ) number of 50. Choi et al. [4] found that flow uniformity increase with a decreasing area ratio, see Figure 3.1. Moreover, they found that the pressure drop over the manifold increases with an increasing area ratio, see Figure 3.2. The rise in pressure for an area ratio of 4 and 8 (near the end of the manifold) is dedicated to the momentum effect being dominant over the friction effect, as discussed in section 1.2 [4].

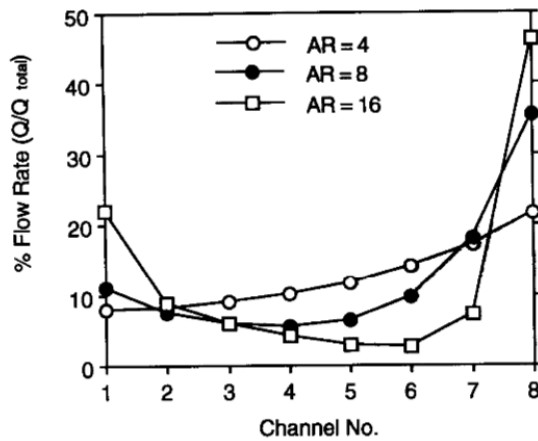


Figure 3.1: Flow rate through parallel channels for three different are ratios [4].

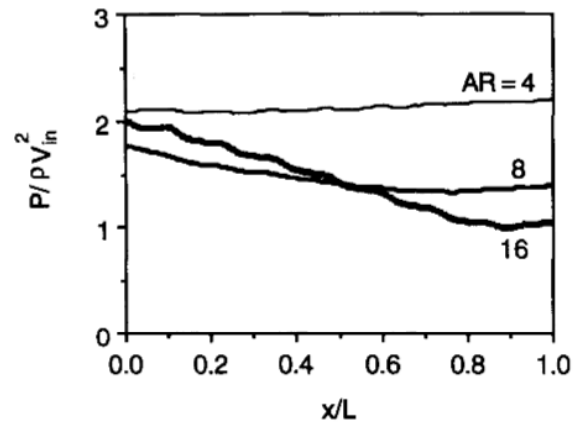


Figure 3.2: Pressure coefficient in dividing header for different area ratios [4].

Jiang et al. [5] performed a similar research in which they experimented with the flow discharge of 5 parallel channels for a dividing manifold. However, the setup used for this experiment has an order of magnitude larger dimensions and  $Re$  numbers between  $50e^3$  and  $200e^3$ . Moreover, the area ratios with which these tests were performed are between 2.81 and 0.14. Despite these differences, the same effect of the area ratio with respect to the flow uniformity was obtained, see Figure 3.3.

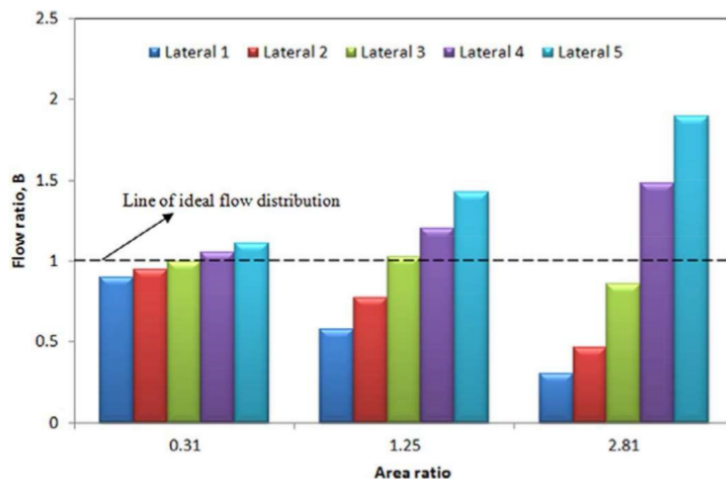


Figure 3.3: Flow uniformity for three different are ratios [5].

### 3.1.2. WIDTH RATIO

Similarly to the area ratio, Choit et al. [6] used numerical analysis to research the effect of the width ratio with respect to flow uniformity. The geometry as shown in Figure 3.4 was used for the analyses. The width of the dividing manifold was kept constant while the width of the combining manifold was varied to test width ratios of 0.5, 1, 2 and 4.

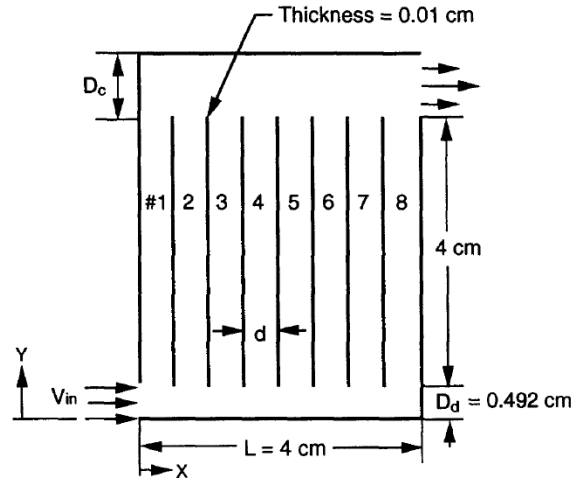


Figure 3.4: Geometry used by Choi et al. to analyse the effect of width ratio [6].

From the performed analyses it was found that the flow uniformity increases for an increasing width ratio, see Figure 3.5. This effect is dedicated to the decrease of the momentum gain in the combining manifold. Moreover, it is found that an increase in width ratio leads to a decrease in pressure drop over both the dividing and combining manifold, see Figure 3.6 [6].

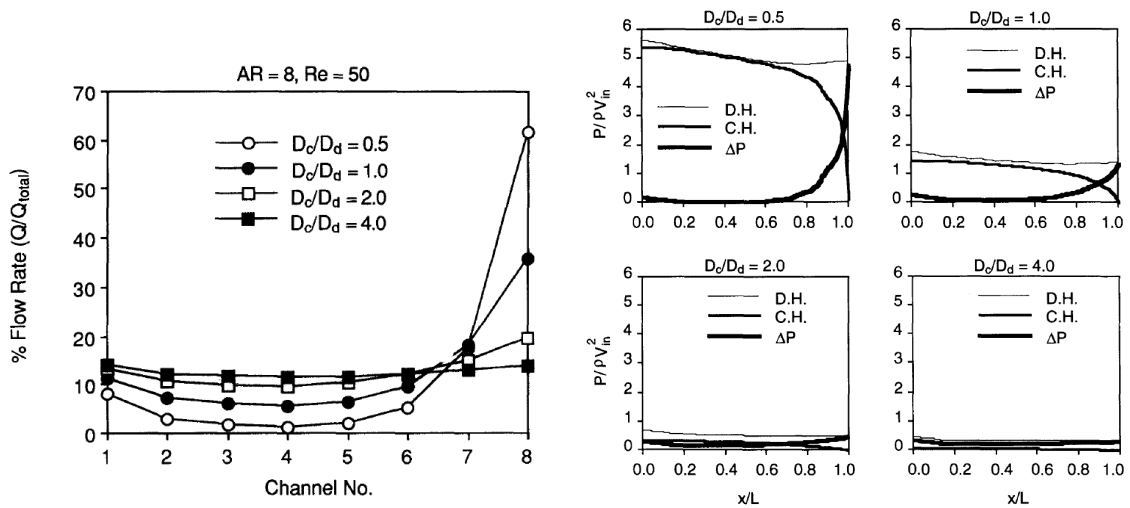


Figure 3.5: Flow rate through parallel channels for different width ratios [6]. Figure 3.6: Pressure coefficient for dividing and combining manifold for different width ratios [6].

Similar results are observed by Tonomura et al. [7] who performed a CFD-based optimisation for a parallel flow manifold system in micro-devices. From the results of Tonomura et al. [7], see Figure 3.7, it can be concluded that mainly the enlargement of the combining manifold has an effect on the flow uniformity. That is, for type B-2 in Figure 3.7, the combining manifold is twice as large as type B-1. Here the effect of the enlargement of the combining manifold can clearly be observed. Whereas, type B-3 has an enlargement of the dividing manifold with respect to type B-1. However, for these two types, only a small difference exists.

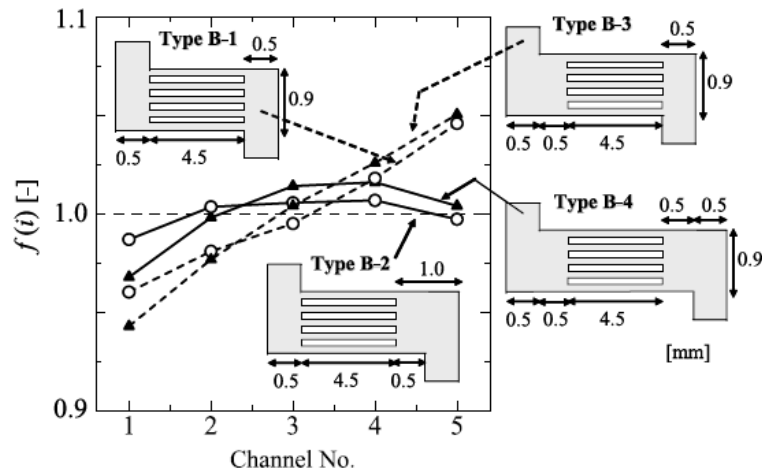


Figure 3.7: Normalized flow rate through parallel channels for different width ratios [7].

### 3.1.3. ASPECT RATIO

Although no literature was found with respect to the specific effect of the aspect ratio, Kim et al. [8] performed several analyses to determine the effect of several manifold geometries on the uniformity of the flow distribution. These analyses were performed using a 3D CFD model which was verified with an experiment. Taking a set of results where only the length and width of the manifold were varied, the trend as shown in Figure 3.8 was obtained. Where  $U$  is defined by Equation 3.4, hence the closer to unity  $U$  is the better the flow uniformity. From this trend, it can clearly be seen that for an increase in aspect ratio, the flow uniformity becomes better.

$$U = 1 - \text{standard deviation of normalized flow rate} \quad (3.4)$$

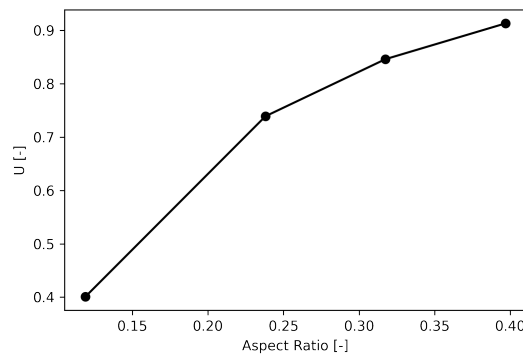


Figure 3.8: Effect of aspect ratio on flow uniformity based on the results of Kim et al. [8].

### 3.1.4. SHAPE

From the design method of London et al. [22], as discussed in section 2.1, it was already observed that for parallel flowing manifolds the dividing manifold should have an oblique shape to obtain uniform flow distribution. However, in this design method, it is assumed that the combining manifold has a constant cross-sectional area. Kim et al. [9] analysed three different shapes of dividing and combining manifolds, rectangular, trapezoidal and triangular, see Figure 3.9. From these analyses it was found that the triangular manifold shape resulted in the best flow uniformity, however, the pressure drop was also found to be highest for the triangular manifold [9].

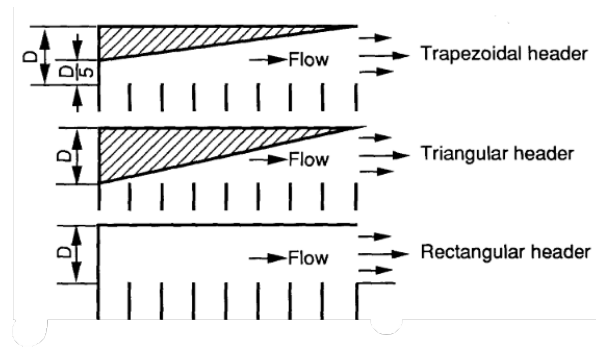


Figure 3.9: Three manifold shapes used to compare for performance [9].

Similar results were found by Dharaiya et al. [10], where two parallel flowing manifolds with the constant cross-sectional area were compared to two tapered manifolds with comparative hydraulic diameter, see Figure 3.10 and Figure 3.11.

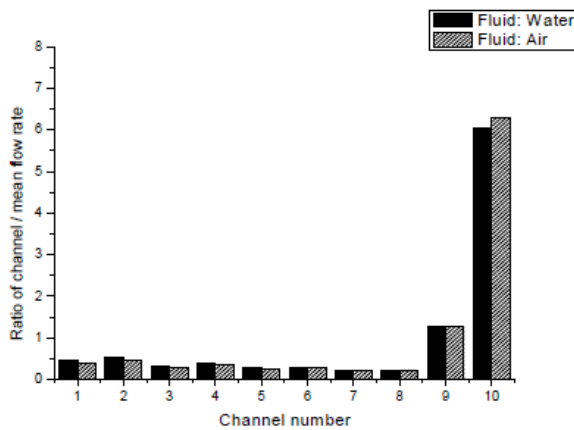


Figure 3.10: Flow distribution per channel for constant cross-section manifold with  $D_H = 0.7\text{ mm}$  [10].

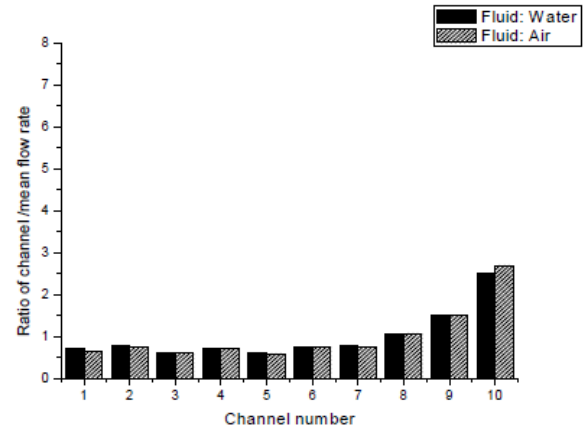


Figure 3.11: Flow distribution per channel for tapered manifold with  $D_H = 0.7\text{ mm}$  [10].

Moreover, Tong et al. [11], analyzed four different tapering methods and their effect on flow uniformity, i.e., linear, concave-down, concave-up and combined concave-down and concave-up see Figure 3.12. For applying the linear taper only to the dividing manifold it was found that applying a larger taper angle for all tested Reynolds numbers results in better flow uniformity. The same results were found for the concave-down taper, where a larger minor axis/major axis ratio results in better flow uniformity. However, the concave-up tapering was found to have a small negative effect on the flow uniformity. Furthermore, from the three non-linear tapering methods, the combined curve showed the most promising results, although only one configuration was tested. Moreover, it can be concluded that of the four tapering methods, the linear method was the most effective. Finally, it was found that tapering both the dividing and combining manifold cancels the positive effect of tapering only the dividing manifold [11].

The last finding is interesting as it opposes the earlier discussed findings of Dharaiya et al. [10]. After a careful examination of both papers, it is hard to say what caused the difference in the findings. Although the papers have slightly different definitions of flow uniformity it is not believed to be the cause of such a larger difference in results. Secondly, from the provided information it seems that both papers used a well-defined set-up for the CFD simulation, however, this is hard to judge as the details of the set-up are missing. Finally, the difference could come from the overall dimensions of the problem, however, the paper of Tong et al. [11] does not specify the used dimensions and therefore no comparison can be made. Therefore, it is concluded that care should be taken in the

interpretation of results in the research that will be performed.

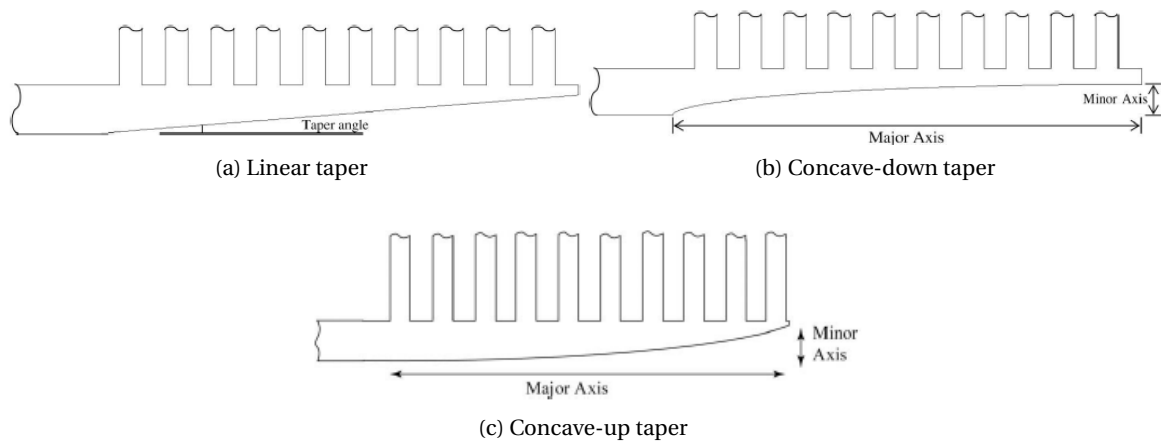


Figure 3.12: Tapering methods used by Tong et al. [11].

From the above analyses of geometrical effects on flow uniformity and pressure drop it can be concluded that the manifold in general should be as small as possible. However, in practice, the length of the manifold is often restricted by the required length of the HEX core. When the length is restricted it is best to enlarge the width of the manifold to get better flow uniformity. Generally, these modifications also result in a lower pressure drop over the manifold length. Moreover, it can be concluded that there exists a relation between the shape of the dividing and combining manifold. Finally, it can be concluded that tapering of the dividing manifold has a positive effect on flow uniformity, however, it will increase the pressure drop. Whether it is effective to change the shape of the combining manifold should be investigated as the literature does not agree on this effect.

### 3.1.5. REYNOLDS NUMBER

Two papers have been found investigating the relations between Reynolds number and mass flow maldistribution. However, different conclusions were obtained by the authors. The first study, performed by Choi et al. [6], explored the sensitivity by testing three different Reynolds numbers. Their findings, see Figure 3.13, show that there is an intricate relation between the Reynolds number and the obtained mass flow distribution. Choi et al. [6], state that the main cause of the drop in mass flow for the first channels and the increase in mass flow for the last channels is due to the increased inlet velocity. That is, due to the larger Reynolds number, the inlet velocity is larger, therefore the fluid is driven to the end of the manifold.

The second study, performed by Jiang et al. [5], also conducted experiments with three Reynolds numbers but arrived at a different conclusion. According to their findings, the change in flow uniformity was deemed insignificant despite the Reynolds number variations.

It is crucial to acknowledge that the observed variations in results may be attributed to the substantial differences in manifold design and the order of magnitude of the Reynolds numbers tested. Consequently, drawing a universal conclusion about the relationship between flow uniformity and Reynolds number becomes challenging.

In conclusion, the sensitivity of Reynolds number on mass flow maldistribution reveals a complex and case-dependent relationship. The manifold design, Reynolds number, and the specific use case significantly influence the observed outcomes. These findings underscore the importance of a nuanced approach when assessing the impact of Reynolds number variations on flow uniformity.

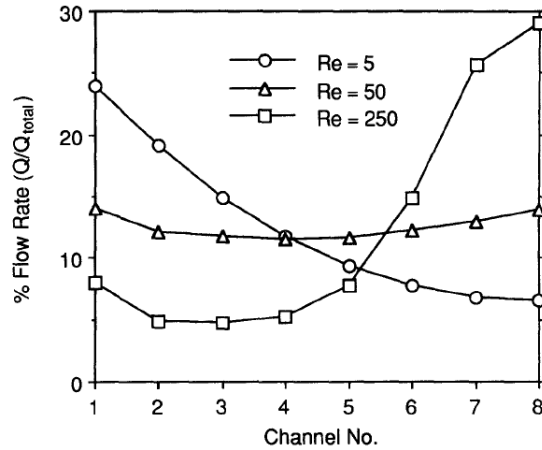


Figure 3.13: Mass flow distribution for three different Reynolds numbers in a manifold with an aspect ratio of 8 and a width ratio of 4 [6].

### 3.2. OPTIMISED MANIFOLDS

Although the design of manifolds and the several effects of geometrical and flow characteristics in these design problems have been studied extensively, only a few papers were found that made the step towards the optimisation of manifold systems. A set of these studies is the optimisation of the manifold structure, by adding baffle plates or guide vanes, however, these papers are not in the scope of this research and will not be discussed any further [25, 26].

In section 2.2 it is explained how Yang et al. [12] provide a solution to the analytical method of Bajura and Jones [2], simultaneously a parametric study was performed using this solution. From this study, it was found that the flow uniformity would be maximum when  $\gamma=1.44$ , see Figure 3.14. From this result, it can thus be concluded that for a manifold system with constant cross-sectional areas, a Pareto set of optimal designs exists [12].

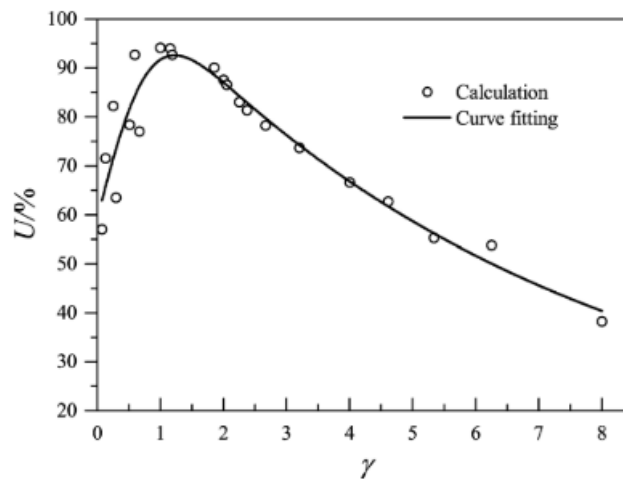


Figure 3.14: Results parametric study of Yang et al. [12].

Moreover, two papers were found using the discrete method, discussed in section 2.3, to optimise the dividing and combining manifold shape. Although a similar method was used, both papers result in different designs. In the paper of Pan et al. [3] the taper of the dividing manifold is distributed somewhat evenly over the entire length of the manifold, see Figure 3.15a where  $W_c$  is

the width of the channels,  $E$  is the depth of the channels, and  $N$  is the number of channels. Moreover, for the combining manifold the width increases slightly at the start of the manifold and then becomes almost constant after which it suddenly increases near the outlet, see Figure 3.15b. However, in the paper of Jackson et al. [13] the shape for both the dividing and combining manifold is similar to the shape found by Pan et al. [3] for the combining manifold, see Figure 3.16. However, the slow increase in width for the first few channels is not present in the results of Jackson et al. [13]. Moreover, it can be seen that the manifold width increases with the number of channels. At a certain point, this increase will result in unusable design features for which different solutions have to be found [13]. The difference between the obtained results can be explained by the different assumptions made when solving for the discrete solution. However, from both papers, it can be seen that when not constraining for a constant cross-sectional area a tapered shape is obtained.

The results of Yang et al. [12], Pan et al. [3] and Jackson et al. [13], all have in common that the designs of the manifolds have been optimized based on the existing design methods. The paper of Pan et al. [3] and Jackson et al. [13], did go a step further by verifying the optimized design using a CFD simulation. Although obtaining valuable insight using these methods, the optimized designs are still flawed due to the assumptions of the used design method.

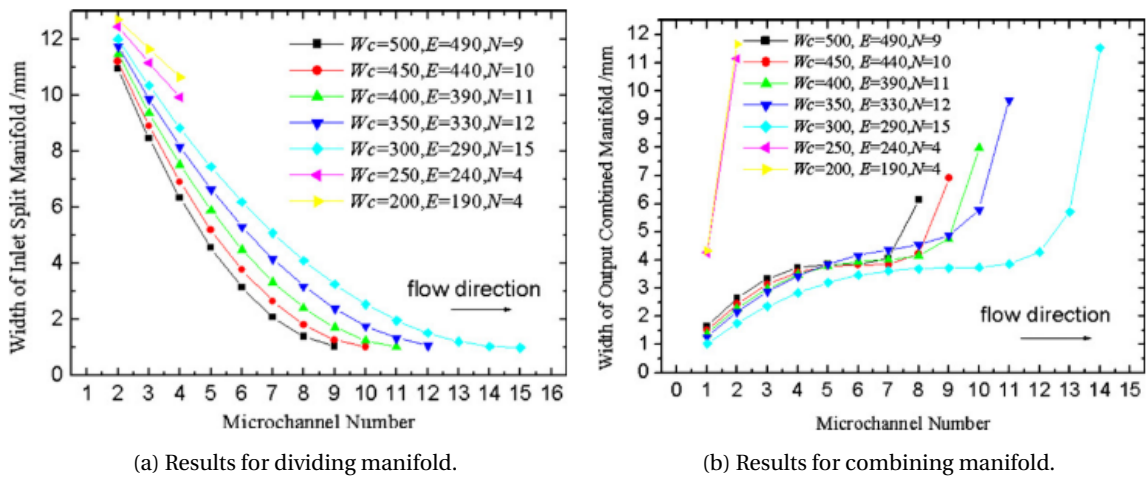


Figure 3.15: Optimal shapes for different channel widths and the number of channels [3].

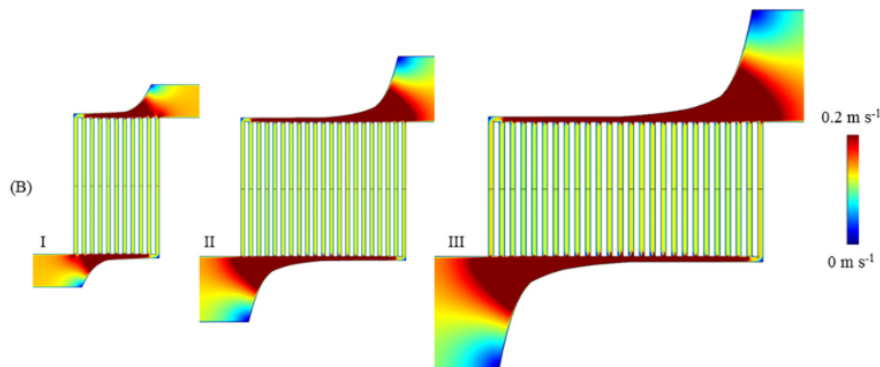


Figure 3.16: Optimised shapes from Jackson et al. [13].

More recently Kim [14] performed a 3D computational fluid dynamics (CFD) optimisation of a dividing manifold in a parallel flow configuration. For this optimisation procedure, the objective

function was divided into several sub-objective functions as in Equation 3.5, where the number of sub-objective functions was equal to the number of design variables. Then each design variable was updated based on the value of the sub-objective function as in Equation 3.6. Where  $n$  is the number of design variables,  $i$  is the current iteration,  $UR$  is the under-relaxation factor and  $Target$  is the target value for the sub-objective [14].

$$OBJ = f(obj_1, obj_2, \dots, obj_n) \quad (3.5)$$

$$v_{n,i+1} = v_{n,i} [1 \pm UR_n \{obj_n - Target_n\}] \quad (3.6)$$

The geometry of the manifold was parametrised by 22 coordinate points, one for each channel and one for the start and end of the manifold connected by non-uniform rational B-splines (NURBS) curves. The intermediate points, that is point 1 to 20, were placed on the axial position of the parallel channel centres along the upper wall of the manifold. The objective function of the optimisation procedure was flow uniformity through the parallel channels as in Equation 3.7. For this objective function, the sub-objectives were defined as the difference in mass flow through the first and  $n^{\text{th}}$  channel. However, this will result in 19 sub-objectives with 19 corresponding update functions, as in Equation 3.6. Hence, three more conditions have to be defined to update all design variables. The first condition was to fix the position of the first design point as in Equation 3.8, i.e., the inlet of the manifold will keep the original width. The second condition was to define the position of the second design point as the average of the first and third design point as in Equation 3.9. The third condition was to set the height of the end wall equal to the height of the 21<sup>st</sup> design point as in Equation 3.10. Furthermore, the convergence criteria were set to  $1e-4$  for the difference between the  $i^{\text{th}}$  and the  $i+1^{\text{th}}$  objective evaluation and a decrease of the new objective. The full optimisation procedure can be seen in Figure 3.17 [14].

$$OBJ = \sqrt{\left( \sum_{i=1}^N \left( \frac{\dot{m}_i - \dot{m}_{i,ideal}}{\dot{m}_{i,ideal}} \right)^2 \right) / (N-1)} \quad (3.7)$$

$$y_{0,i+1} = y_{0,i} \quad (3.8)$$

$$y_{1,i+1} = 0.5(y_0 + y_{2,i+1}) \quad (3.9)$$

$$y_{21,i+1} = y_{20,i+1} \quad (3.10)$$

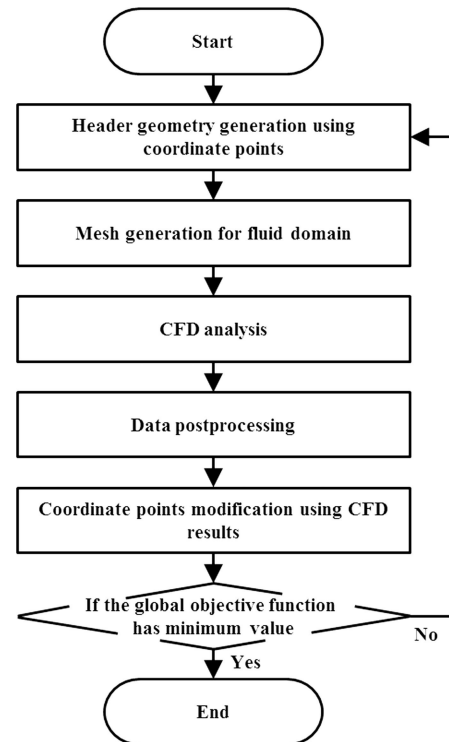


Figure 3.17: Optimisation procedure used by Kim [14].

The results of the above-described optimisation procedure can be found in Figure 3.18. In Figure 3.18a it can be seen that the optimisation procedure took nine iterations, where the objective function went from 0.3808 to 0.0148. This increase in flow uniformity however results in an increase

in the total pressure drop, as can be seen in [Figure 3.18b](#). However, from [Figure 3.18c](#) it can be concluded that the increase in pressure drop is mainly due to the parallel channels. Though, the pressure drop in the dividing manifold also slightly increases for the optimised manifold. Moreover, from [Figure 3.18d](#) it can be seen that the final shape is different from the theoretically predicted shape. Where the theoretically predicted shape is based on the design method of London as discussed in [section 2.1](#).

However, Kim [14] used a limited number of variables in the optimization, limiting the design space of the optimizer. Moreover, no verification regarding the optimality of the solution was provided. Combined with the use of a zeroth-order optimization algorithm, no conclusions can be given on the optimality of the design.

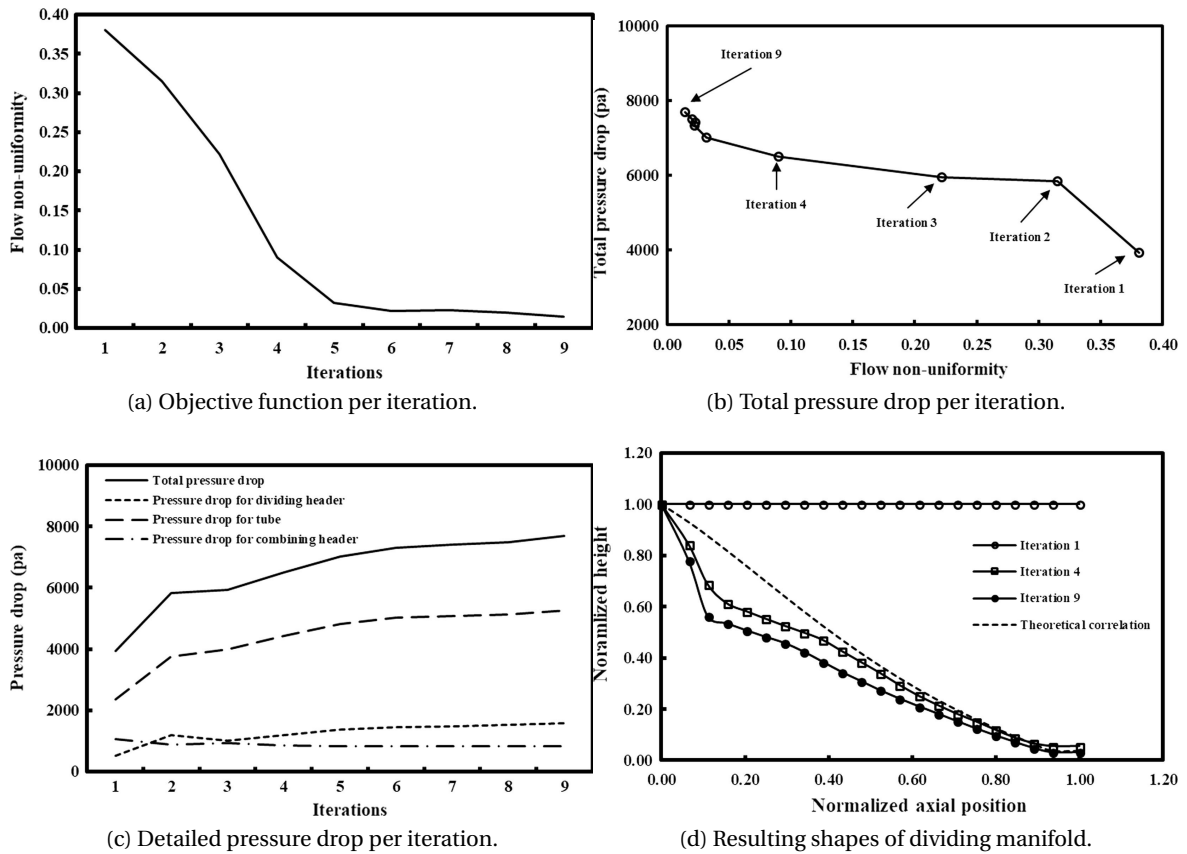


Figure 3.18: Results obtained from optimisation procedure performed by Kim [14].

# 4

## CONCLUSION

From the first section of this chapter, it becomes clear that several types of manifolds exist. Moreover, it is shown how these types of manifolds can be configured in several different systems. It also becomes clear that the most challenging design, w.r.t. equal mass flow distribution, is a consecutive parallel flowing manifold system. Hence, it is of interest to take a closer look into the optimization of that specific system.

The second chapter discussed several different design methods for manifolds, to reduce the mass flow maldistribution. From the paper of London et al. [22] simple shape functions are obtained for the dividing manifold. However, these shape functions are derived using a set of simplifying assumptions. Bajura and Jones [2] critiqued this methodology and provided an analytical solution to the flow distribution in dividing manifold systems. Furthermore, Yang et al. [12] used this analytical solution to create a design guide for dividing manifold systems. However, this design guide, although rather simple, only holds for a dividing manifold of constant area. Finally, the discrete design method by Pan et al. [3] was discussed. The design method simplifies the flow in the manifold system significantly, i.e., the actual flow is unlikely to be entirely laminar, and the flow resistance is more intricate than initially depicted. Nevertheless, the underlying concept of the method is robust, and with refinement, it has the potential to yield an accurate design guideline.

The third section discusses the current literature that either performed a sensitivity analysis with respect to manifold design or performed an optimization procedure on a manifold. From the sensitivity analyses, it can be concluded that: smaller area ratios are beneficial for the mass flow distribution; larger width ratios are beneficial for mass flow distribution; larger aspect ratios are beneficial for mass flow distribution and oblique shapes are beneficial for mass flow distribution. Moreover, it was concluded that a more intricate relation exists between the Reynolds number and the mass flow maldistribution. Finally, it was shown how several papers used different methods for the optimization of manifold systems. Most of these papers used an existing design method to optimize the design of the manifold system. It was concluded that the obtained optimized design are inherently flawed due to the assumptions present in the design methods. Moreover, the optimization procedure of Kim [14] was discussed. In this paper, a dividing manifold was optimized using 3D CFD simulations. However, due to the optimization algorithm, number of design variables and lack of optimality verification it was concluded that the obtained results are indicative at best. However, it was shown that a better design than the obtained design from either London's or Yang's design method is attainable. Therefore, it is of interest to use modern methods such as adjoint-based gradient search and free form deformation to optimize a consecutive dividing parallel flowing manifold.

# II

## RESEARCH PAPER

# 3D Shape Optimization of Consecutive Manifolds using Free Form Deformation and Adjoint-Based Methods.

L. van der Mark\*

*Delft University of Technology, Delft, 2628 CD, The Netherlands*

Current design methods for oblique manifolds were first presented in the paper of London et al. in 1968. This method presents a single equation to shape the dividing manifold of several manifold configurations. However, current literature shows a potential to improve the current design method by implementing advanced techniques. This paper aims to bridge this gap by presenting an innovative design methodology incorporating these advanced techniques. The proposed design method integrates free-form deformation and adjoint-based methods within a 1st-order shape optimization framework. The objective function focuses on the minimization of mass flow mal-distribution, evaluated by an incompressible Reynolds-Averaged Navier-Stokes solver. Through three initial tests, this paper demonstrates a consistent improvement in the objective for all obtained designs. Noteworthy is the finding that small changes to the initial design lead to significant enhancements, evidenced by an 82.5% decrease in the mass flow mal-distribution. Off-design testing further substantiates the effectiveness of the design method, showcasing superior performance under varying initial conditions for the optimized designs. Further testing not only exhibits improved objectives but also reveals common features among results for diverse initial designs. This paper shows a novel and effective design methodology for consecutive manifold systems, laying a robust foundation for an improved design method.

## I. Introduction

THE design method for oblique manifolds has not changed in the past 56 years, since its first introduction by London et al. [1]. Manifolds are responsible for the distribution and collection of fluid over multiple channels and are used in several applications, such as heat exchangers, engines, fuel cells and irrigation systems. Two main types of manifolds exist: bifurcating and consecutive manifolds. Bifurcating manifolds are designed such that the flow is split into two equal streams until all the desired outlet ports are reached [2]. Consecutive manifolds divide the flow into the required amount of sub-streams in one single step, often connecting multiple ports or channels placed on one lateral side of the manifold [2]. In industrial applications, consecutive manifolds are often used due to their relatively compact size and simple design. Furthermore, it is possible to realize different flow arrangements based on the relative flow orientation of a dividing and combining manifold pair. If the flow in the dividing and combining manifolds has always the same flow directions with respect to that of the lateral channels, then the resulting flow arrangement is called parallel. Controversy, if the flow has an opposite direction in the two manifolds, then the overall flow arrangement is of the reverse type. Finally, if the main stream enters and exits at the middle of the manifold, then the configuration is defined as centred. Xia et al. [3] showed that the parallel configuration results in the worst mass flow distribution across lateral channels. Therefore, this paper will focus on the design of parallel consecutive manifold design.

The design method of London et al. [1] provides a way to define the shape of consecutive dividing oblique manifolds. Notably, the shape is determined through the application of Bernoulli's equation, assuming a uniform one-dimensional inviscid flow within the manifolds. Moreover, two main design conditions are imposed; the combining manifold has a constant area along the length of the manifold; the fluid mass flow is equally distributed across the parallel channels connected by the manifolds. The second condition results in the prerequisite that the pressure distribution in the dividing and combining manifold should be parallel to each other. This prerequisite is utilized to derive an equation for the required shape necessary to achieve this parallel pressure distribution. This is accomplished by equating the obtained pressure profile in both manifolds to each other and rearranging the equation using continuity equations [1].

Although London et al [1] provide a simple procedure to determine the shape of the dividing manifold, the method relies on several assumptions and neglects important effects, such as momentum loss. Bajura and Jones [4] argue that the choice of a relevant streamline in the Bernoulli equation becomes difficult when considering the conservation of momentum. They provide a generalized control volume analysis of the fluid flow in manifolds. Shen [5] used the

---

\*MSc. Candidate, Faculty of Aerospace Engineering Department of Power and Propulsion, Kluyverweg 1, Delft, the Netherlands.

equation of Bajura and Jones to provide an analytical solution to determine the effects of friction on the fluid mass flow distribution. This analytical solution showed a slightly better fit, however, it is not suitable for design calculations [5][6]. Yang et al. [6] identified this issue and provided an analytical solution suitable for design calculations. Yang et al. [6] used this analytical solution to analyze several manifold designs. This analysis resulted in a parametric equation relating the manifold dimensions and flow conditions to the fluid mass flow distribution.

There is limited literature on the optimization of dividing manifolds, yet plenty of research has been performed regarding the investigation of the effect on the performance of the main geometrical characteristics of manifolds. It has been shown that a small area ratio, that is the ratio between the total cross-sectional area of the channels in parallel over the cross-section of the manifold, is beneficial to obtain a homogeneous mass flow distribution in the parallel channels[7][8]. Similarly, Choi et al. [9] and Tonomura et al. [10] show that a large width ratio, that is the ratio between the width of a combining and dividing manifold, is beneficial to achieve a uniform mass flow distribution. Furthermore, Kim et al. [11] shows that for a large aspect ratio, that is the ratio between the width and length of the manifold, the uniformity of mass flow distribution improves. Finally, it is proven that tapered shapes, such as the shape provided by London et al. [1], are beneficial to minimize differences among the mass flow rate of the various channels in parallel [12][13][14].

Recently, Kim [15] performed a 3D CFD optimization of a dividing manifold. The initial design consisted of a manifold with a constant cross-section along the length. The manifold was parameterized via non-uniform rational B-splines (NURBS) for a total of 22 control points. The objective of the optimization was to minimize the so-called mass flow mal-distribution factor, which is the variance of mass flow in the parallel channels. The optimization procedure resulted in an improved performance for the dividing manifold, compared to London et al.'s procedure.

Although London et al.'s design method has been used for several years. Bajura and Jones already stated that the simplifying nature of the Bernoulli method ignores important effects [4]. They provided a generalized flow model to capture most of the important flow phenomena. Yang et al. used this model to provide a set of parametric equations, such that an optimal dividing manifold could be designed for any flow [6]. However, a big limitation of this method is the assumption that the manifold has a constant cross-section, hereby severely limiting the design space. Furthermore, Kim showed that using CFD and optimization procedures will result in a better design than London's method [12]. However, the parametrization method limits the design space, resulting in a 2D shape optimization. Finally, no literature was found implementing advanced techniques such as free-form deformation and adjoint gradient search in the design procedure of manifolds.

Current literature has shown that better shapes for dividing manifolds can be obtained when using CFD-based optimization. However, currently available advanced methods have not been applied in this context before. The objective of this research is to provide a novel design method for dividing manifolds by devising a CFD-based optimization method leveraging advanced techniques such as the free-form deformation and adjoint method.

An important choice in shape optimisation is how the surfaces to be optimized are parameterised. However, several parameterisation methods exist, i.e., basis vector, domain element, PDE, discrete, polynomials and splines, analytical, free-form deformation (FFD) and computer-aided design (CAD) [16]. The first six methods are limited in their use as they either do not allow for complex geometries or only allow for small geometry changes. Furthermore, FFD and CAD-based methods are often used due to their efficiency, compactness and ease of use with complex geometries [16][17]. However, the FFD method, due to its flexibility, does not allow for the direct control of design features. At the same time, CAD-based methods allow for direct control of design features but at the cost of reduced design flexibility [17][18]. Due to the allowed flexibility in shape deformation and its availability in the SU2 software suite, the FFD method has been preferred in this work to implement a shape optimization method for oblique manifolds.

Furthermore, the choice of the optimization algorithm is important. The main trade-off is between the use of 0<sup>th</sup>, 1<sup>st</sup> and 2<sup>nd</sup>-order methods. The 0<sup>th</sup>-order methods are often the simplest algorithms as they only make use of direct function evaluation. This simplicity, however, is at the cost of longer convergence times of the optimizer. The 1<sup>st</sup> and 2<sup>nd</sup>-order methods are more complex as they make use of the first and second derivative, respectively, of the objective function [19]. To promote the search for the optimum. In this research a 1<sup>st</sup>-order optimization algorithm is used.

To calculate the gradient of the objective function several methods could be used, such as the forward or central difference method, the complex step method, the adjoint method etc. [20]. However, methods such as forward difference, central difference and complex step require a function evaluation for each perturbation of a design variable. This quickly results in a prohibitive computational cost for CFD-based optimization procedures with multiple design variables, as every function evaluation may require several hours of simulation. The adjoint method requires only one extra function evaluation for every objective and constraint in the optimization problem [21]. Hence, it provides a much more efficient strategy to handle multiple design variables in CFD-based optimization problems.

## II. Methodology

The design chain of the optimization procedure is described using the extended design structure matrix (XDSM) presented in Figure 1. The main process steps of the optimization procedure are placed along the diagonal of the diagram. The output of each procedure block is placed along the same row of the corresponding block, while the inputs are placed above the considered block. Moreover, the number and thin black lines represent the order of operations, whereas the thick grey line represents the data stream [22].

The first step in the procedure is the parameterization of the mesh, which requires the baseline design of the manifold ( $\mathbf{G}$ ) as an input. The second step is the parameterization of the FFD box, where the surface ( $\mathbf{X}_{surf}^0$ ) to be optimized is linked to the nodes in the FFD box. The third step is the optimization, here the objective ( $\mathcal{J}$ ) and the objective gradient ( $d\mathcal{J}/d\alpha$ ) are used to determine the new design vector ( $\alpha$ ). To initialize the computation, as the results of the flow solver and adjoint solver are not known in the first design step, the optimizer is provided with an initial design vector ( $\alpha^0$ ) of zeroes. The fourth step is mesh deformation, which takes the new design vector to create the corresponding new, and thus deformed, mesh ( $\mathbf{X}_{vol}$ ). The fifth step is the simulation of the CFD model, in this work an incompressible Reynolds averaged Navier-Stokes (RANS) solver is used to find the state variables ( $\mathbf{U}$ ), residuals ( $\mathbf{R}$ ) and the value of the objective function associated with the new geometry. The sixth step provides the solution of the adjoint problem, which uses the solutions of the flow solver and the mesh deformation to determine the gradient of the objective function with respect to the design variables.

To practically implement the presented XDSM several software programs are used. The 3D model of the manifold, i.e. the initial design  $\mathbf{G}$  in Figure 1, is created using ANSYS SpaceClaim<sup>1</sup>. The mesh parametrization, step 0 in Figure 1, is done in ANSYS ICEM CFD<sup>2</sup>. For the mesh deformation, as well as the flow and adjoint solver, that is step 3-5 in Figure 1, the SU2<sup>3</sup> suite was used. Finally, for the optimizer, it was chosen to use the Interior Point Optimizer (IPOPT<sup>4</sup>). To implement the communication between the optimizer and the different SU2 executables, the Framework for Aeronautical Design Optimization (FADO<sup>5</sup>) has been adopted.

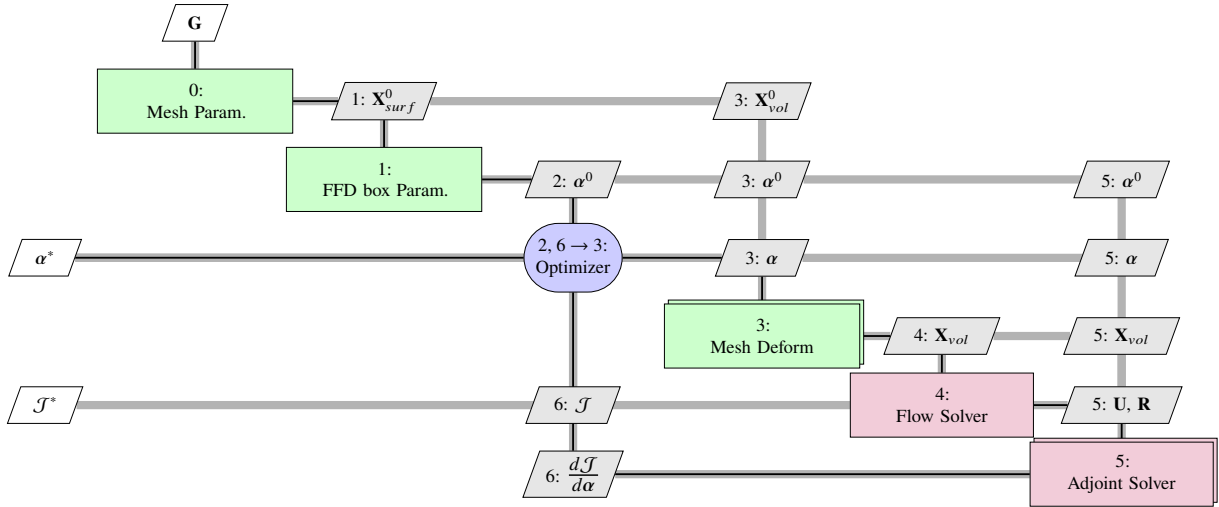


Fig. 1 The extended design structure matrix of the optimization procedure.

<sup>1</sup><https://www.ansys.com/products/3d-design/ansys-spaceclaim>

<sup>2</sup><https://www.ansys.com/training-center/course-catalog/fluids/introduction-to-ansys-icem-cfd>

<sup>3</sup><https://su2code.github.io/>

<sup>4</sup><https://coin-or.github.io/Ipopt/>

<sup>5</sup><https://github.com/su2code/FADO>

## A. Test Case and Definition of the Baseline Manifold Design

To demonstrate the capability of the methodology, a manifold of an exemplary radiator with 10 lateral channels was selected. These lateral channels were characterized by a diameter of 3 mm and a length of 55 mm. The pitch between the channels, center to center, was set at 1.5 times the channel diameter. Moreover, the center of the first channel was placed 18 mm from the inlet. Finally, the length of the outlet manifold was exaggeratedly extended to ease the converge of the RANS solver, as non-flow uniformity at the outlet port generates significant variations in the back pressure of the parallel channels, causing fluctuations in the estimated mass flow rate in each channel. To determine a proper diameter for the manifolds, the analytical design method described by Yang et al. [6] was used. Yang et al. [6] state that a dividing manifold ensures an optimal mass flow distribution if the coefficient  $\gamma$  defined by Equation (1) has a value around 1.44.

$$\gamma = \frac{\alpha^2}{\beta^3} \quad (1) \quad \alpha = \left(\frac{\lambda^2 L}{D}\right)^{1/2} \cdot \left(\frac{f}{H}\right)^{1/2} \quad (2) \quad \beta = \lambda \cdot \left(\frac{2 - \gamma_d}{H}\right)^{1/2} \quad (3)$$

Here  $\lambda$  is the ratio between the total cross-sectional area of the lateral channels in parallel and the manifold cross-sectional area (area-ratio),  $L$  is the length of the manifold,  $D$  the diameter of the manifold,  $f$  the friction coefficient of the flow in the manifold,  $H$  the flow resistance in the lateral channels,  $\gamma_d$  the static pressure recovery coefficient, which is a factor that takes into account the uncertainty in the axial momentum loss due to the turning of the fluid [6][23]. Water was chosen as a working fluid, with a temperature of 300.45 K, inlet velocity of 1.0 m/s, inlet density of 995.64 kg/m<sup>3</sup> and a viscosity of 8e<sup>-4</sup> kg/m s. Moreover, the fluid was assumed to be incompressible.

The friction coefficient in the manifold was estimated using Equation (4), while the flow resistance in the lateral channels was calculated using Equation (5) as defined by Bajura and Jones[4]. Here  $\Delta P_c$  is the overall pressure drop over the length of the lateral channel, from experiments estimated to be 40 kPa. Moreover,  $\rho$  is the fluid density in the channel and  $\bar{V}_c$  is the average velocity in the channel, which was estimated assuming perfect mass flow distribution. Finally,  $\gamma_d$  was estimated to be 0.94 from Figure 2 in the paper of Bajura [23].

$$f = \begin{cases} \frac{64}{Re} & Re < 2200 \\ \frac{0.3164}{Re^{0.25}} & Re < 1e5 \\ 0.0032 + \frac{0.221}{Re^{0.237}} & \text{otherwise} \end{cases} \quad (4) \quad H = \frac{2\Delta P_c}{\rho \bar{V}_c^2} \quad (5)$$

Using the above equations, a diameter of 10.5 mm was found to be optimum for the chosen test case. The method provided by Yang et al. [6] is only applicable to dividing manifolds. For simplicity, the same diameter was used for the combining manifold.

Next, Equation (6) and Equation (7) provided by London et al. [1] were used to shape the dividing manifold.  $Z$  represents the normalized height of the manifold ( $z_{wall}/y_o$ );  $X$  is the normalized location along the manifold length ( $x/L$ );  $\rho_i$  and  $\rho_o$  are the inlet and outlet density;  $z_i$  and  $y_o$  are the initial heights of the dividing and combining manifold, respectively, and  $h_i$  and  $h_o$  is the velocity head in the dividing and combining manifold. Combining Equation (6) and Equation (7) together with the assumption of an incompressible flow, leads to Equation (8).

$$Z = \frac{(1 - X)}{\left[\left(\frac{\rho_i}{\rho_o}\right) \left(\frac{\pi^2}{4}\right) X^2 + \left(\frac{y_o}{z_i}\right)^2\right]} \quad (6) \quad \frac{h_o}{h_i} = \frac{\rho_i}{\rho_o} \left(\frac{z_i}{y_o}\right)^2 \quad (7) \quad Z = \frac{(1 - X)}{\left[\left(\frac{\pi^2}{4}\right) X^2 + 1\right]} \quad (8)$$

It follows from Equation (8) that the normalized height of the manifold depends only on the height at the inlet of the manifold itself, as well as its length. Moreover, it can be noted that the method of London et al. [1] provides only information about two dimensions of the manifold. The profile of  $Z$  is assumed to be independent of the width or depth of the manifold. Hence, to obtain a 3D shape,  $Z$  was interpreted as the local diameter of the manifold. Finally, according to Equation (8) the manifold height/diameter becomes equal to 0 mm at the end of the manifold. This would make it impossible to properly connect the manifold and the last lateral channel(s). Therefore, the effective height used to calculate the shape was taken to be 3 mm smaller than the actual height, thereby assuming a minimum diameter of 3 mm. This resulted in the 3D model as presented in Figure 2. The main dimensions of the manifold can be found in Table 1 while the coordinates of the manifold profile can be found in Appendix A.

**Table 1** Dimensions of the initial 3D model used in the optimization procedure.

Dimension	Size
manifold diameter [mm]	10.5
length dividing manifold [mm]	61.5
length combining manifold [mm]	119
diameter lateral channel [mm]	3
length lateral channel [mm]	55
spacing between channel centres [mm]	4.5
distance inlet to first channel centre [mm]	18
number of channels [-]	10
fillet radius [mm]	0.25

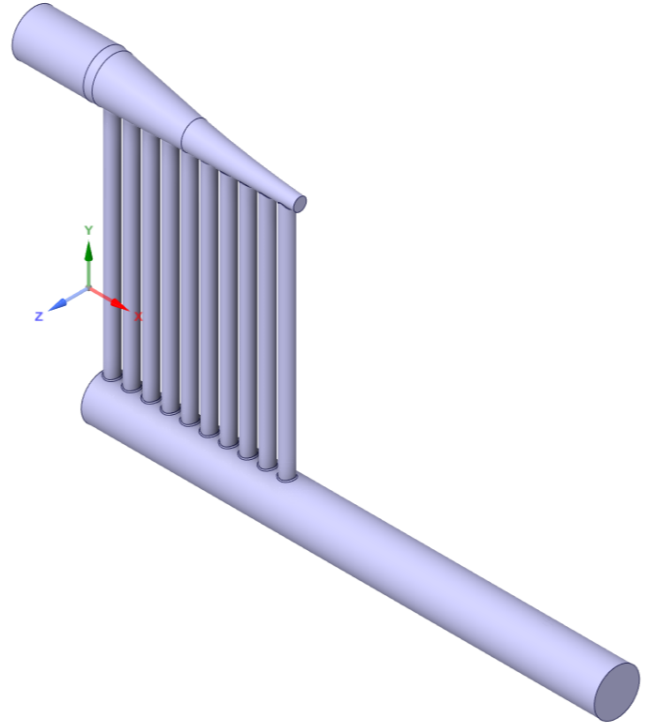


**Fig. 2** Initial 3D model used in the optimization procedure.

In the initial tests, it was found that a sharp corner between the manifold and channel inlets caused numerical instabilities. These sharp corners resulted in non-physical flow patterns as shown in Figure 3. To resolve this issue, fillets were placed between the manifolds and channel inlets. These fillets were given a radius of 0.25 mm, to not affect the flow in the manifold too much while maintaining a size that the mesh could capture.

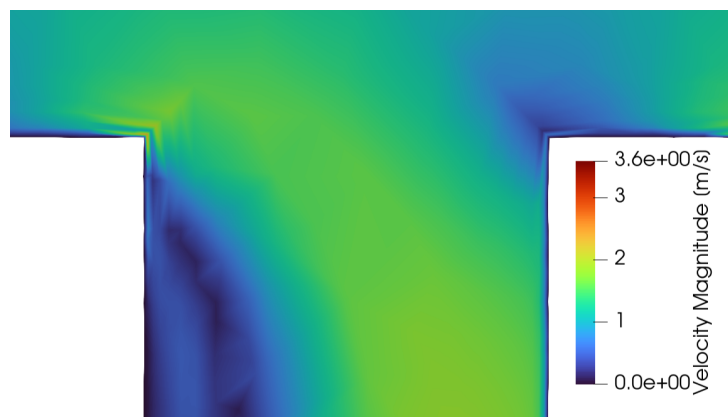


**Fig. 3** Resolved flow in a manifold with sharp corners, a non-physical flow pattern can be seen in the left corner, at the manifold-channel interface.

## B. Mesh

The geometry was meshed with tetra-mixed volume elements using the Octree method in ANSYS ICEM CFD [24]. To create a proper mesh the 3D model was divided into different parts, namely: the inlet surface, where a uniform velocity profile is imposed; the dividing manifold surface; the fillet surfaces between the dividing manifold and lateral channels; the lateral channel surfaces; the fillet surfaces between the lateral channels and the combining manifold; the combining manifold surface; and the outlet surface where the systems back-pressure is imposed. Moreover, for each channel, a surface was added 5 mm before the outlet of the channel itself, to determine the local mass flow rate. This information is needed, such that the objective function can be evaluated by the solver. It was found that the location of these surfaces has a negligible effect on the value of the objective function.

Due to the algorithm of the Octree method, in which each mesh element is successively divided by two until the required mesh size is achieved, neighbouring elements in the mesh are, at most, a factor of two apart [24]. This was taken into account when defining the mesh sizes. To determine a suitable mesh size for the different parts of the geometry a mesh convergence study was performed, details can be found in section III. The selected surface mesh sizes can be found in Table 2, the maximum size of a volume mesh element was found to be 2 mm.

Moreover, it was found that a mesh refinement was required at the inlet of the channels and the first half of the combining manifold, as reported in Table 3. The channel refinements begin at the center where the dividing manifold meets the channel and extend 10 mm downward in the center of the channel. The combining manifold refinement starts in the centre of the combining manifold at  $x=16$  mm and extends 45 mm into the manifold.

**Table 2 Maximum surface mesh size settings for the different parts of the 3D model.**

Part	Mesh Size [mm]
Inlet	0.25
Dividing Manifold Surface	0.5
Dividing Manifold-Channel Fillet	0.125
Channel Surfaces	0.25
Combining Manifold-Channel Fillet	0.125
Combining Manifold Surface	0.5
Outlet	0.25

**Table 3 Used settings for the local mesh refinements.**

Channel Inlets	
Mesh size [mm]	0.25
Growth ratio [-]	1.2
Number of layers [-]	7
Combining Manifold	
Mesh size [mm]	1.0
Growth ratio [-]	1.2
Number of layers [-]	4

Finally, to properly predict the velocity profile in the proximity of the walls, a prism layer was added on all the walls of the domain. To determine the height of the first cell in the prism layer ( $y_1$ ) Equation (9) was used, with  $y^+ \leq 10$ . This resulted in a height of  $4.7e^{-5}$  m for the region of the parallel channels. However, here a perfect mass flow distribution was assumed. Conservatively, the initial height was chosen to be  $3e^{-5}$  m for the entire domain. Furthermore, the prism layer was set up with an exponential growth factor of 1.3, for a total of 7 layers.

$$y^+ = \frac{u_t y_1 \rho}{\mu} \quad (9) \quad u_t = \sqrt{\frac{\tau_w}{\rho}} \quad (10) \quad \tau_w = \frac{1}{2} f \rho V_\infty^2 \quad (11)$$

## C. FFD box parameterization

To implement the FFD box parameterization, the SU2\_DEF executable was used, see the SU2 website<sup>6</sup> for more details. Two different FFD boxes have been defined, one around the dividing manifold and one around the combining manifold.

For the dividing manifold the FFD box starts at 5 mm from the inlet and ends at 0.5 mm after the end of the manifold. Along both the y- and z-direction the corner points of the FFD box are defined at 5.25 mm from the center in both directions. Where the center of the FFD box coincided with the center point of the inlet surface of the manifold. Furthermore, the FFD box has been defined into 14 sections in both the y and z-direction and 29 sections in the x-direction. Finally, the surface of the dividing manifold, as defined in the mesh parametrization, has been set as the surface to be deformed.

For the combining manifold the FFD box starts at 1 mm in front of the combining manifold, and the FFD box ends at 35.5 mm before the outlet. The coordinates along the y-and z-direction have been defined at 5.25 mm from the center

<sup>6</sup>[https://su2code.github.io/tutorials/Species\\_Transport/](https://su2code.github.io/tutorials/Species_Transport/)

in both directions. Where the center of the FFD box coincides with the center of the outlet surface of the manifold. The FFD box has also been divided into 14 sections in the y and z-direction. The FFD box was divided into 44 sections in the x-direction such that the distance between the FFD nodes is similar to the FFD box around the dividing manifold.

#### D. Mesh Deformation

The mesh deformation is performed by the SU2\_DEF executable via a two-step process. The first step consists of deforming the surface controlled by the FFD box. The second step consists of deforming the volume mesh, based on the deformed surface.

It is worth recalling the basics of the FFD algorithm. First, let us define a local coordinate system  $(S, T, U)$ . Now, for any point  $X$ , a set of coordinates  $(s, t, u)$  can be defined such that Equation (12) holds. This set of coordinates can be found using Equation (13).

$$X = X_0 + sS + tT + uU \quad (12)$$

$$s = \frac{T \times U(X - X_0)}{T \times US}, \quad t = \frac{S \times U(X - X_0)}{S \times UT}, \quad u = \frac{S \times T(X - X_0)}{S \times TU} \quad (13)$$

The next step is to define a grid of control points,  $P_{ijk}$ , defined in the local coordinate system. Where the indexes  $i, j$  and  $k$  indicate the  $l + 1$  nodes in the  $S$ -direction,  $m + 1$  in the  $T$ -direction and  $n + 1$  in the  $U$ -direction, respectively. The location of the control points can be defined as in Equation (14), where the indexes  $i, j$  and  $k$  range from zero to  $l, m$  and  $n$  respectively. Note that the mathematical procedure represents the parameterization of the FFD box indicated as step one in the XDSM and that the resulting vector of control points  $P_{ijk}$  corresponds to the design vector  $\alpha$ .

$$P_{ijk} = X_0 + \frac{i}{l}S + \frac{j}{m}T + \frac{k}{n}U \quad (14)$$

Now the surface deformation is specified by moving the control points from the initial position in any given direction. Then the deformation of an arbitrary point  $X$  on the surface is calculated using the trivariate Bernstein polynomial in Equation (15), where  $X_{ffd}$  is the deformed position of point  $X$ . For more information on FFD boxes, the reader is referred to the paper of Sederberg and Parry [25].

$$X_{ffd} = \sum_{i=0}^l \binom{l}{i} (1-s)^{l-i} s^i \left[ \sum_{j=0}^m \binom{m}{j} (1-t)^{m-j} t^j \left[ \sum_{k=0}^n \binom{n}{k} (1-u)^{n-k} u^k P_{i,j,k} \right] \right] \quad (15)$$

To deform the volume mesh a linear elasticity-based approach is used [26][27]. Based on preliminary tests, it was found that setting the stiffness model to wall distance in SU2 resulted in the best quality of the deformed mesh.

#### E. Flow Solver

The flow field within the domain is simulated utilizing the SU2\_CFD executable, which is the Computational Fluid Dynamics (CFD) code of the SU2 suite. Regarding the CFD model, the incompressible Reynolds Averaged Navier Stokes (RANS) method [28] is used with the Menter Shear Stress Transport (SST) turbulence model of 2003 [29][30]. At the inlet of the flow domain, a velocity of 1.0 m/s in the x-direction and a temperature of 300.45 K was imposed. At the outlet, a back pressure of 0.0 Pa was imposed. At the walls of the dividing manifold, channels and combining manifold a no-slip condition was imposed. Finally, the surfaces created in the channels were set as internal surfaces such that they would not interfere with the flow solution. For specific settings used in the configuration file, the reader is referred to Appendix F. For more details on how the incompressible RANS method or the SST turbulence model is implemented in the SU2 suite the reader is referred to the papers of Economou [28] and Menter [29][30].

#### F. Adjoint Solver

To solve for the gradient of the objective function, SU2 uses Equation (16). Where  $d\mathcal{J}/d\alpha$  is the total gradient of the objective ( $\mathcal{J}$ ) with respect to the design vector ( $\alpha$ ),  $M(\alpha)$  is the system of equation expressing the mesh deformation and  $d\mathcal{J}/d\mathbf{X}$  is the sensitivity of the objective function to the volume mesh deformation [31][32]. Substituting Equation (17) into Equation (16), gives Equation (18).

$$\frac{d\mathcal{J}}{d\alpha} = \frac{d}{d\alpha} M^T(\alpha) \frac{d\mathcal{J}}{d\mathbf{X}} \quad (16) \quad \frac{dM}{d\alpha} = \frac{d\mathbf{X}}{d\mathbf{X}_{surf}} \frac{d\mathbf{X}_{surf}}{d\alpha} \quad (17) \quad \frac{d\mathcal{J}}{d\alpha} = \frac{d\mathcal{J}}{d\mathbf{X}} \frac{d\mathbf{X}}{d\mathbf{X}_{surf}} \frac{d\mathbf{X}_{surf}}{d\alpha} \quad (18)$$

To evaluate the first derivative on the right-hand side of Equation (18),  $d\mathcal{J}/d\mathbf{X}$ , the SU2\_CFD\_AD executable is used. The other two derivatives,  $d\mathbf{X}/d\mathbf{X}_{surf}$  and  $d\mathbf{X}_{surf}/d\alpha$ , are obtained through the SU2\_DOT\_AD executable [26].

To solve for  $d\mathcal{J}/d\mathbf{X}$ , notice that the objective is a function of the state variables  $\mathbf{U}$  and the mesh  $\mathbf{X}$ , i.e.,  $\mathcal{J}(\mathbf{U}, \mathbf{X})$ . Moreover,  $\mathbf{U}$  is also a function of  $\mathbf{X}$ , i.e.,  $\mathbf{U}(\mathbf{X})$ . Hence, the derivative of the objective function with respect to  $\mathbf{X}$  can be written as Equation (19) [31][21].

$$\frac{d\mathcal{J}}{d\mathbf{X}} = \frac{\partial \mathcal{J}}{\partial \mathbf{X}} + \frac{\partial \mathcal{J}}{\partial \mathbf{U}} \frac{d\mathbf{U}}{d\mathbf{X}} \quad (19)$$

Where the partial derivatives are relatively easily computed using Algorithmic Differentiation (AD) [21], however, the total derivative  $d\mathbf{U}/d\mathbf{X}$  becomes much more expensive due to the required re-evaluation of  $\mathbf{U}$  for a perturbation of  $\mathbf{X}$ . To compute the total derivative  $d\mathbf{U}/d\mathbf{X}$ , it is assumed that the current design iteration is a steady-state solution which is fully converged. In other words, the residuals of the governing equations  $\mathbf{R}(\mathbf{U}(\mathbf{X}), \mathbf{X})$  are zero. This can be used to differentiate the residuals as given in Equation (20).

$$\frac{d\mathbf{R}}{d\mathbf{X}} = \frac{\partial \mathbf{R}}{\partial \mathbf{X}} + \frac{\partial \mathbf{R}}{\partial \mathbf{U}} \frac{d\mathbf{U}}{d\mathbf{X}} = 0 \quad \rightarrow \quad \frac{\partial \mathbf{R}}{\partial \mathbf{U}} \frac{d\mathbf{U}}{d\mathbf{X}} = -\frac{\partial \mathbf{R}}{\partial \mathbf{X}} \quad (20)$$

Assuming that the matrix  $\partial \mathbf{R}/\partial \mathbf{U}$  can be inverted, the right hand side of Equation (20) can be substituted into Equation (19), giving Equation (21).

$$\frac{d\mathcal{J}}{d\mathbf{X}} = \frac{\partial \mathcal{J}}{\partial \mathbf{X}} - \frac{\partial \mathcal{J}}{\partial \mathbf{U}} \frac{\partial \mathbf{R}^{-1}}{\partial \mathbf{U}} \frac{\partial \mathbf{R}}{\partial \mathbf{X}} \quad (21)$$

Then it is worth introducing the adjoint vector ( $\psi$ ), see Equation (22), which can be determined by the adjoint equation Equation (23).

$$\psi^T = \frac{\partial \mathcal{J}}{\partial \mathbf{U}} \frac{\partial \mathbf{R}^{-1}}{\partial \mathbf{U}} \quad (22) \quad \frac{\partial \mathbf{R}^T}{\partial \mathbf{U}} \psi = \frac{\partial \mathcal{J}^T}{\partial \mathbf{U}} \quad (23)$$

Using the solution for the adjoint vector, the total derivative can be found using Equation (24).

$$\frac{d\mathcal{J}}{d\mathbf{X}} = \frac{\partial \mathcal{J}}{\partial \mathbf{X}} - \psi^T \frac{\partial \mathbf{R}}{\partial \mathbf{X}} \quad (24)$$

## G. Optimizer

The IPOPT algorithm makes use of the barrier method to solve large-scale nonlinear optimization problems of the general form in Equation (25), where  $\mathcal{J}$  is the objective function,  $\alpha$  the design vector,  $\mathbf{c}(\alpha)$  the vector of equality constraints and  $\alpha_L$  and  $\alpha_U$  are the lower and upper bounds. To implement the barrier function Equation (25) is reformulated as in Equation (26), where  $\xi_j$  is the barrier parameter, which converges to zero for an optimal solution. Then the optimization problem is solved using a line-search filter method. For more information on the algorithm and implementation thereof, the reader is referred to the paper of Wächter and Biegler [33].

$$\begin{aligned} \min_{\alpha \in \mathbb{R}^n} \quad & \mathcal{J}(\alpha) \\ \text{s.t.} \quad & \mathbf{c}(\alpha) = 0 \\ & \alpha_L \leq \alpha \leq \alpha_U \end{aligned} \quad (25) \quad \begin{aligned} \min_{\alpha \in \mathbb{R}^n} \quad & \phi_{\xi_j}(\alpha) = \mathcal{J}(\alpha) - \xi_j \sum_{i \in I_L} \ln(\alpha^i - \alpha_L^i) - \xi_j \sum_{i \in I_U} \ln(\alpha_U^i - \alpha^i) \\ \text{s.t.} \quad & \mathbf{c}(\alpha) = 0 \end{aligned} \quad (26)$$

The objective function in the optimization problem is defined as the mal-distribution factor in the channels connected to the manifolds, see Equation (27) [15].  $\dot{m}_i$  is the measured mass flow in the  $i^{\text{th}}$  channel,  $\bar{m}$  the average mass flow through the parallel channels calculated using Equation (28) and  $n$  the number of parallel channels.

$$\mathcal{J} = \sqrt{\frac{\sum_{i=1}^n \left( \frac{\dot{m}_i - \bar{m}}{\bar{m}} \right)^2}{n-1}} \quad (27) \quad \bar{m} = \frac{\sum_{i=1}^n \dot{m}_i}{n} \quad (28)$$

As discussed in subsection II.B, the calculation of the mass flow in each channel is performed at given control surfaces placed 5 mm from the outlet of the lateral channels.

The entries of the design variable vector in the optimization problem are the coordinates of the FFD nodes created in the initialization process. In SU2, the movement of the FFD box nodes has to be defined separately, such that the direction along which each node may move can be specified. In this paper, three different configurations of the design variable vector have been tested. The first one allows each node to move along a radial path with respect to the center of the bottom surface of the FFD box. With the second configuration, each node is defined twice such that the nodes may move freely on the y and z-plane. The third configuration differs from the second one for the fact that also a FFD box around the combining manifold is included.

To ensure a good connection between the inlet and the deformed dividing manifold, the first two planes in the x-direction of the FFD box, have been excluded from the design vector. Furthermore, to ensure a good connection between the dividing manifold and the parallel channels, the first three planes in the y-direction of the FFD box, have been excluded. The same limitations have been applied when defining the design vector of the combining manifold. That is, the last two planes in the x-direction and the last three planes in the y-direction have been excluded. This resulted in a design vector of 5040, 10080 and 26850 nodes for the first, second and third design vectors respectively. The maximum translation of a node has been set to -5 mm and 5 mm given the inlet radius (5.25 mm) of the manifold. Moreover, no constraints were used during the optimization procedure.

### III. Verification

To ensure that the method was correctly implemented, several verification steps have been performed. The first one was a mesh convergence study, to ensure that a correct mesh size throughout the simulations would be used. Secondly, for all performed simulations in this paper, a solver convergence check was performed, to ensure the obtained solution has stabilized. To verify the adjoint solver convergence, the gradients obtained by the adjoint solver were compared to gradients estimated through the forward difference method. This verification step was performed only once, due to the required computational time. Finally, the optimality of all obtained designs was evaluated, to ensure the obtained design would qualify as optimal.

#### A. Mesh Convergence

From initial tests, it was found that the flow solution is most sensitive to the mesh size used in the surface meshes. This resulted in a maximum volume mesh size of 2 mm with the defined refinement zones as discussed in section II. To determine which mesh size to use for the different parts in the mesh, first, a mesh was created with the largest surface mesh sizes for which the flow solver would converge. This resulted in a mesh of 996831 nodes, see Table 4 for the mesh size of the various regions of the computational domain.

**Table 4 Maximum surface mesh size settings for which the flow solver converged.**

Part	Mesh Size [mm]
Inlet	0.5
Dividing Manifold Surface	0.5
Dividing Manifold-Channel Fillet	0.125
Channel Surfaces	0.5
Combining Manifold-Channel Fillet	0.125
Combining Manifold Surface	0.5
Outlet	0.5
Mesh size channel refinement	0.25

The mesh sizes of each part were decreased until a discrepancy smaller than 1% was obtained in the results with respect to the previous solution. The larger mesh size is then chosen for the CFD model, such that the number of nodes is minimized while preserving the accuracy of the simulations. First, the mesh size of the inlet, outlet and channel walls was decreased, Figure 4 shows the relative variation in the objective function. From this experiment, a mesh size of 0.25 mm for all these regions was selected. Second, the mesh was progressively refined in the area close to the inlet of the

channels. From this experiment, it was found that a mesh size of 0.25 mm for this region of the mesh was satisfactory, see Figure 5. Note that in both Figure 4 and Figure 5 the values of the objective function are normalized with respect to the solution obtained for the smallest mesh size. This is done such that it clearly can be seen that the chosen mesh size differs by less than 1% with respect to the finest tested mesh size. The mesh size of the manifold surfaces and manifold-channel interfaces was not further reduced, as any modification either resulted in prohibitively large meshes or caused the flow solver to diverge in the case of a coarser mesh.

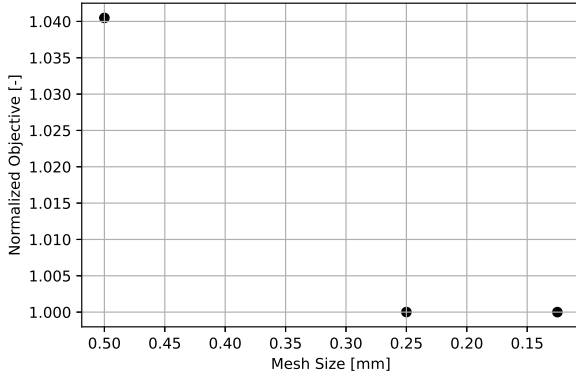


**Fig. 4** Mesh convergence results for decreasing the inlet, outlet and channel wall surface mesh size.

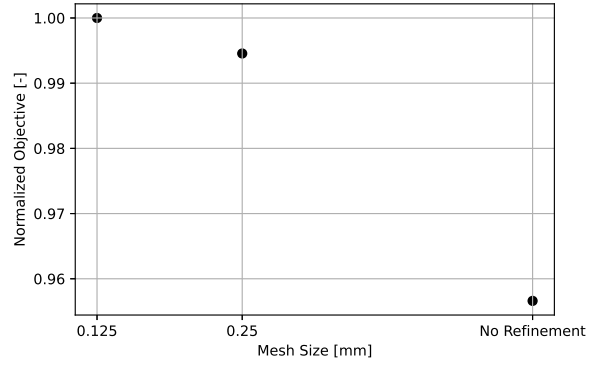


**Fig. 5** Mesh convergence results for decreasing the mesh size of the channel refinement zone.

## B. Solver convergence

To ensure the solutions of the flow and adjoint solver have sufficiently stabilized, a convergence level of at least three orders of magnitude had to be reached. This level of convergence has been checked for all results discussed in section IV. It can be assumed that all results have converged according to the stated criteria, except if stated otherwise. The plot of the residuals of the various simulations can be found in Appendix B.

## C. Gradient Verification

The gradients obtained through the adjoint method are dependent on the convergence of both the flow and adjoint solver. Therefore the obtained gradients of the adjoint method have been compared to the gradients obtained from a forward difference (FD) method, dependent only on the convergence of the flow solver. The gradients of the FD method were obtained with Equation (29), where a step size ( $h$ ) of  $1e-3$  was used. As testing the gradients of all FFD nodes becomes prohibitive, due to the large number of design variables, 15 randomly selected nodes were used for the comparison, see Figure 6. It can be seen that most gradients are matched with high accuracy, except the gradients associated with the 8<sup>th</sup> and 14<sup>th</sup> node, where a larger relative discrepancy is observed. However, this discrepancy is acceptable as the majority of the obtained gradients match within a 1% relative error. Therefore, it can be stated that the chosen convergence tolerance, which implies that the solution residuals must decrease by three orders of magnitude, is sufficient in the scope of this paper.

$$f'(x) = \frac{f(x_{i+1}) - f(x_i)}{h} \quad (29)$$

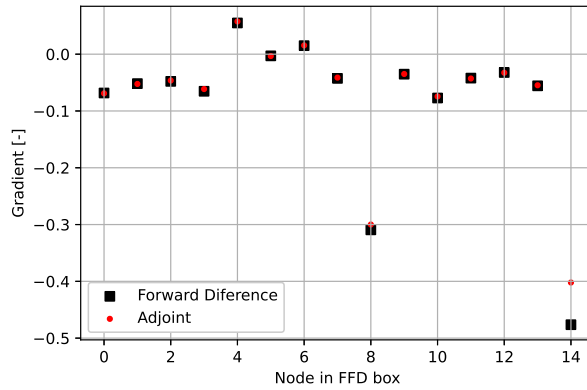


**Fig. 6 Gradients of the injective function at 15 randomly selected FFD nodes as calculated by the FD method (black) and the adjoint method (red).**

#### D. Optimization convergence

To verify that the obtained design of the optimization procedure could be a local optimum, a set of checks is performed. First, it is checked if the objective function follows a monotonically decreasing path throughout the procedure, as in Figure 7. A non-monotonic path would suggest that better designs exist within the current optimization procedure that have not been investigated. From Figure 7 it can be seen that the radial-based optimization procedure, discussed in section IV, follows such a path. Moreover, a steep drop in the objective function can be seen around the 10<sup>th</sup> iteration. This drop is due to a restart of the procedure, as the used cluster has a run-time limit.

Secondly, it is checked whether the obtained design is limited by the bounds, as in Figure 8, since the initial bounds as discussed in section II are based on an initial guess. If an optimal design has multiple design variables restricted by bounds, the bounds would require a reevaluation. In Figure 8, it can be seen that the optimal design for the radial-based optimization has no variables that reached the bounds.

Lastly, it is checked whether the first-order necessity condition applies to the obtained design. In other words, all gradients of the final solution should be zero. This check provides information on the potential for further optimization of the obtained design. A design with all gradients at zero means that every perturbation of a design variable causes a worse design. However, due to the large number of variables and the complexity of the problem, it will be very hard to obtain such a perfect solution. Hence, this check consists of verifying that a significant portion of the design variables have moved towards zero for the obtained design. In Figure 9, the results of such a check for the radial-based optimization can be seen, where to facilitate the legibility of the chart, only the gradients of one out of one hundred design variables are displayed. It can be noticed that most of the gradients indeed moved towards zero.

The second-order sufficiency condition must be satisfied to ensure that the obtained design is an actual optimum. However, this requires information on the Hessian of the problem, which is not available with the adopted procedure. Hence, if all the conditions stated above are satisfied, it can still be the case that the obtained design is a local optimum.

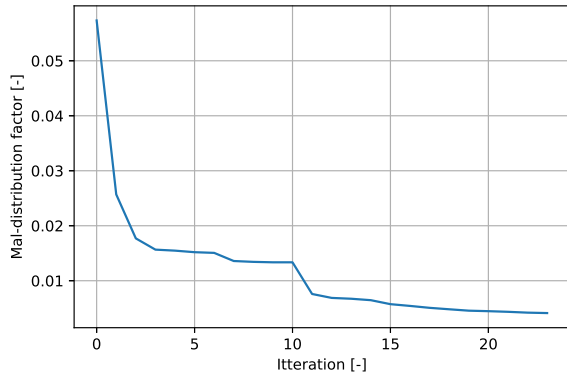


**Fig. 7 Objective for each design iteration of the radial-based optimization procedure.**

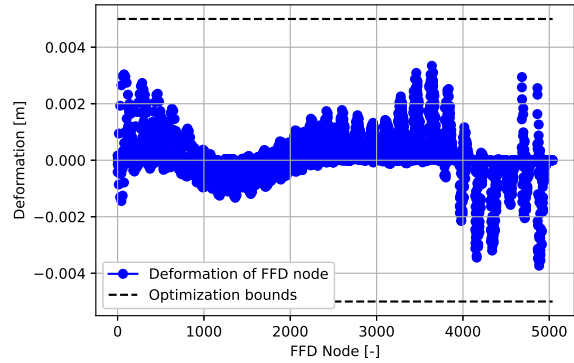


**Fig. 8 The deformation of all FFD nodes (blue dots) in the radial-based optimization procedure with the given bounds (grey striped line).**

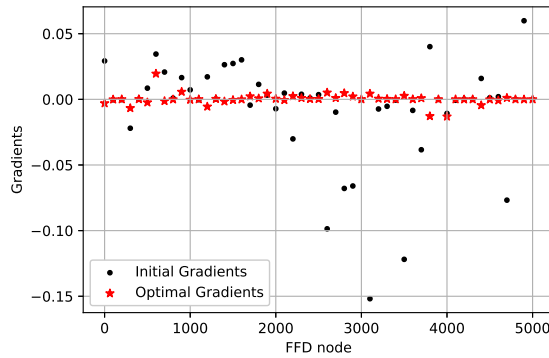


**Fig. 9 Gradients of the objective function at every 100<sup>th</sup> FFD node in the design vector for the radial-based optimization procedure. Black dots represent the gradients of the initial design and red stars represent the gradient of the optimized design.**

## IV. Results and Discussion

All the results presented below were obtained using a Python script that automatically runs ParaView<sup>7</sup>. In this Python script, first, the flow solution pertaining to the dividing and combining manifold were separated from each other. Then either the dividing or combining manifold was sliced into several cross-sections, where the slices were strategically placed such that they fall in the middle of two lateral channels. In Appendix C, the exact locations at which the solution is sampled can be found.

### A. Yang-based design vs. London-based design

In the preliminary design phase, the performance of a manifold with a tubular shape with a constant diameter was assessed and compared to that of a manifold shaped by adapting London's procedure, as explained in subsection II.A. It was found that the manifold with a constant diameter, if sized according to Yang's design procedure exhibits a mal-distribution factor of 0.085. Whereas the manifold featuring a profile defined according to London's criteria had a better performance, with a mal-distribution factor of 0.057. Thus, London's design method provides roughly a 32.9% decrease in the overall mal-distribution. However, the perfect mass flow distribution theoretically achievable with London's

<sup>7</sup><https://www.paraview.org/download/>

guidelines is not obtained. In Figure 10 the area, velocity and pressure distribution along the length of both manifold designs are plotted.

From Figure 10 it can be seen that for Yang's design, as the area along the manifold remains constant, the flow velocity along the manifold keeps reducing, as expected, due to the continued loss of mass flow through the lateral channels. From the pressure profile, it can be seen that between  $x=0$  and  $x=0.016$  (the start of the first lateral channel) the pressure decreases. This can be explained by friction losses in the pipe. Afterwards, it can be seen that the pressure in the manifold increases due to the decreasing mass flow rate and the consequent flow deceleration. However, the rate of pressure increase gradually decreases. This can be explained by the presence of friction effects and the approaching of the end of the manifold. For the manifold shaped according to London's guidelines, the flow cross-section normal to the lateral channels decreases. As the cross-section reduces at  $x=0.016$  an increase in velocity is observed, till a distance from the inlet corresponding to  $x=0.047$ . Afterwards, the velocity quickly decreases to zero, due to the presence of the end of the manifold. The pressure curve shows a trend that differs from that observed for the design based on Yang's guidelines. First, the pressure decreases due to friction effects as for the tubular manifold. Then the pressure decreases significantly due to both the increased velocity and related friction effects. Finally, the pressure quickly increases when the velocity decreases near the end. It is worth noticing the larger inlet pressure estimated for the manifold shaped according to London's design procedure. This implies that such a manifold is characterized by larger pressure drops than the tubular one. Notably, the pressure drop is about 21% higher with the design solution obtained by applying London's method

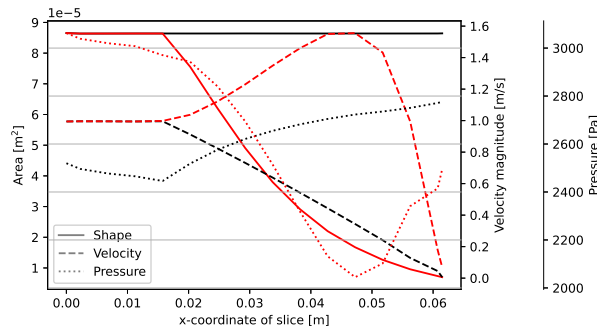


**Fig. 10 Area, velocity and pressure along the length of the dividing manifold for Yang-based design (black lines) and London-based design (red lines)**

It is clear that for an equal distribution of mass flow, the pressure distribution in the dividing manifold has to be equal to that in the combining manifold. In Figure 11 the pressure distributions in both manifolds and design solutions are plotted. It can be seen that, for both design methods, the pressure distribution in the combining manifold is equal. The small observed differences could be the results of numerical approximations due to differences in the meshes, the level of convergence of the solution, etc. Moreover, it can be seen that the pressure distribution in the dividing manifold designed with London's guidelines follows the pressure distribution in the combining manifold better. This effect can also be seen from the fact that the pressure drop  $\Delta P$  in the lateral channels varies in a smaller range than that observed for the tubular manifold.

The relation between the pressure and the mass flow distributions can be seen in Figure 12: the larger the pressure loss in a channel, as presented in Figure 11, the larger the mass flow and vice versa. This observation holds true except for the first channel of the manifold with London's profile. It would be expected that the mass flow through the first channel is larger than in the second channel, due to the higher pressure drop. Furthermore, from Figure 12 and Figure 13, it can be inferred that there is a relation between the size of the separation bubble at the channel inlet and the mass flow in each channel. Moreover, it can be noticed that the overall higher velocity in the manifold with London's profile causes larger separation bubbles, which might explain the overall larger pressure drop over the entire flow domain.

In summary, it can be concluded that London's design method provides a 32.9% improvement in the mal-distribution factor compared to Yang's design method. While London's method, as applied in this paper, does not achieve the assumed perfect mass flow distribution, it's crucial to note that this method was not proposed by the authors for axial-symmetric manifolds. Moreover, London's design method results in a 21.5% increase in the pressure drop over the entire system compared to Yang's method.

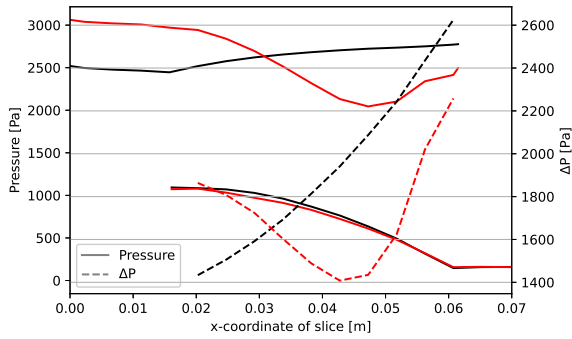


**Fig. 11** Pressure distribution in the dividing manifold (top) and combining manifold (bottom) and the resulting pressure loss in the lateral channels. The black lines represent Yang's design and the red line represents London's design.

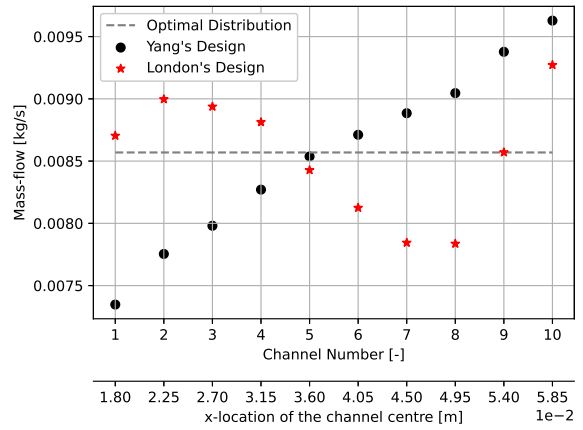
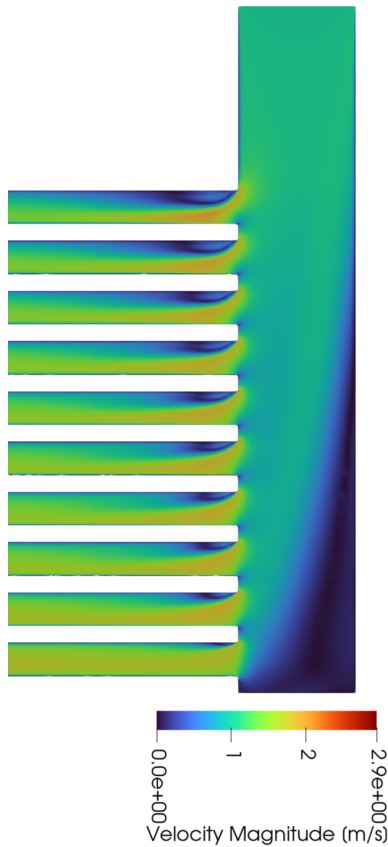
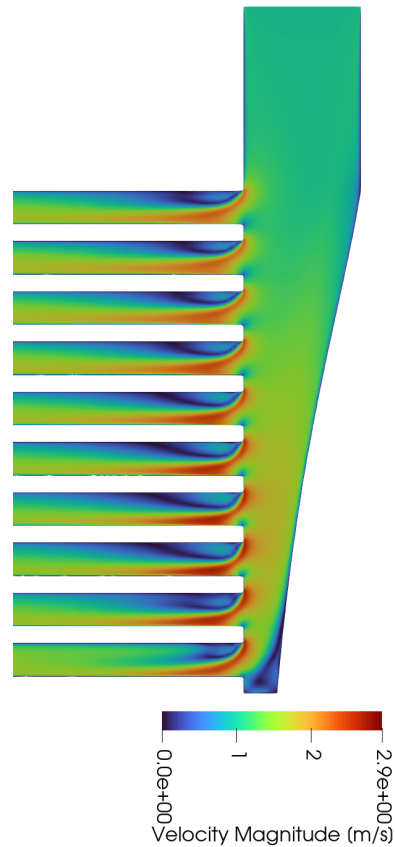


**Fig. 12** Mass flow rate in each channel for Yang's design (black) and London's design (red).



**(a)** Result for design based on Yang's method.



**(b)** Results for design based on London's method.

**Fig. 13** Velocity magnitude (in m/s) in the dividing manifold for the  $z=0.0125$  m plane.

## B. Optimization results

As discussed in section II, three design optimizations have been performed, i.e., 1) the optimization of only the dividing manifold with an FFD box parametrization whose nodes can only move in the radial direction ('radial-based'); 2) the optimization of only the dividing manifold where the design variables are the FFD nodes which can move along the y and z axis of the geometry ('cartesian-based'); and 3) the simultaneous optimization of both the dividing and combining manifold with an FFD box parametrization identical to that of the second optimization study ('dual-manifold optimization'). For the first two optimization studies, the initial design is as presented in Figure 2, i.e., a dividing manifold shaped according to London's design method. Several attempts have been made to utilize an initial dividing manifold with a constant cross-section; however, these efforts yielded unsuccessful results. More details can be found in Appendix E. For the dual-manifold optimization run, the combining manifold was also shaped according to London's design method, see Appendix A.

### 1. Dividing manifold optimization

The optimization of the dividing manifold with a radial-based FFD box parametrization resulted in a mal-distribution factor of 0.004, which is 93% lower than that estimated for the baseline geometry shaped according to London's design procedure. For the optimization with a cartesian-based FFD box parameterization, a mal-distribution factor of 0.010 was found which represents an 82.5% reduction with respect to the baseline geometry. However, for the cartesian-based case, it proved difficult to obtain consistent convergence of the adjoint solver to the required tolerance discussed in section III. Hence, the obtained design is affected by uncertainty, as it is unknown whether the accurate gradients were estimated or not. However, the flow solver did converge, therefore the obtained design is still of interest. The area, velocity and pressure distribution for the baseline geometry and those obtained through optimization are reported in Figure 14.

From Figure 14 it can be noted that the optimal shape obtained with radial-based deformation has an increase in area, between  $x=0$  and  $x=0.02$ , causing a decrease in the velocity, whereas the design obtained with cartesian-based deformation has a slight decrease in area, resulting in an increased velocity compared to the initial design. The radially-deformed manifold shape then has a decrease in area compared to the baseline design between  $x=0.02$  and  $x=0.03$ . After this position, the area increases again till  $x=0.05$ . Moreover, from  $x=0.04$  onwards, it can be seen that both the optimal designs feature approximately the same shape. A top view of the resulting 3D shapes can be found in Figure 48, in Appendix D. Furthermore, it can be seen from Figure 15 that both the optimal designs do not exhibit a symmetric shape. It can also be seen in Figure 15d that the optimizer is trying to limit the height of the manifold near the end. Hence, it can be stated that the choice of limiting the minimum manifold height towards the end of the dividing manifold is detrimental to obtaining a uniform mass flow distribution.

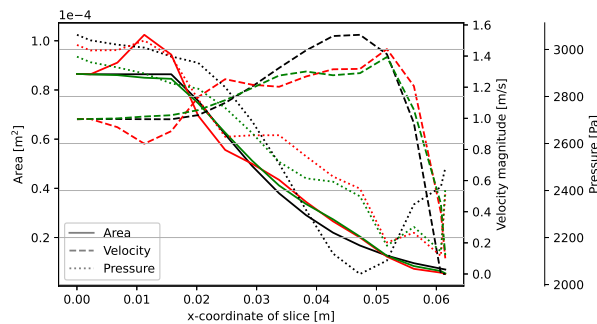


**Fig. 14** Area, velocity and pressure distribution along the length of the optimized dividing manifold. The black lines represent the baseline design, the red lines represent the optimal design obtained with radial-based parametrization of the manifold surfaces, and the green lines correspond to the design obtained with cartesian-based parametrization.

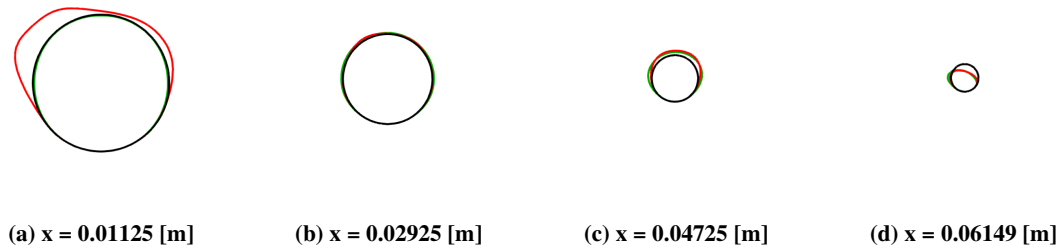


**Fig. 15** Cross sections of the optimized dividing manifold for the radial-based parametrization (red), the cartesian-based parametrization (green) and the baseline design (black).

The pressure distribution along the manifold and the resulting pressure difference between the dividing and combining manifold for both optimal designs can be seen in Figure 16. The resulting mass flow distribution across the lateral channels can be seen in Figure 17. It can be seen that the design obtained with a radial-based deformation results in slightly better pressure distribution and therefore has a more equal mass flow distribution. Furthermore, it can be seen that the pressure loss for the obtained designs is approximately equal to that of the baseline design. In Figure 18, it can be seen that the separation bubbles in the lateral channels cover a larger flow region, i.e. they extend further into the channel, for the design obtained through the cartesian-based deformation of the manifold surfaces. However, it must be noted that the design obtained through cartesian-based parametrization achieves 89% of the mal-distribution reduction observed for the solution of the optimization with the radial-based parametrization, with a smaller deformation. Hence, the aft part of the manifold is more sensitive to design changes than the front part.

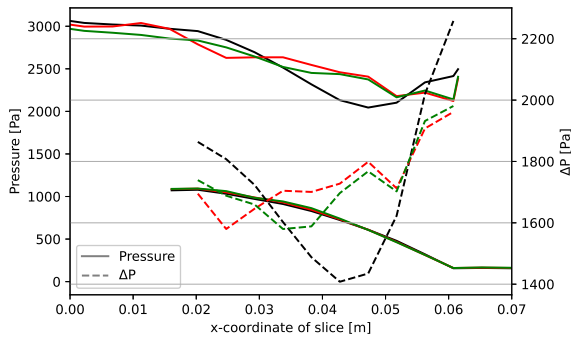


**Fig. 16** Pressure distribution in the dividing manifold (top) and combining manifold (bottom) and the resulting pressure loss in the lateral channels. The black lines represent the baseline design, the red lines correspond to the design obtained through the radial-based parametrization, and the green lines correspond to the design obtained with the cartesian-based parametrization.

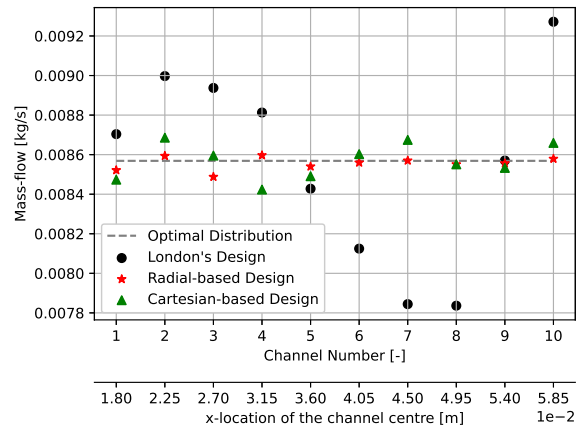
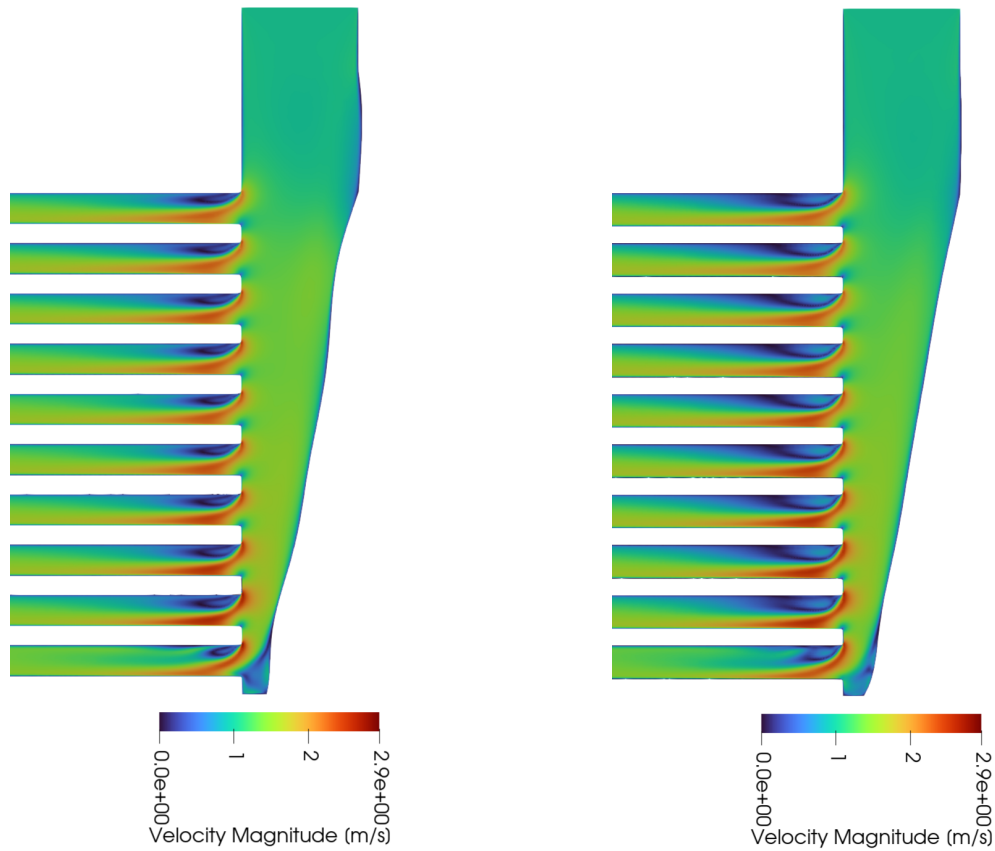


**Fig. 17** Mass flow rate in each channel for baseline design (black), the design obtained with radial-based parameterization (red) and the design obtained with cartesian-based parametrization (green).

## 2. Dividing and combining manifold optimization

The simultaneous optimization of both manifolds started from a different initial geometry, see Figure 36 in Appendix A. This initial geometry caused worse mass flow distribution across the channels, resulting in a mal-distribution factor of 0.251. However, the optimized solution has a nearly perfect mass flow distribution across all channels, essentially



(a) Results for the design obtained with radial-based parameterization. (b) Results for the design obtained with cartesian-based parameterization.

**Fig. 18** Velocity magnitude (in m/s) in the dividing manifold at a depth of  $z=0.0125$  mm (approximately the plane at the center of the manifold).

resulting in a null mal-distribution factor. Figure 19 shows the resulting area, velocity and pressure distribution for the dividing manifold, while Figure 20 shows the results for the combining manifold.

From Figure 19 it can be seen that the optimal shape initially follows a profile similar to that previously discussed in subsection IV.B.1, i.e., an increase in area at the beginning of the manifold. However, after the initial increase, the optimal shape follows a more London-like shape, with a larger decrease in area near the end of the manifold. From Figure 20 it can be seen that the adoption of a profile in the combining manifold mirroring that defined with London's procedure for the combining manifold causes a high-pressure drop at the start of the combining manifold. The optimized shape mitigates this by locally increasing the area of the combining manifold. From Figure 21, it can be seen that the optimized dividing manifold, in contrast to the previous results, features a symmetrical shape. However, the combining manifold does not as seen in Figure 22, moreover, the 3D model of the optimized manifolds can be found in Figure 49, in Appendix D.

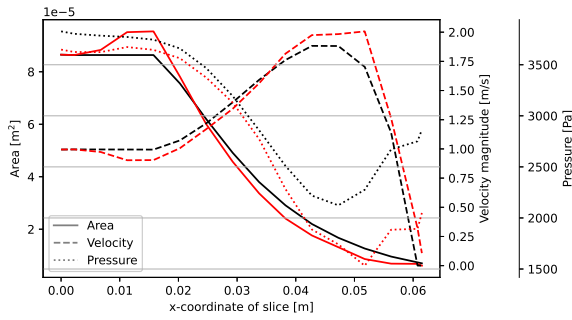


**Fig. 19** Area, velocity and pressure distribution along the length of the optimized dividing manifold (red) compared to the baseline design (black).

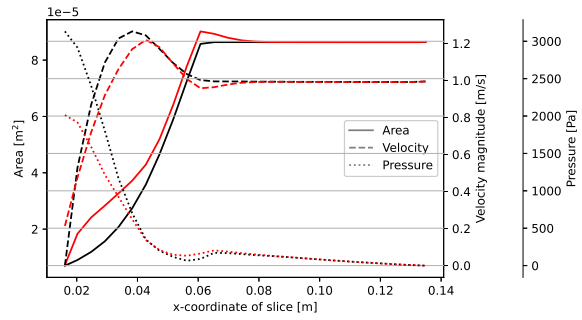


**Fig. 20** Area, velocity and pressure distribution along the length of the optimized combining manifold (red) compared to the baseline design (black).

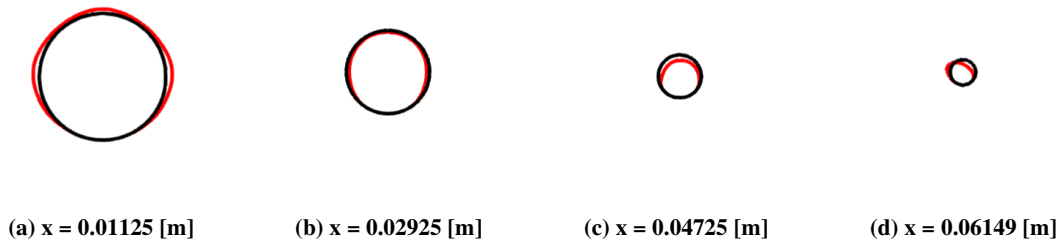


**Fig. 21** Cross sections of the optimized dividing manifold (red) and the baseline design (black), for the dual-manifold optimization.

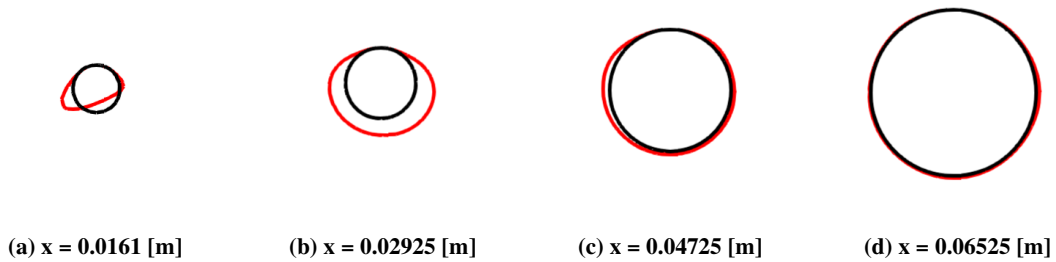


**Fig. 22** Cross sections of the optimized combining manifold (red) and the baseline design (black), for the dual-manifold optimization.

Furthermore, Figure 23 shows the pressure distributions for the initial and optimized design. From this figure, it becomes apparent why the mal-distribution is worse for the baseline case: the pressure drop in the lateral channels keeps increasing from the first channel to the last one. Conversely, the pressure drop in the lateral channels for the optimized design are more evenly distributed, resulting in an almost perfect mass flow distribution as proven in Figure 24. Moreover, it can be seen that adapting the flow cross-section along both the dividing and combining manifolds results in a larger pressure drop, also in the case this adaption is optimized.

The main changes in the pressure distribution are obtained in the last half of the dividing manifold, i.e., from  $x=0.035$  to  $x=0.061$ , and the first half of the combining manifold, i.e., from  $x=0.015$  to  $x=0.04$ . However, it is apparent from Figure 25, that the change in pressure distribution has a minimal effect on the qualitative flow distribution: the velocity

magnitude in the flow domain for the optimal solution seems identical to that estimate for the baseline design. This highlights the effect of the back pressure created by the combining manifold on the mass flow rate in the lateral channels.

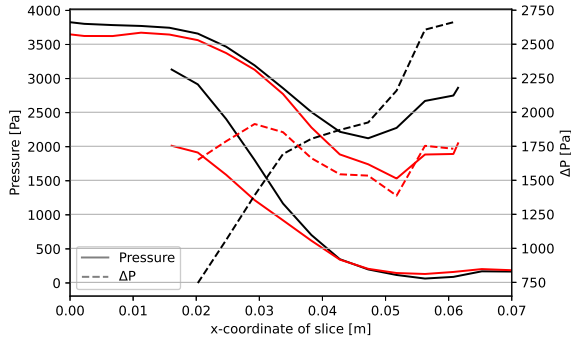


**Fig. 23** Pressure distributions in the manifolds and pressure loss in the lateral channels. The black lines represent the baseline design, red is the design of the dual-manifold optimization.

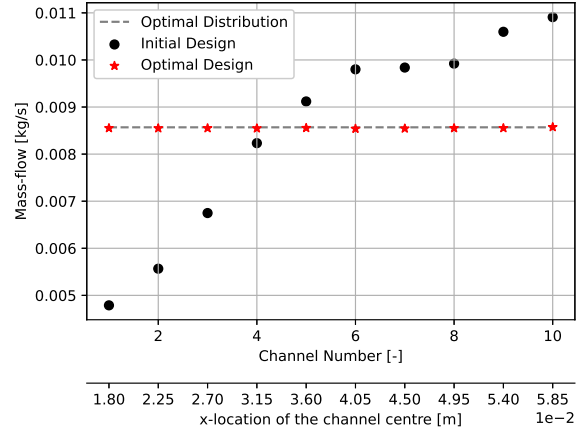
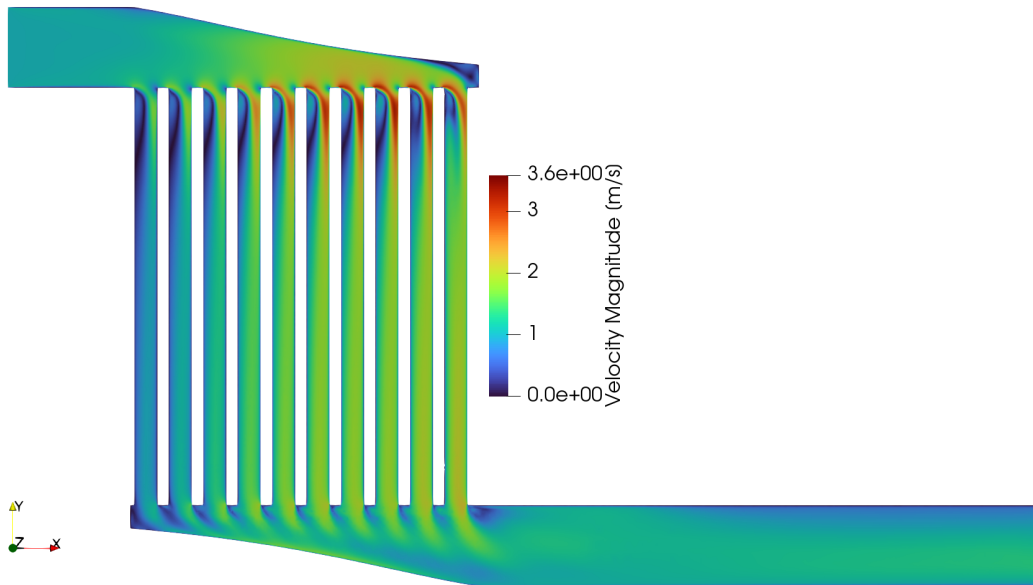


**Fig. 24** Mass flow rate in each channel for the baseline design (black) and the design of the dual-manifold optimization (red).

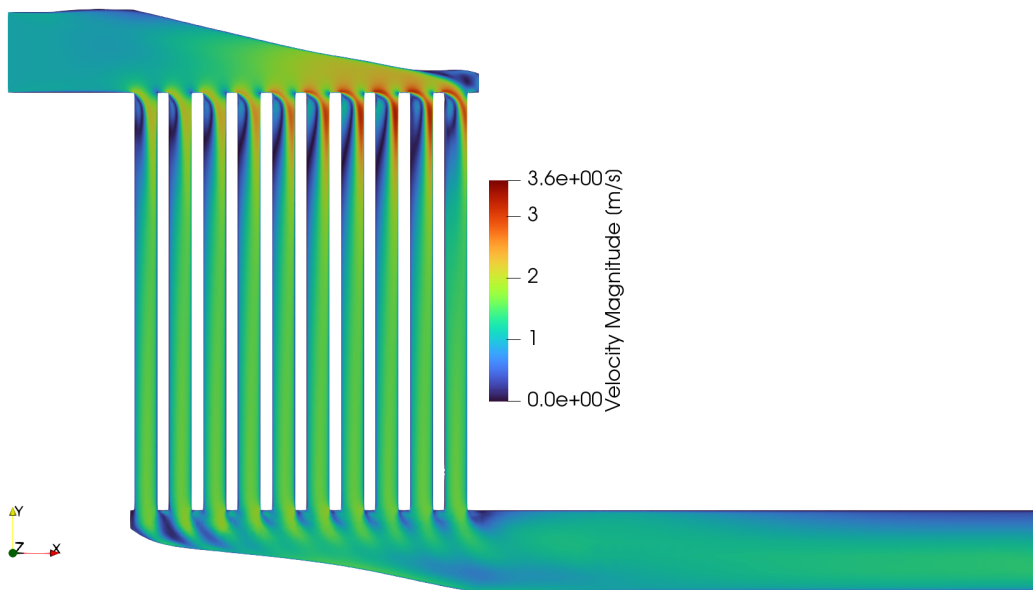
Finally, the results of the three optimization runs are summarized in Table 5, indicating that shape optimization consistently provides an improved design compared to the currently available methods. However, the proposed design method is computationally expensive and time-consuming, as proper tuning of the CFD models is needed to get consistent solver convergence. It can be seen that the optimization of both manifolds simultaneously results in the best mass flow distribution. Nevertheless, it's important to highlight that this design leads to the highest overall pressure drop across the flow domain. Moreover, the design obtained with cartesian-based parametrization required only a small adjustment of the baseline geometry obtained with London's method while achieving at the same time an 82.5% improvement of the mal-distribution factor. Hence, significant improvements in mass flow distribution could be achieved with small modifications of the design method of London, without a significant increase in pressure loss. However, it should be investigated further if enforcing symmetry in the manifold shape can have a significant impact on the mass flow distribution. Finally, notice that asymmetric manifold shapes may be adopted only if additive manufacturing is a viable option for the production of the device of interest. Thus, enforcing manifold symmetry in the optimization may be required to ensure the manufacturability of the obtained shapes.

**Table 5** Summary of the obtained objectives and pressure loss for different designs.

Design	mal-distribution factor	Compared to Design #1	Compared to Design #2	$P_1 - P_0$
Tubular manifolds - Yang's method	0.085	-	49.1%	2520
Dividing manifold - London's method	0.057	-32.9%	-	3062
Shape opt. - Cartesian-based FFD	0.010	-88.2%	-82.5%	2969
Shape opt. - Radial-based FFD	0.004	-95.3%	-93%	3019
Shape opt. of both manifolds	0	-100%	-100%	3648



(a) Baseline design.



(b) Optimal design.

**Fig. 25** Velocity magnitude (in m/s) along a plane positioned at  $z=0.0125$  mm (approximately the plane at the center of the manifolds).

### C. Off-Design Analysis

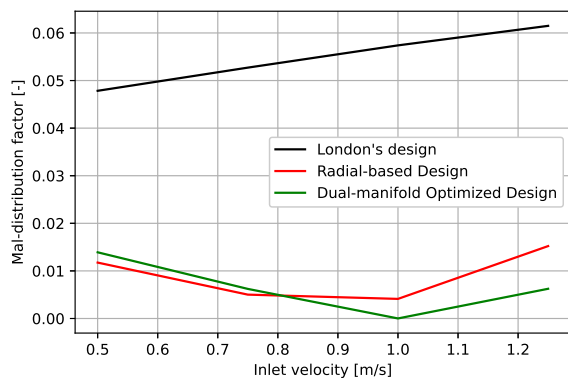
It is obvious that the flow conditions at the manifold inlet may significantly affect the mass flow mal-distribution. Moreover, most manifolds operate under varying flow conditions. However, the shapes obtained before are optimal for specific flow conditions. Hence, the optimized manifolds might perform worse than the baseline design when operated under conditions different from those considered in the optimization. To verify this possibility, the off-design performance of the optimized manifolds has been investigated, to gain insight into the sensitivity of the optimized designs to the flow conditions. To this purpose, CFD simulations were performed with various inlet flow velocities, namely 0.5, 0.75 and 1.25 m/s. It is worth recalling that the optimization was carried out for an inlet velocity in the dividing manifold of 1 m/s. The results of these off-design tests can be seen in Figure 26, Figure 27 and Table 6. The design obtained with the cartesian-based FFD exhibited inconsistent solver convergence for the different inlet velocities, preventing a full comparison with the other design. Consequently, this design was excluded from the comparison.

Figure 26 shows the variation of the mal-distribution factor with respect to the different initial velocities for the different optimized designs. It can be seen that the manifold shaped according to London's method performs better for smaller velocities. It is believed that this behaviour is due to the assumed pressure drop over the lateral channels in Yang's method and the assumed perfect mass flow distribution in London's method.

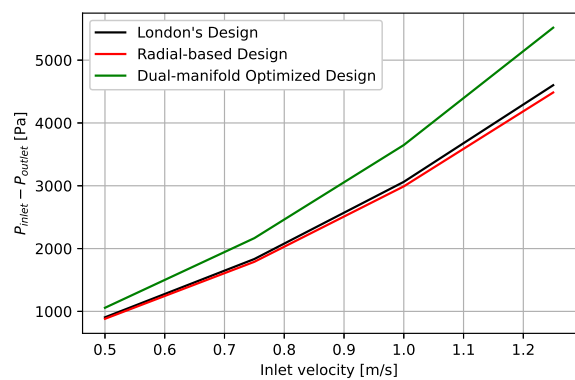
Furthermore, the mal-distribution factor is still significantly larger for the manifold shaped according to London's procedure compared to the optimized designs, regardless of the inlet flow velocity. However, the mass flow rate distribution for the optimized designs is relatively more sensitive to the flow conditions than for the manifold designed with London's method, as seen in Table 6. The relative drop in performance for the design resulting from the simultaneous optimization of both manifolds is not shown here as the objective function value for the on-design conditions is effectively 0, which would result in extremely high numbers, bearing no physical meaning.

Figure 27 shows the variation of the pressure drop with inlet velocity. It can be seen that the trend of the pressure loss with the flow velocity is similar for all design solutions. Notably, the larger the inlet velocity the larger the pressure loss in the system. As mentioned in the previous section, the solution obtained by optimizing both manifolds simultaneously had worse performance in terms of pressure drop. In off-design conditions, this effect becomes worse when the inlet velocity is increased, whilst the design obtained with a radial-based FFD remains similar to that of the baseline geometry defined with London's procedure. Hence, there is no practical advantage in adopting complex shapes for the outlet manifold.

In summary, it can be stated that for all the tested inlet velocities the optimized designs have a better mal-distribution factor. However, the relative drop in performance in off-design conditions is worse than for the baseline geometry. Moreover, it is concluded that the pressure drops changes with the inlet velocity in a similar way for all solutions. Due to the excellent flow distribution achieved by optimizing both manifolds simultaneously, it is recommended to implement a multi-objective optimization procedure if the optimization of the outlet manifold shape is included in the design procedure, where the objectives are the minimization of both the flow mal-distribution and pressure drop.



**Fig. 26** Flow mal-distribution in off-design conditions for the baseline design (black), the optimal design obtained with radial-based parameterization (red) and that resulting from the simultaneous optimization of both manifolds (green).



**Fig. 27** Pressure loss in off-design conditions for the baseline design (black), the optimal design obtained with radial-based parameterization (red) and that resulting from the simultaneous optimization of both manifolds (green).

**Table 6 Summarized results of the off-design analysis.**

Design	V=0.5 m/s	V = 0.75 m/s	V = 1.0 m/s	V = 1.25 m/s
Objective values in off-design				
London's Design	0.048	0.053	0.057	0.061
Radial-based Design	0.012	0.005	0.004	0.015
Double-optimized Design	0.013	0.006	0	0.006
Difference in objective compared to London				
Radial-based Design	-75%	-91%	-93%	-75.4%
Double-optimized Design	-72.9%	-88.7%	-100 %	-90.2%
Difference in objective compared to on-design				
London's Design	-15.8%	-7%	-	7%
Radial-based Design	200%	25%	-	275%
Double-optimized Design	-	-	-	-
Pressure loss values for off-design [Pa]				
London's Design	905	1834	3062	4601
Radial-based Design	882	1790	3019	4485
Double-optimized Design	1057	2166	3648	5517

**D. Effects of inlet velocity on optimization results**

To find if there is a trend in the optimal designs with the inlet flow velocity, a second test case was analyzed, where the initial design was created and optimized according to the same procedure previously discussed. The initial inlet velocity for this test case is 1.25 m/s. Test cases with much higher ( $V=2.5$  m/s) or lower ( $V=0.4$  m/s) velocities than those caused in the first test case (1 m/s) were not analyzed due to problems with the convergence of the flow solver. For this new test case, an inlet diameter of 8.5 mm was found appropriate by applying the method described in section II. The baseline shape of the dividing manifold was then defined with London's method, see Appendix A for more details about the geometry

For the baseline design, a mal-distribution factor of 0.126 was estimated through a CFD simulation, which is a 121% increase compared to the baseline design of the previous test cases. In Figure 28 the area, velocity and pressure distribution for the dividing manifold of the baseline design of both test cases (test case 1  $V_{inlet} = 1$  m/s; test case 2  $V_{inlet} 1.25$  m/s) are compared. In Figure 29 the pressure distributions in the dividing and combining manifold can be seen. It becomes clear that the difference in performance mainly comes from the change in pressure distribution in the combining manifold, which increased due to the decrease in diameter compared to the first test case. This results in a large  $\Delta P$  increase between  $x=0.042$  and  $x=0.061$ , whose effect on the mass flow distribution is shown in Figure 33.

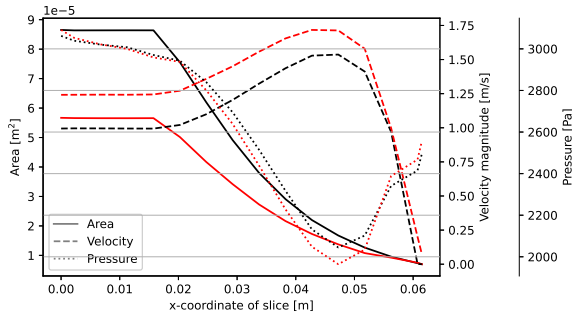


**Fig. 28** Area, velocity and pressure distribution along the length for the baseline dividing manifold design for test case 1 (black) and 2 (red).

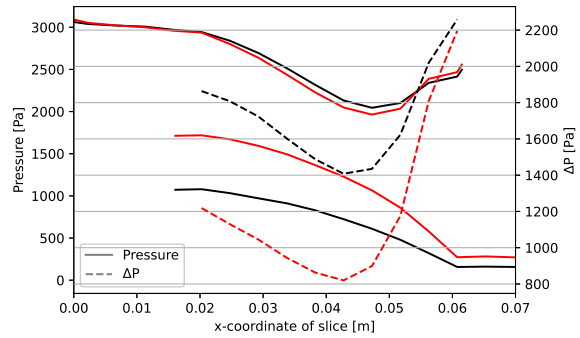


**Fig. 29** Pressure distribution in the manifolds and the resulting pressure loss in the lateral channels for test case 1 (black) and 2 (red).

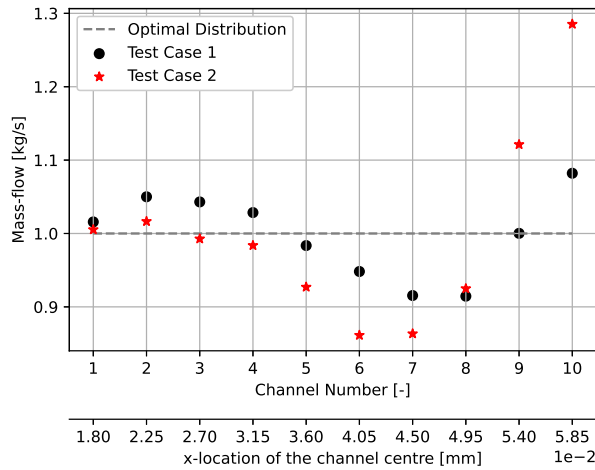


**Fig. 30** Mass flow rate in each channel for the baseline design of test case 1 (black) and 2 (red).

The optimization of the manifold for test case 2 was performed using a design vector whose nodes can only move along the y and z axes. The shape and pressure distribution of the optimal design is presented in Figure 31 and Figure 32. The corresponding minimum flow mal-distribution factor is 0.011 which is 91.3% lower than the base line design. The top view of the obtained optimal design can be found in Figure 50 in Appendix D. From Figure 31, it can be seen that the optimized design has an increase in flow area between  $x=0.0$  and  $x=0.018$ , in line with the results obtained for the deciding manifold of test case 1. Furthermore, the optimized design shows a larger area compared to the baseline design within the range  $x=0.03$  to  $x=0.048$ . In contrast, it shows a reduced area between  $x=0.048$  and  $x=0.06$ , as in the optimal designs obtained for test case 1. However, the increase in area between  $x = 0.018$  and  $x=0.03$  has not been seen in any previous solution. Hence, it is not possible to generalize an optimum profile for the dividing manifold based on the results of the optimization for test cases one and two, though similar features are present in the optimal solutions.

In conclusion, it has been shown that the presented design method proved to be effective also for a different though similar test case. The main challenge in the analysis of test cases with different inlet velocities, and thus Reynolds numbers, is the convergence of both the CFD and adjoint solver. Moreover, the second test case shows that the optimization led to an optimum shape with several features in terms of area distribution similar to those of the optimal designs obtained for test case 1. Therefore, it is recommended to improve the robustness of the incompressible flow solver in SU2. Once this is achieved, it is recommended to test multiple test cases to extrapolate new design guidelines for HEX manifolds.

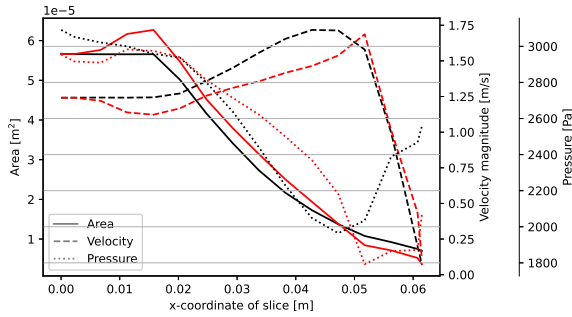


**Fig. 31** Area, velocity and pressure distribution along the length for the baseline design (black) and the optimal design (red).

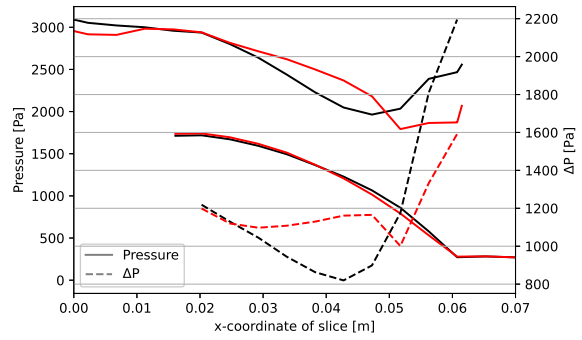


**Fig. 32** Pressure distribution in the manifolds and the resulting pressure loss in the lateral channels for the baseline design (black) and the optimal design (red).

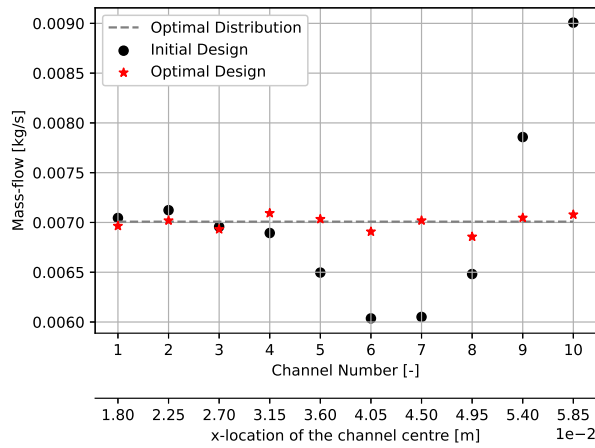


**Fig. 33** Mass flow rate in each channel for the baseline design (black) and the optimized design (red).

## V. Conclusion and Recommendations

The present work provides a novel design method for both dividing and combining manifolds by utilizing advanced techniques such as free-form deformation and the adjoint method. A 1<sup>st</sup>-order shape optimization has been implemented, using free-form deformation to parameterize the geometry, an incompressible RANS solver to evaluate the objective function, and the adjoint method to evaluate the gradients of the objective function.

An initial comparison of two existing design methods, i.e., Yang's and London's method, revealed that London's method provided a 32.9% improvement w.r.t. mal-distribution factor compared to Yang's method. However, this improvement comes at the cost of a 21.5% increase in pressure drop. Moreover, it was found that the design obtained through London's method provided the best baseline design for the proposed design method.

To test the proposed design method three different tests have been performed. First, a baseline design was obtained through London's method. This design was then optimized using the proposed method. Second, the obtained optimal designs were assessed in off-design conditions by varying the inlet flow velocity. Finally, the optimal design procedure was tested for an additional inlet flow velocity.

In the first design test case, three different definitions of the design vector were used. The first one allows the FFD nodes to move only in a radial direction from the bottom center of the FFD box, i.e., a radial-based parameterization method was used to optimize the dividing manifold. The second definition allowed the deformation to occur in the y and z-directions. This optimization strategy is defined as a cartesian-based parameterization. The third definition, allows the FFD nodes to move in the y and z-direction as the previous one, but includes nodes which parametrize the shape of both

the dividing and combining manifolds. This parameterization technique resulted in a simultaneous optimization of both manifolds. In this case, a new baseline design was defined using a London's method for both the dividing and combining manifold.

From the radial-based deformation, a mal-distribution factor of 0.004 was obtained which represents a 95.3% improvement compared to the baseline design. The cartesian-based deformation resulted in a mal-distribution factor of 0.010 which is an 82.5% improvement in performance. The simultaneous optimization of the dividing and combining manifold resulted in a mal-distribution factor of practically 0. While this optimization achieved the best mal-distribution factor, it also led to the highest overall pressure drop across the flow domain, marking a 19.1% increase compared to the baseline design. The design obtained with the cartesian-based FFD was found to have, overall, the best performance due to the notable improvement in the mal-distribution factor obtained with minimal design changes and no penalties in the pressure drop, which decreases by 3%.

The off-design test was performed assuming inlet flow velocities of 0.5, 0.75 and 1.25 m/s while the design inlet flow velocity was 1 m/s. From this test, it was found that all optimized designs had smaller mal-distribution factors in all operating conditions than the baseline design defined with London's method. However, the optimal designs exhibit a drop in performance in off-design conditions that is worse than that of the baseline design. Moreover, it was found that all designs showed similar changes in pressure drop due to the change in the inlet velocity.

The third test, i.e., the optimization of the dividing manifold for a different inlet flow velocity, was performed using a cartesian-based design vector. The baseline design for this new test case yielded a larger mal-distribution factor of 0.126, than in the first test case. The mal-distribution factor decreased to 0.011 using the proposed design method. Moreover, the resulting area distribution showed features similar to those of the optimal solution of the first test case. However, no one-to-one comparison between the obtained area distributions could be made.

While the presented design procedure consistently yields better-performing designs, it requires considerable computational resources and suffers also from solver convergence issues. Furthermore, all obtained designs show a low degree of asymmetry, which might prove to be infeasible in practical applications. Moreover, the increase in the pressure drop observed from the optimal manifolds should not be ignored.

Consequently, further research is recommended to minimize the challenges with the solver convergence. Once this is achieved, it could be useful to test multiple initial design configurations to assess the method thoroughly. It is also recommended to investigate the effects a symmetry constraint might have on the performance of the optimal designs. Moreover, it is recommended to test a multi-objective optimization strategy, where both the mal-distribution and pressure drop are minimized. Finally, it is recommended to validate the design method through experimental testing.

In summary, this paper lays the foundation for an improved design method of manifolds, yet further research is necessary to refine the proposed method for its practical implementation and broader applicability.

### **Acknowledgement**

I hereby want to thank Dr. C.M. De Servi and Dr.ir. N. Anand for their time, guidance and knowledge during this project. During this project, they provided me with critical feedback, technical support and several important insights. Moreover, I would like to thank S. Vermani for his help with several challenges I encountered in SU2.

I acknowledge the use of computational resources of DelftBlue supercomputer, provided by Delft High Performance Computing Centre (<https://www.tudelft.nl/dhpc>).

## Nomenclature

### Symbols

$c(\alpha)$	equality constraint vector
$D$	diameter manifold [m]
$f$	friction factor in the manifold [-]
$\mathcal{J}$	Objective function
$H$	flow resistance in the lateral channels [-]
$h$	velocity head [kg/m <sup>2</sup> ]
$L$	length of the manifold [m]
$P$	pressure [Pa]
$\mathbf{R}$	residual vector flow solver [-]
$Re$	Reynolds Number [-]
$\mathbf{U}$	state variable vector of the flow solver
$u_t$	friction velocity [m/s]
$V$	flow velocity [m/s]
$\bar{V}$	averaged velocity [m/s]
$X$	normalized location along the manifold [-]
$\mathbf{X}$	coordinate vector mesh nodes [-]
$y$	height combining manifold [m]
$y^+$	non-dimensional wall distance [-]
$Z$	normalized height of the dividing manifold [-]
$z$	height dividing manifold [m]

### Greek Symbols

$\alpha, \beta, \gamma$	parameters in Yang's design method [-]
$\alpha$	design vector
$\gamma_d$	static pressure recovery coefficient [-]
$\lambda$	area-ratio [-]

$\mu$	viscosity [kg/ms]
$\xi$	barrier parameter [-]
$\rho$	density [kg/m <sup>3</sup> ]
$\tau_w$	wall shear stress [Pa]
$\psi$	adjoint vector [-]

### Sub- & Superscript

0	initial
$c$	channel
$i$	inlet
$L$	Lower bound
$o$	outlet
$surf$	surface
$U$	upper bound
$vol$	volume
$\infty$	far up-stream

### Abbreviations

3D	Three Dimensional
CFD	Computation Fluid Dynamics
FADO	Framework for Aeronautical Design Optimization
FD	Forward Difference
FFD	Free-Form Deformation
IPOPT	Interior Poin Optimizer
RANS	Reynolds Averaged Navier-Stokes
SST	Shear Stress Transport
XDSM	Extended Design Structure Matrix

## References

- [1] London, A. L., Klopfer, G., and Wolf, S., "Oblique Flow Headers for Heat Exchangers," *Journal of Engineering for Power*, Vol. 90, No. 3, 1968, pp. 271–284.
- [2] Wang, J., "Theory of flow distribution in manifolds," *Chemical Engineering Journal*, Vol. 168, No. 3, 2011, pp. 1331–1345. <https://doi.org/10.1016/j.cej.2011.02.050>.
- [3] Xia, G., Jiang, J., Wang, J., Zhai, Y., and Ma, D., "Effects of different geometric structures on fluid flow and heat transfer performance in microchannel heat sinks," *International Journal of Heat and Mass Transfer*, Vol. 80, 2015, pp. 439–447. <https://doi.org/https://doi.org/10.1016/j.ijheatmasstransfer.2014.08.095>.
- [4] Bajura, R. A., and Jones, J., E. H., "Flow Distribution Manifolds," *Journal of Fluids Engineering*, Vol. 98, No. 4, 1976, pp. 654–665. <https://doi.org/10.1115/1.3448441>, URL <https://doi.org/10.1115/1.3448441>.
- [5] Shen, P. I., "The Effect of Friction on Flow Distribution in Dividing and Combining Flow Manifolds," *Journal of Fluids Engineering*, Vol. 114, No. 1, 1992, pp. 121–123. <https://doi.org/10.1115/1.2909987>, URL <https://doi.org/10.1115/1.2909987>.
- [6] Yang, H., Wang, Y., Meng, X., Li, D., and Cai, X., "Guidelines for Design of Dividing Manifolds With Discharge Uniformly Distributed at Different Positions Along the Device Axis," *Journal of Fluids Engineering*, Vol. 142, No. 2, 2020. <https://doi.org/10.1115/1.4044984>.

- [7] Choi, S. H., Shin, S., and Cho, Y. I., "The effect of area ratio on the flow distribution in liquid cooling module manifolds for electronic packaging," *International Communication in Heat and Mass Transfer*, Vol. 20, No. 2, 1993, pp. 221–234. [https://doi.org/https://doi.org/10.1016/0735-1933\(93\)90050-6](https://doi.org/https://doi.org/10.1016/0735-1933(93)90050-6).
- [8] Jiang, Y., Alawee, W. H., Essa, F. A., Abdullah, A. s., Omara, Z. M., Ahmad, H., Ali, R., Wang, F., and Menni, Y., "Effect of area ratio and Reynolds number on the distribution of discharge in dividing manifold," *International Journal of Low-Carbon Technologies*, Vol. 17, 2022, pp. 1271–1279. <https://doi.org/10.1093/ijlct/ctac018>.
- [9] Choi, S. H., Shin, S., and Cho, Y. I., "The effect of the Reynolds number and width ratio of the flow distribution in manifolds of liquid cooling modules for electronic packaging," *International Communication in Heat and Mass Transfer*, Vol. 20, No. 5, 1993, pp. 607–617.
- [10] Tonomura, O., Tanaka, S., Noda, M., Kano, M., Hasebe, S., and Hashimoto, I., "CFD-based optimal design of manifold in plate-fin microdevices," *Chemical Engineering Journal*, Vol. 101, No. 1-3, 2004, pp. 397–402. <https://doi.org/10.1016/j.cej.2003.10.022>.
- [11] Kim, D., Yu, C.-H., Yoon, S. H., and Choi, J. S., "Effects of manifold geometries on flow distribution to parallel microchannels," *Journal of Mechanical Science and Technology*, Vol. 25, No. 12, 2012, pp. 3069–3074. <https://doi.org/10.1007/s12206-011-1220-3>.
- [12] Kim, S., Choi, E., and Cho, Y. I., "The effect of header shapes on the flow distribution in a manifold for electronic packaging applications," *International Communication in Heat and Mass Transfer*, Vol. 22, No. 3, 1995, pp. 329–341. [https://doi.org/https://doi.org/10.1016/0735-1933\(95\)00024-S](https://doi.org/https://doi.org/10.1016/0735-1933(95)00024-S).
- [13] Dharaiya, V. V., Radhakrishnan, A., and Kandlikar, S. G., "Evaluation of a Tapered Header Configuration to Reduce Flow Maldistribution in Minichannels and Microchannels," *ASME 2009 7th International Conference on Nanochannels, Microchannels and Minichannels*, 2009, pp. 771–777. <https://doi.org/10.1115/icnmm2009-82288>.
- [14] Tong, J. C. K., Sparrow, E. M., and Abraham, J. P., "Geometric strategies for attainment of identical outflows through all of the exit ports of a distribution manifold in a manifold system," *Applied Thermal Engineering*, Vol. 29, No. 17-18, 2009, pp. 3552–3560. <https://doi.org/10.1016/j.applthermaleng.2009.06.010>.
- [15] Kim, S., "A novel design method of the dividing header configuration using 3D numerical simulation for a heat exchanger with a parallel arrangement," *Applied Thermal Engineering*, Vol. 159, 2019. <https://doi.org/10.1016/j.applthermaleng.2019.113807>.
- [16] Samareh, J. A., "A Survey of shape parameterization techniques," *CEAS/AIAA/ICASE/NASA Langley International Forum on Aeroelasticity and Structural Dynamics 1999*, Vol. 1, 1999.
- [17] Samareh, J., "Aerodynamic shape optimization based on free-form deformation," *10th AIAA/ISSMO multidisciplinary analysis and optimization conference*, 2004, p. 4630.
- [18] Anand, N., Vitale, S., Pini, M., and Colonna, P., "Assessment of FFD and CAD-based shape parametrization methods for adjoint-based turbomachinery shape optimization," *Proceedings of Montreal*, Vol. 7, 2018, p. 9th.
- [19] Papalambros, P. Y., and Wilde, D. J., *Principles of optimal design: modeling and computation*, Cambridge university press, 2000.
- [20] Martins, J. R., Sturdza, P., and Alonso, J. J., "The complex-step derivative approximation," *ACM Transactions on Mathematical Software (TOMS)*, Vol. 29, No. 3, 2003, pp. 245–262.
- [21] Martins, J. R. R. A., and Ning, A., *Engineering Design Optimization*, Cambridge University Press, Cambridge, UK, 2022. <https://doi.org/10.1017/9781108980647>, URL <https://mdobook.github.io>.
- [22] Lambe, A. B., and Martins, J. R., "Extensions to the design structure matrix for the description of multidisciplinary design, analysis, and optimization processes," *Structural and Multidisciplinary Optimization*, Vol. 46, 2012, pp. 273–284.
- [23] Bajura, R. A., "A Model for Flow Distribution in Manifolds," *Journal of Engineering for Power*, Vol. 93, No. 1, 1971, pp. 7–12. <https://doi.org/10.1115/1.3445410>, URL <https://doi.org/10.1115/1.3445410>.
- [24] *Ansys ICEM CFD User's Manual*, Ansys, r2 ed., 2022. Available at [https://ansyshelp.ansys.com/account/secured?returnurl=/Views/Secured/corp/v222/en/icm\\_user/iuser\\_intro.html](https://ansyshelp.ansys.com/account/secured?returnurl=/Views/Secured/corp/v222/en/icm_user/iuser_intro.html).
- [25] Sederberg, T. W., and Parry, S. R., "Free-form deformation of solid geometric models," *Proceedings of the 13th annual conference on Computer graphics and interactive techniques*, 1986, pp. 151–160.

- [26] Economon, T. D., Palacios, F., Copeland, S. R., Lukaczyk, T. W., and Alonso, J. J., “SU2: An Open-Source Suite for Multiphysics Simulation and Design,” *AIAA Journal*, Vol. 54, No. 3, 2016, pp. 828–846. <https://doi.org/10.2514/1.J053813>, URL <https://doi.org/10.2514/1.J053813>.
- [27] Dwight, R. P., “Robust mesh deformation using the linear elasticity equations,” *Computational Fluid Dynamics 2006: Proceedings of the Fourth International Conference on Computational Fluid Dynamics, ICCFD, Ghent, Belgium, 10-14 July 2006*, Springer, 2009, pp. 401–406.
- [28] Economon, T. D., “Simulation and Adjoint-Based Design for Variable Density Incompressible Flows with Heat Transfer,” *AIAA Journal*, Vol. 58, No. 2, 2020, pp. 757–769. <https://doi.org/10.2514/1.J058222>, URL <https://doi.org/10.2514/1.J058222>.
- [29] Menter, F. R., “Two-equation eddy-viscosity turbulence models for engineering applications,” *AIAA Journal*, Vol. 32, No. 8, 1994, pp. 1598–1605. <https://doi.org/10.2514/3.12149>, URL <https://doi.org/10.2514/3.12149>.
- [30] Menter, F. R., Kuntz, M., Langtry, R., et al., “Ten years of industrial experience with the SST turbulence model,” *Turbulence, heat and mass transfer*, Vol. 4, No. 1, 2003, pp. 625–632.
- [31] Albring, T. A., Sagebaum, M., and Gauger, N. R., “Efficient aerodynamic design using the discrete adjoint method in SU2,” *17th AIAA/ISSMO multidisciplinary analysis and optimization conference*, 2016, p. 3518.
- [32] Economon, T. D., Alonso, J. J., Albring, T. A., and Gauger, N. R., “Adjoint formulation investigations of benchmark aerodynamic design cases in SU2,” *35th AIAA Applied Aerodynamics Conference*, 2017, p. 4363.
- [33] Wächter, A., and Biegler, L. T., “On the implementation of an interior-point filter line-search algorithm for large-scale nonlinear programming,” *Mathematical programming*, Vol. 106, 2006, pp. 25–57.

## Appendix A: London Shape Coordinates

**Table 7** Coordinates of the initial London shape.

x-coordinate [mm]	16.5	18.375	20.25	22.125	24	25.875	27.75	29.625	31.5
diameter [mm]	10.5	10.17	9.82	9.44	9.05	8.64	8.24	7.83	7.43
x-coordinate [mm]	33.375	35.25	37.125	39	40.875	42.75	44.625	46.5	48.375
diameter [mm]	7.04	6.66	6.3	5.95	5.62	5.3	5.01	4.73	4.46
x-coordinate [mm]	50.25	52.125	54	55.875	57.75	59.625	61.5		
diameter [mm]	4.21	3.98	3.76	3.55	3.36	3.17	3.0		

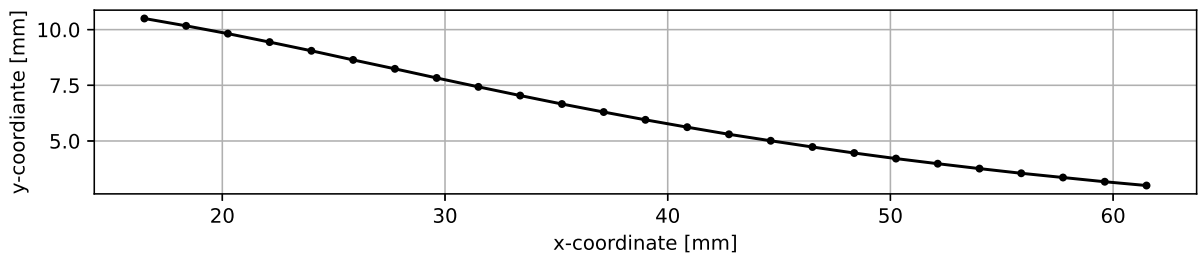


**Fig. 34** Plotted coordinates of the initial London shape.

**Table 8** Coordinates of the London shape for the combining manifold.

x-coordinate [mm]	16.5	18.375	20.25	22.125	24	25.875	27.75	29.625	31.5
diameter [mm]	3.0	3.17	3.36	3.55	3.76	3.98	4.21	4.46	4.73
x-coordinate [mm]	33.375	35.25	37.125	39	40.875	42.75	44.625	46.5	48.375
diameter [mm]	5.01	5.3	5.62	5.95	6.3	6.66	7.04	7.43	7.83
x-coordinate [mm]	50.25	52.125	54	55.875	57.75	59.625	61.5		
diameter [mm]	8.24	8.64	9.05	9.44	9.82	10.17	10.5		

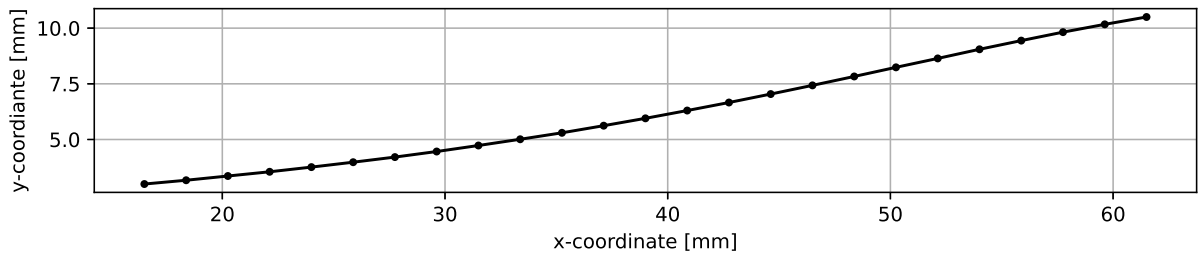


**Fig. 35** Plotted coordinates of the London shape for the combining manifold.

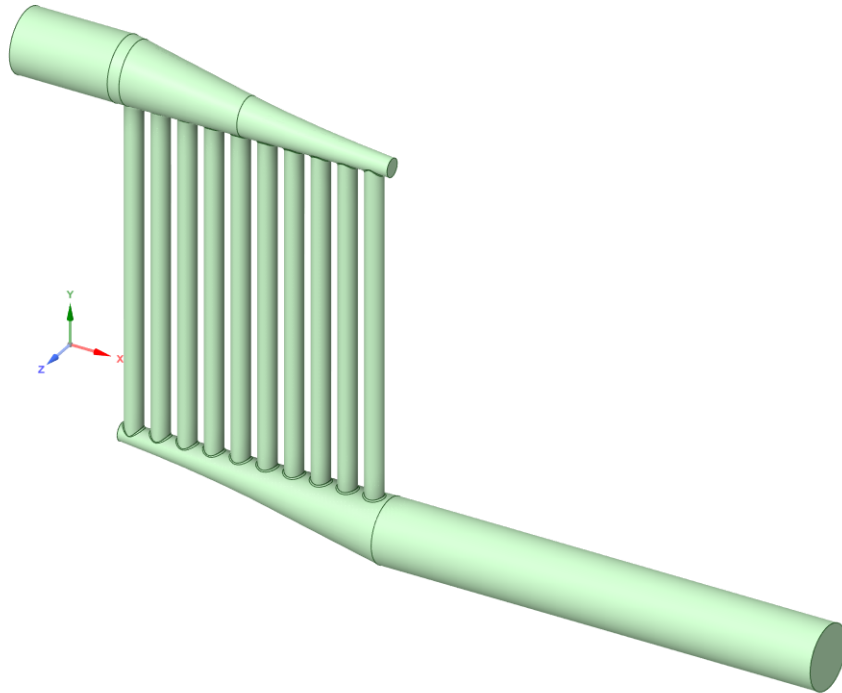


**Fig. 36** 3D model with both manifolds shaped according to London's design method.

**Table 9** Coordinates of the London shape for an inlet velocity of 1.25 m/s.

x-coordinate [mm]	16.5	18.375	20.25	22.125	24	25.875	27.75	29.625	31.5
diameter [mm]	8.5	8.26	8.0	7.72	7.43	7.14	6.84	6.54	6.25
x-coordinate [mm]	33.375	35.25	37.125	39	40.875	42.75	44.625	46.5	48.375
diameter [mm]	5.96	5.68	5.42	5.16	4.92	4.69	4.47	4.27	4.07
x-coordinate [mm]	50.25	52.125	54	55.875	57.75	59.625	61.5		
diameter [mm]	3.89	3.72	3.56	3.4	3.26	3.13	3.0		

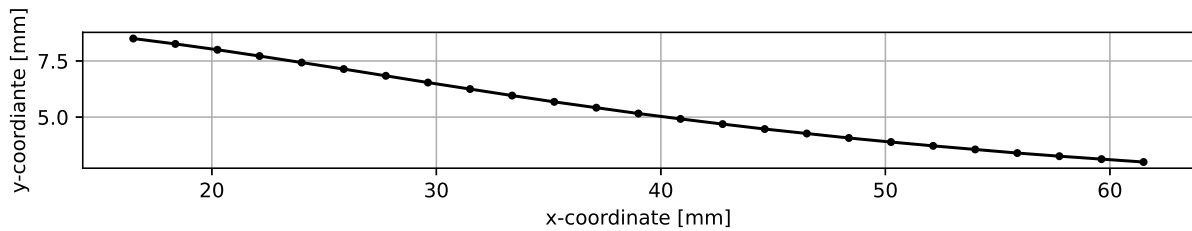


**Fig. 37** Plotted coordinates of the London shape for an inlet velocity of 1.25 m/s.

## Appendix B: Convergence plots

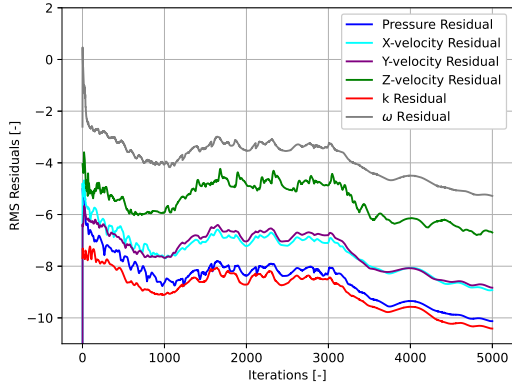


**Fig. 38** Convergence plots of CFD simulation of Yang's geometry as discussed in subsection IV.A.

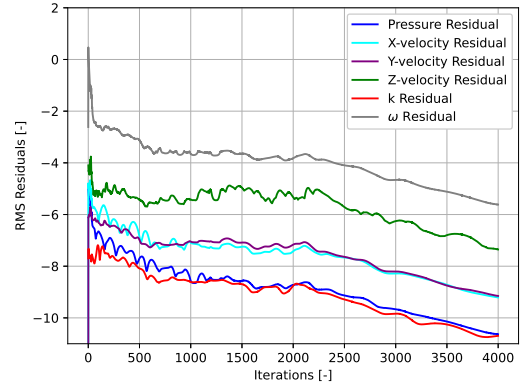


**Fig. 39** Convergence plots of CFD simulation of London's geometry as discussed in subsection IV.A.

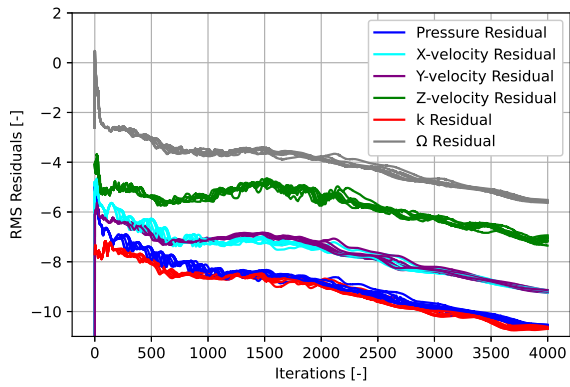


**Fig. 40** Convergence plots of CFD simulation of Radial-based optimization as discussed in subsection IV.B.

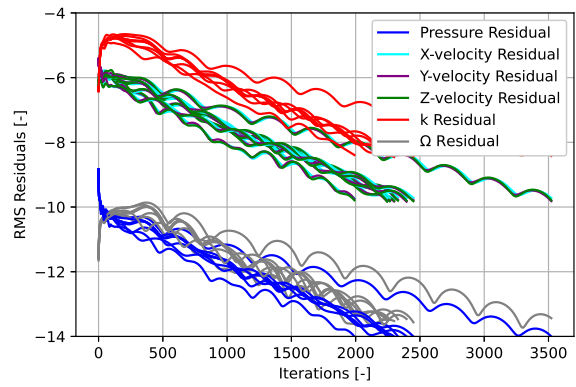


**Fig. 41** Convergence plots of adjoint simulation of Radial-based optimization as discussed in subsection IV.B.

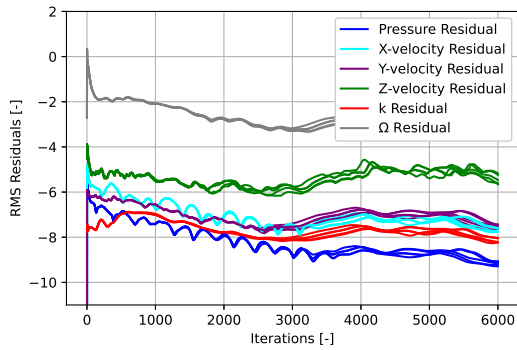


**Fig. 42** Convergence plots of CFD simulation of Cartesian-based optimization as discussed in subsection IV.B.

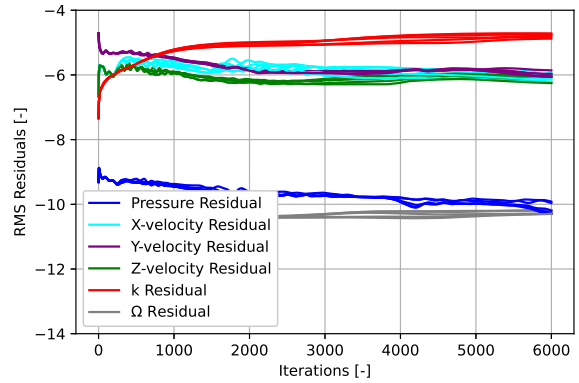


**Fig. 43** Convergence plots of adjoint simulation of Cartesian-based optimization as discussed in subsection IV.B.

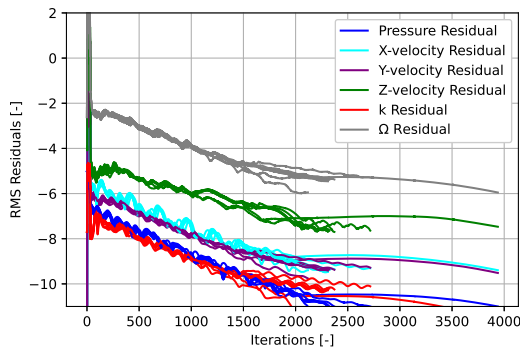


**Fig. 44** Convergence plots of CFD simulation of dual-manifold optimization as discussed in subsection IV.B.

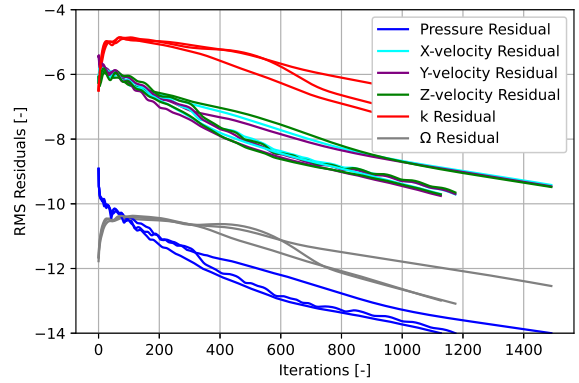


**Fig. 45** Convergence plots of adjoint simulation of dual-manifold optimization as discussed in subsection IV.B.

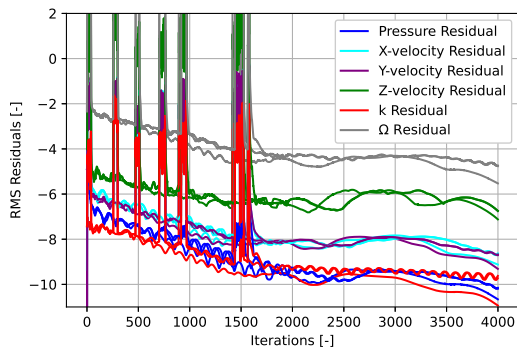


**Fig. 46** Convergence plots of CFD simulations in the optimization with different inlet velocity as discussed in subsection IV.D.

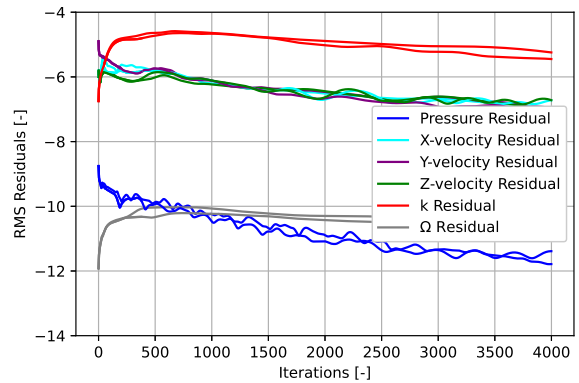


**Fig. 47** Convergence plots of adjoint simulations in the optimization with different inlet velocity as discussed in subsection IV.D.

### Appendix C: Location of slices used in the result analysis.

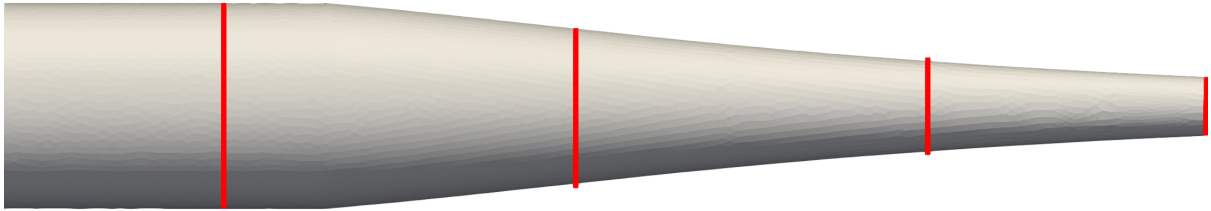
**Table 10 X-coordinates of the slices used in the results analysis of the dividing manifold.**

Slice Number	1	2	3	4	5	6	7	8
x-location slice [mm]	0.01	2.25	6.75	11.25	15.75	20.25	24.75	29.25
Slice Number	9	10	11	12	13	14	15	16
x-location slice [mm]	33.75	38.25	42.75	47.25	51.75	56.25	60.75	61.49

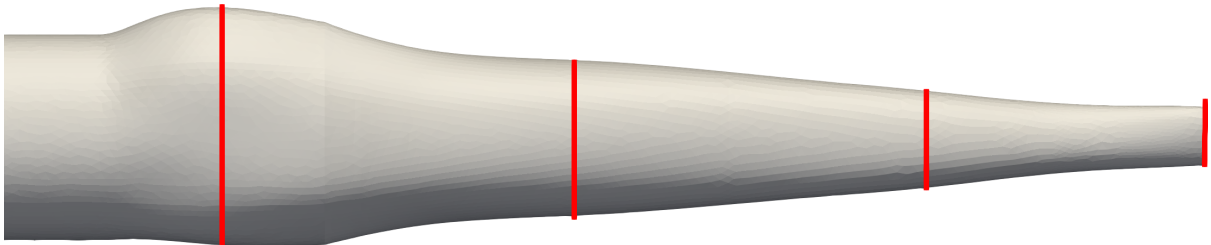
**Table 11 X-coordinates of the slices used in the results analysis of the combining manifold.**

Slice Number	1	2	3	4	5	6	7	8
x-location slice [mm]	16.1	20.25	24.75	29.25	33.75	38.25	42.75	47.25
Slice Number	9	10	11	12	13	14	15	16
x-location slice [mm]	51.75	56.25	60.75	65.25	69.75	74.25	78.75	83.25
Slice Number	17	18	19	20	21	22	23	24
x-location slice [mm]	87.75	92.25	96.75	101.25	105.75	110.25	114.75	119.25
Slice Number	25	26	27	28				
x-location slice [mm]	123.75	128.25	132.75	134.90				

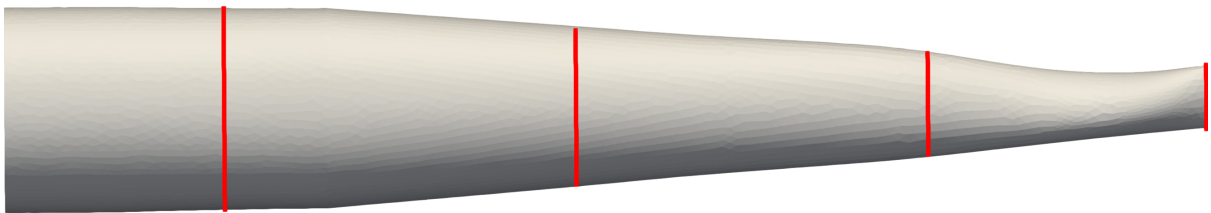
## Appendix D: Resulting 3D Models of the different optimization procedures



(a) Top view of London's design for the dividing manifold.

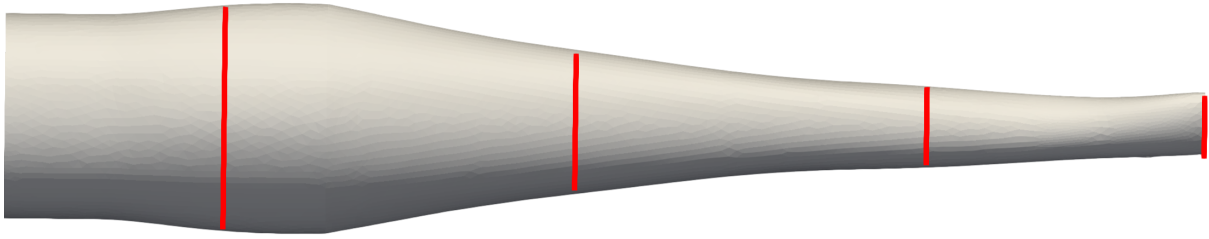


(b) Top view of the dividing manifold obtained through radial-based optimization.

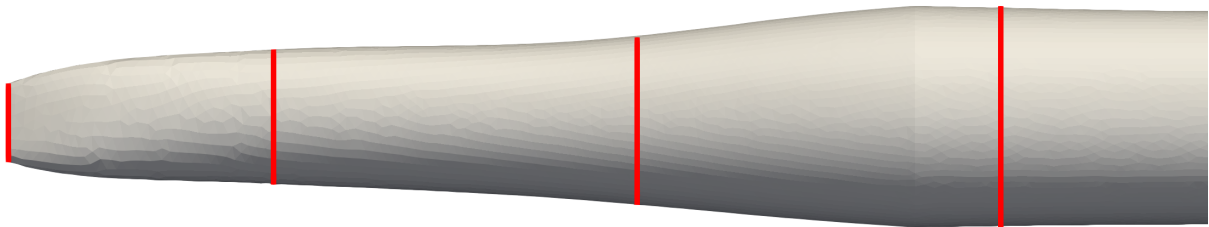


(c) Top view of the dividing manifold obtained through freely-based optimization.

**Fig. 48** Top view of several dividing manifolds, the red stripes mark the locations of the slices used in Figure 15.



(a) Top view of the dividing manifold obtained through optimization.



(b) Top view of the combining manifold obtained through optimization.

**Fig. 49** Top view of dividing and combining manifolds for the double-optimized design procedure, the red stripes mark the locations of the slices used in Figure 21 and Figure 22.

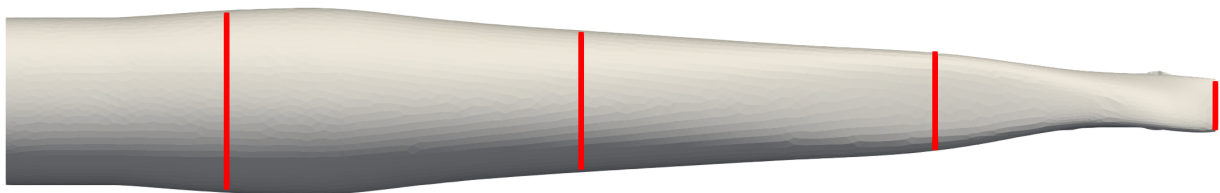


**Fig. 50** Top view of the optimized dividing manifold for  $V_{init}=1.25$  m/s.

### Appendix E: Optimization runs with Yang's design as the initial design.

Initially, the research aimed to start the optimization runs from Yang's design. However, from several attempts, it was concluded that Yang's design was an unsuitable starting point for the optimizer currently selected. In this section these attempts will be discussed, and why it is believed that these attempts did not work. It must be noted that the discussed results below are from the 'best' attempts and more experiments have been performed to come to these conclusions. Moreover, it should be noted that due to limited resources, all experiments were limited to a 24-hour run time. Hence, the obtained results are not actual optimal designs.

The first attempt that was made to optimize Yang's manifold design was based on a rectangular FFD box with freely moving FFD nodes. From Figure 51, it can be seen that this attempt led to unexpected non-symmetrical shapes. The obtained shape resulted in a mall distribution factor of 0.071 from an initial mall distribution factor of 0.085, moreover, it was found that both the flow and adjoint solver converged for each iteration. Although the non-symmetrical shape of the manifold is not a reason to discard the initial design of Yang, from the obtained sensitivities it was found that the adjoint solver found very small sensitivities towards the end of the manifold. This means that the deformation near the end of the manifold will be of limited amount. However, from the literature and the obtained results discussed in the paper, it is found that an oblique shape is beneficial to the mall distribution factor. Moreover, the paper aims to find possible improvements to the current design method of London. As the obtained results of the freely-based optimization from Yang's design did not indicate any movement towards such oblique shapes, it was determined that for this method Yang's manifold could not be used as an initial design.

However, it is recommended to let the optimization run with more run time when more resources are available. As both the flow and adjoint solver converged and the objective decreased with the first few design iterations. Although the obtained designs might run into manufacturing limitations, valuable lessons could be learned with respect to the flow physics within manifold systems.



**Fig. 51** Top view of deformed Yang manifold with freely moving nodes, with the inlet on the left side of the figure.

The second attempt to optimize Yang's manifold design was based on a rectangular FFD box with radial moving nodes. From Figure 52, it can be seen that the obtained manifold shows similar features compared to the freely moving nodes. However, the extrusions of the manifold and the back of the manifold are made much larger than before. This result is mainly due to larger design space for the radial-based optimization. The resulting shape had a mall distribution factor of 0.043, with both flow and adjoint solver converging.

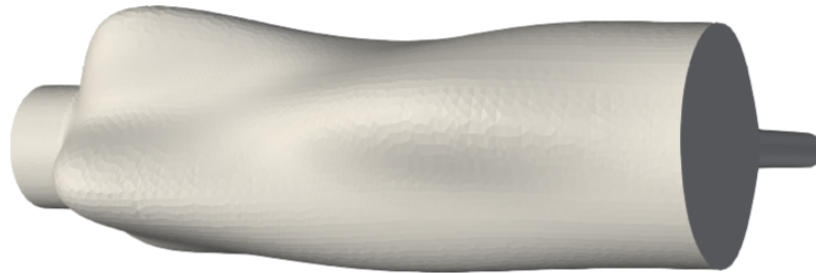


**Fig. 52** Top view of deformed Yang manifold with radial moving nodes, with the inlet on the left side of the figure.

The argumentation for why the radial-based method for Yang's manifold did not work, is largely the same as for the freely-based manifold. Moreover, from Figure 53 it can be seen that the enlargement of the manifold mainly causes a large recirculation zone. These recirculation zones allow for a better maldistribution factor with a lower pressure loss in the system. However, enlarging the design is often not desirable due to space restrictions and limitations.

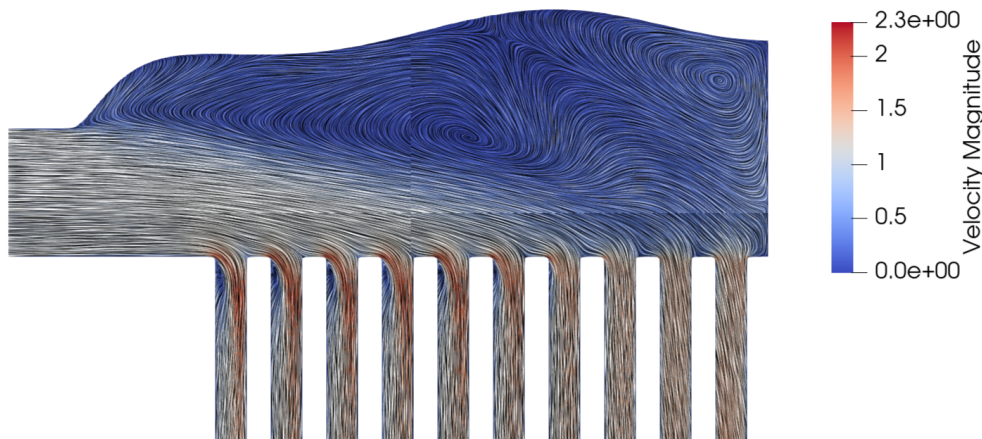


**Fig. 53** Caption

The last attempt to optimize Yang's manifold design used a circular FFD box, as in Figure 55. The main problem with the circular FFD boxes is the strict orientation of the geometry with respect to the geometry. As can be seen in Figure 54, the circular FFD box has a gap between the two faces of the FFD box. This gap initially caused a bad mesh deformation as shown in Figure 56. To avoid this behaviour from happening the mesh was rotated such that the gap would coincide with the lateral channels, as these already were excluded from the deformation. However, this resulted in negligible deformations. Therefore, in line with earlier discussion, this method also was neglected.

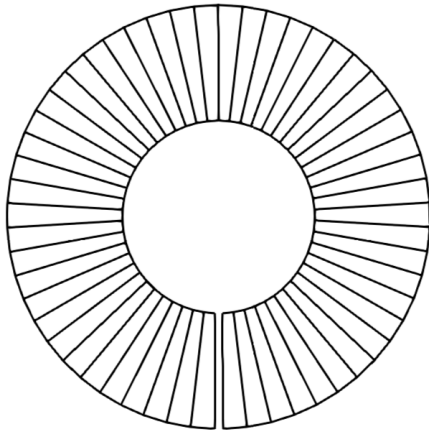


Fig. 54 Front view of the circular FFD box.

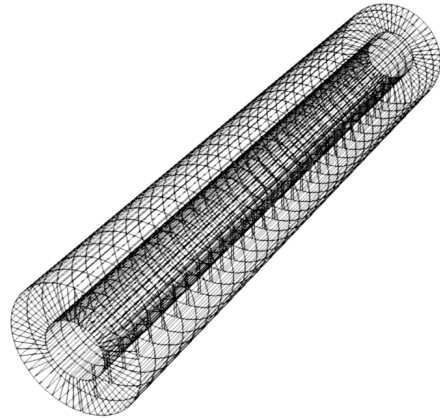


Fig. 55 Isometric view of the circular FFD box.

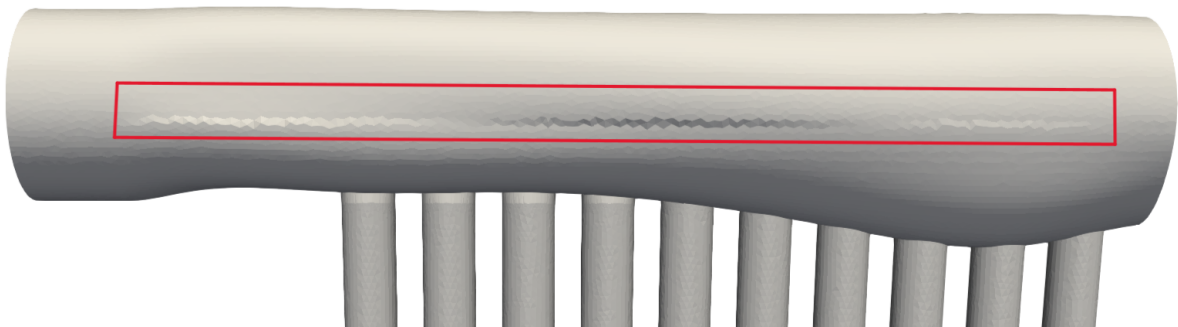


Fig. 56 Bad mesh quality after deformation, marked by the red box.

### Appendix F: Example of a configuration file used in the optimization procedure.

The configuration file shown below has been used in the radial-based optimization. It must be noted that for some settings either `%_DIRECT_` or `%_ADJOINT_` has been used. These settings are specific to the CFD and Adjoint solver respectively. The used FADO file is set up such that these settings are automatically changed, therefore it is possible to use one configuration file for both solvers. Moreover, it should be noted that the `DV_KIND` and `DV_PARAM`, on line 331 and 338 respectively, are not completed as this would require two vectors of 5040 settings.

```

1 % ----- DIRECT, ADJOINT, AND LINEARIZED PROBLEM DEFINITION -----%
2 %
3 % Solver type (RANS, INC_RANS)
4 SOLVER= INC_RANS
5 %
6 % Specify turbulence model (NONE, SA, SST)
7 KIND_TURB_MODEL= SST
8 %

```

```

9 % Specify versions/corrections of the SST model (V2003m, V1994m, VORTICITY, KATO_LAUNDER, UQ,
  SUSTAINING)
10 SST_OPTIONS= V2003m
11 %
12 % Mathematical problem (DIRECT, CONTINUOUS_ADJOINT, DISCRETE_ADJOINT)
13 % Defaults to DISCRETE_ADJOINT for the SU2_*_AD codes, and to DIRECT otherwise.
14 %MATH_PROBLEM= DIRECT
15 %
16 % Restart solution (NO, YES)
17 RESTART_SOL= NO
18 %
19 % ----- CUSTOM OUTPUTS AND OBJECTIVE FUNSTION -----%
20 %
21 CUSTOM_OUTPUTS = 'avgMfC : Function{(SURFACE_MASSFLOW[1] + SURFACE_MASSFLOW[2] + \
22 SURFACE_MASSFLOW[3] + SURFACE_MASSFLOW[4] +SURFACE_MASSFLOW[5] + \
23 SURFACE_MASSFLOW[6] + SURFACE_MASSFLOW[7] + SURFACE_MASSFLOW[8] + \
24 SURFACE_MASSFLOW[9] + SURFACE_MASSFLOW[10]) / 10}'
25 %
26 OBJECTIVE_FUNCTION= CUSTOM_OBFUNC
27 %
28 CUSTOM_OBFUNC = 'sqrt((pow((SURFACE_MASSFLOW[1]-avgMfC)/avgMfC, 2) + \
29 pow((SURFACE_MASSFLOW[2]-avgMfC)/avgMfC, 2) + \
30 pow((SURFACE_MASSFLOW[3]-avgMfC)/avgMfC, 2) + \
31 pow((SURFACE_MASSFLOW[4]-avgMfC)/avgMfC, 2) + \
32 pow((SURFACE_MASSFLOW[5]-avgMfC)/avgMfC, 2) + \
33 pow((SURFACE_MASSFLOW[6]-avgMfC)/avgMfC, 2) + \
34 pow((SURFACE_MASSFLOW[7]-avgMfC)/avgMfC, 2) + \
35 pow((SURFACE_MASSFLOW[8]-avgMfC)/avgMfC, 2) + \
36 pow((SURFACE_MASSFLOW[9]-avgMfC)/avgMfC, 2) + \
37 pow((SURFACE_MASSFLOW[10]-avgMfC)/avgMfC, 2)) / 9)'
38 %
39 GRAD_OBFUNC_FILENAME= of_grad.dat
40 %
41 % ----- SOLVER CONTROL -----%
42 %
43 % Number of iterations for single-zone problems
44 %__DIRECT__ITER= 4000
45 %__ADJOINT__ITER = 4000
46 %
47 % Convergence field
48 %__DIRECT__CONV_FIELD= RMS_PRESSURE
49 %__ADJOITN__CONV_FIELD= RMS_ADJ_PRESSURE
50 %
51 % Min value of the residual (log10 of the residual)
52 %__DIRECT__CONV_RESIDUAL_MINVAL= -11
53 %__ADJOINT__CONV_RESIDUAL_MINVAL = -14
54 %
55 % Start convergence criteria at iteration number
56 CONV_STARTITER= 10
57 %
58 % Number of elements to apply the criteria
59 CONV_CAUCHY_ELEMS= 100
60 %
61 % Epsilon to control the series convergence
62 CONV_CAUCHY_EPS= 1E-10
63 %
64 % ----- INCOMPRESSIBLE FLOW CONDITION DEFINITION -----%
65 %
66 % Density model within the incompressible flow solver.
67 % Options are CONSTANT (default), BOUSSINESQ, or VARIABLE. If VARIABLE,
68 % an appropriate fluid model must be selected.
69 INC_DENSITY_MODEL= CONSTANT
70 %
71 % Solve the energy equation in the incompressible flow solver
72 INC_ENERGY_EQUATION = NO
73 %
74 % Initial density for incompressible flows
75 % (1.2886 kg/m^3 by default (air), 998.2 Kg/m^3 (water))

```

```

76 INC_DENSITY_INIT= 995.74
77 %
78 % Initial velocity for incompressible flows (1.0,0,0 m/s by default)
79 INC_VELOCITY_INIT= ( 1.0, 0.0, 0.0 )
80 %
81 % Initial temperature for incompressible flows that include the
82 % energy equation (288.15 K by default). Value is ignored if
83 % INC_ENERGY_EQUATION is false.
84 INC_TEMPERATURE_INIT= 300.45
85 %
86 % Non-dimensionalization scheme for incompressible flows. Options are
87 % INITIAL_VALUES (default), REFERENCE_VALUES, or DIMENSIONAL.
88 % INC_*_REF values are ignored unless REFERENCE_VALUES is chosen.
89 INC_NONDIM= DIMENSIONAL
90 %
91 % Reference density for incompressible flows (1.0 kg/m^3 by default)
92 INC_DENSITY_REF= 995.74
93 %
94 % Reference velocity for incompressible flows (1.0 m/s by default)
95 INC_VELOCITY_REF= 1.0
96 %
97 % Reference temperature for incompressible flows that include the
98 % energy equation (1.0 K by default)
99 INC_TEMPERATURE_REF = 300.45
100 %
101 % List of inlet types for incompressible flows. List length must
102 % match number of inlet markers. Options: VELOCITY_INLET, PRESSURE_INLET.
103 INC_INLET_TYPE= VELOCITY_INLET
104 %
105 % List of outlet types for incompressible flows. List length must
106 % match number of outlet markers. Options: PRESSURE_OUTLET, MASS_FLOW_OUTLET
107 INC_OUTLET_TYPE= PRESSURE_OUTLET
108 % ----- VISCOSITY MODEL -----%
109 %
110 % Viscosity model (SUTHERLAND, CONSTANT_VISCOSITY, POLYNOMIAL_VISCOSITY).
111 VISCOSITY_MODEL= CONSTANT_VISCOSITY
112 %
113 % Molecular Viscosity that would be constant (1.716E-5 by default)
114 MU_CONSTANT= 8E-4
115 %
116 % ----- THERMAL CONDUCTIVITY MODEL -----%
117 %
118 % Laminar Conductivity model (CONSTANT_CONDUCTIVITY, CONSTANT_PRANDTL,
119 % POLYNOMIAL_CONDUCTIVITY).
120 CONDUCTIVITY_MODEL= CONSTANT_CONDUCTIVITY
121 %
122 % Molecular Thermal Conductivity that would be constant (0.0257 by default)
123 THERMAL_CONDUCTIVITY_CONSTANT= 0.614
124 %
125 % Definition of the turbulent thermal conductivity model for RANS
126 % (CONSTANT_PRANDTL_TURB by default, NONE).
127 TURBULENT_CONDUCTIVITY_MODEL= CONSTANT_PRANDTL_TURB
128 %
129 % Turbulent Prandtl number (0.9 (air) by default)
130 PRANDTL_TURB= 0.90
131 %
132 % ----- BOUNDARY CONDITION DEFINITION -----%
133 %
134 % Navier-Stokes (no-slip), constant heat flux wall marker(s) (NONE = no marker)
135 % Format: ( marker name, constant heat flux (J/m^2), ... )
136 MARKER_HEATFLUX= ( HEXWALL, 0.0, INLETMAN, 0.0, OUTLETMAN, 0.0, INLETCH, 0.0, OUTLETCH, 0.0)
137 %
138 % Inlet boundary marker(s) with the following formats (NONE = no marker)
139 % Inc. Velocity: (inlet marker, temperature, velocity magnitude, flow_direction_x,
140 % flow_direction_y, flow_direction_z, ... ) where flow_direction is
141 % a unit vector.
142 % Inc. Pressure: (inlet marker, temperature, total pressure, flow_direction_x,
143 % flow_direction_y, flow_direction_z, ... ) where flow_direction is

```

```

144 %           a unit vector.
145 MARKER_INLET= ( INLET, 300.45, 1.0, 1, 0, 0 )
146 MARKER_INTERNAL = (CH1, CH2, CH3, CH4, CH5, CH6, CH7, CH8, CH9, CH10)
147 %
148 % Outlet boundary marker(s) (NONE = no marker)
149 MARKER_OUTLET= ( OUTLET, 0.0)
150 %
151 FREESTREAM_TURBULENCEINTENSITY= 0.05
152 % ----- SURFACES IDENTIFICATION -----%
153 %
154 % Marker(s) of the surface in the surface flow solution file
155 MARKER_PLOTTING = (INLET, CH1, CH2, CH3, CH4, CH5, CH6, CH7, CH8, CH9, CH10)
156 %
157 % Marker(s) of the surface where the non-dimensional coefficients are evaluated.
158 MARKER_MONITORING = (INLET, CH1, CH2, CH3, CH4, CH5, CH6, CH7, CH8, CH9, CH10 )
159 %
160 MARKER_ANALYZE = (INLET, CH1, CH2, CH3, CH4, CH5, CH6, CH7, CH8, CH9, CH10 )
161 %
162 % ----- COMMON PARAMETERS DEFINING THE NUMERICAL METHOD -----%
163 %
164 % Numerical method for spatial gradients (GREEN_GAUSS, WEIGHTED_LEAST_SQUARES)
165 NUM_METHOD_GRAD= WEIGHTED_LEAST_SQUARES
166 %
167 % CFL number (initial value for the adaptive CFL number)
168 %__DIRECT__CFL_NUMBER= 1
169 %__ADJOINT__CFL_NUMBER = 100
170 %
171 % Adaptive CFL number (NO, YES)
172 %__DIRECT__CFL_ADAPT= YES
173 %__ADJOINT__CFL_ADAPT= NO
174 % Parameters of the adaptive CFL number (factor-down, factor-up, CFL min value,
175 %                                     CFL max value, acceptable linear solver convergence)
176 % Local CFL increases by factor-up until max if the solution rate of change is not limited,
177 % and acceptable linear convergence is achieved. It is reduced if rate is limited, or if there
178 % is not enough linear convergence, or if the nonlinear residuals are stagnant and oscillatory.
179 % It is reset back to min when linear solvers diverge, or if nonlinear residuals increase too
180 % much.
180 CFL_ADAPT_PARAM= ( 0.9, 1.1, 1.0, 1000.0, 1E-6 )
181 %
182 % ----- LINEAR SOLVER DEFINITION -----%
183 %
184 % Linear solver or smoother for implicit formulations:
185 % BCGSTAB, FGMRES, RESTARTED_FGMRES, CONJUGATE_GRADIENT (self-adjoint problems only), SMOOTHER.
186 LINEAR_SOLVER= FGMRES
187 %
188 % Preconditioner of the Krylov linear solver or type of smoother (ILU, LU_SGS, LINELET, JACOBI)
189 LINEAR_SOLVER_PREC= LU_SGS
190 %
191 % Minimum error of the linear solver for implicit formulations
192 LINEAR_SOLVER_ERROR= 1E-8
193 %
194 % Max number of iterations of the linear solver for the implicit formulation
195 LINEAR_SOLVER_ITER= 20
196 %
197 % ----- FLOW NUMERICAL METHOD DEFINITION -----%
198 %
199 % Convective numerical method (JST, JST_KE, JST_MAT, LAX-FRIEDRICH, CUSP, ROE, AUSM,
200 %                               AUSMPLUSUP, AUSMPLUSUP2, AUSMPLUSM, HLLC, TURKEL_PREC,
201 %                               SW, MSW, FDS, SLAU, SLAU2, L2ROE, LMROE)
202 CONV_NUM_METHOD_FLOW= FDS
203 %
204 % Time discretization (RUNGE-KUTTA_EXPLICIT, EULER_IMPLICIT, EULER_EXPLICIT)
205 TIME_DISCRE_FLOW= EULER_IMPLICIT
206 %
207 % ----- SLOPE LIMITER AND DISSIPATION SENSOR DEFINITION -----%
208 %
209 % Monotonic Upwind Scheme for Conservation Laws (TVL) in the flow equations.
210 %           Required for 2nd order upwind schemes (NO, YES)

```

```

211 MUSCL_FLOW= YES
212 %
213 % Slope limiter (NONE, VENKATAKRISHNAN, VENKATAKRISHNAN_WANG,
214 %             BARTH_JESPERSEN, VAN_ALBADA_EDGE)
215 SLOPE_LIMITER_FLOW= NONE
216 VENKAT_LIMITER_COEFF= 0.5
217 %
218 % Monotonic Upwind Scheme for Conservation Laws (TVD) in the turbulence equations.
219 %             Required for 2nd order upwind schemes (NO, YES)
220 MUSCL_TURB= NO
221 %
222 % Slope limiter (NONE, VENKATAKRISHNAN, VENKATAKRISHNAN_WANG,
223 %             BARTH_JESPERSEN, VAN_ALBADA_EDGE)
224 SLOPE_LIMITER_TURB= NONE
225 %
226 % Freeze the value of the limiter after a number of iterations
227 LIMITER_ITER= 999999
228 %
229 % ----- TURBULENT NUMERICAL METHOD DEFINITION -----%
230 %
231 % Convective numerical method (SCALAR_UPWIND, BOUNDED_SCALAR)
232 CONV_NUM_METHOD_TURB= SCALAR_UPWIND
233 %
234 % Reduction factor of the CFL coefficient in the turbulence problem
235 CFL_REDUCTION_TURB= 0.1
236 %
237 % Time discretization (EULER_IMPLICIT, EULER_EXPLICIT)
238 TIME_DISCRE_TURB= EULER_IMPLICIT
239 %
240 % ----- ADJOINT-FLOW NUMERICAL METHOD DEFINITION -----%
241 %
242 % Convective numerical method (JST, LAX-FRIEDRICH, ROE)
243 CONV_NUM_METHOD_ADJFLOW= JST
244 %
245 % Time discretization (RUNGE-KUTTA_EXPLICIT, EULER_IMPLICIT)
246 TIME_DISCRE_ADJFLOW= EULER_IMPLICIT
247 %
248 % Relaxation coefficient (also for discrete adjoint problems)
249 RELAXATION_FACTOR_ADJOINT= 1.0
250 %
251 % Reduction factor of the CFL coefficient in the adjoint problem
252 CFL_REDUCTION_ADJFLOW= 0.8
253 %
254 % Limit value for the adjoint variable
255 LIMIT_ADJFLOW= 1E6
256 %
257 % Use multigrid in the adjoint problem (NO, YES)
258 MG_ADJFLOW= NO
259 %
260 % ----- ADJOINT-TURBULENT NUMERICAL METHOD DEFINITION -----%
261 %
262 % Convective numerical method (SCALAR_UPWIND)
263 CONV_NUM_METHOD_ADJTURB= SCALAR_UPWIND
264 %
265 % Time discretization (EULER_IMPLICIT)
266 TIME_DISCRE_ADJTURB= EULER_IMPLICIT
267 %
268 % Reduction factor of the CFL coefficient in the adjoint turbulent problem
269 CFL_REDUCTION_ADJTURB= 0.01
270 %
271 % ----- FREE-FORM DEFORMATION PARAMETERS -----%
272 %
273 % Parameters for prevention of self-intersections within FFD box
274 FFD_INTPREV = YES
275 %
276 % Parameters for prevention of nonconvex elements in mesh after deformation
277 CONVEXITY_CHECK = YES
278 %

```

```

279 % Tolerance of the Free-Form Deformation point inversion
280 FFD_TOLERANCE= 1E-10
281 %
282 % Maximum number of iterations in the Free-Form Deformation point inversion
283 FFD_ITERATIONS= 500
284 %
285 % FFD box definition: 3D case (FFD_BoxTag, X1, Y1, Z1, X2, Y2, Z2, X3, Y3, Z3, X4, Y4, Z4,
286 %                               X5, Y5, Z5, X6, Y6, Z6, X7, Y7, Z7, X8, Y8, Z8)
287 %                               2D case (FFD_BoxTag, X1, Y1, 0.0, X2, Y2, 0.0, X3, Y3, 0.0, X4, Y4, 0.0,
288 %                               0.0, 0.0, 0.0, 0.0, 0.0, 0.0, 0.0, 0.0, 0.0, 0.0, 0.0, 0.0)
289 FFD_DEFINITION= ( CBOX, \
290 0.0050, 0.05225, 0.00725, \
291 0.0620, 0.05225, 0.00725, \
292 0.0620, 0.06275, 0.00725, \
293 0.0050, 0.06275, 0.00725, \
294 0.0050, 0.05225, 0.01775, \
295 0.0620, 0.05225, 0.01775, \
296 0.0620, 0.06275, 0.01775, \
297 0.0050, 0.06275, 0.01775)
298 %
299 % FFD box degree: 3D case (i_degree, j_degree, k_degree)
300 %                               2D case (i_degree, j_degree, 0)
301 FFD_DEGREE= (29, 14, 14)
302 FFD_CONTINUITY = 2ND_DERIVATIVE
303 %
304 % ----- DESIGN VARIABLE PARAMETERS -----%
305 %
306 % Kind of deformation (NO_DEFORMATION, SCALE_GRID, TRANSLATE_GRID, ROTATE_GRID,
307 %                               FFD_SETTING, FFD_NACELLE,
308 %                               FFD_CONTROL_POINT, FFD_CAMBER, FFD_THICKNESS, FFD_TWIST
309 %                               FFD_CONTROL_POINT_2D, FFD_CAMBER_2D, FFD_THICKNESS_2D,
310 %                               FFD_TWIST_2D, HICKS_HENNE, SURFACE_BUMP, SURFACE_FILE)
311 DV_KIND= FFD_CONTROL_POINT, ..., FFD_CONTROL_POINT
312 %
313 % Marker of the surface in which we are going apply the shape deformation
314 DV_MARKER= ( INLETMAN )
315 %
316 % Parameters of the shape deformation
317 % - FFD_CONTROL_POINT ( FFD_BoxTag, i_Ind, j_Ind, k_Ind, x_Disp, y_Disp, z_Disp )
318 DV_PARAM=(CBOX, 2, 3, 0, 0.0, 0.428571, -1.0 );...;(CBOX, 29, 14, 14, 0.0, 2.0, 1.0 )
319 %
320 DV_VALUE = __FFD_PTS__
321 %
322 % ----- GRID DEFORMATION PARAMETERS -----%
323 %
324 % Linear solver or smoother for implicit formulations (FGMRES, RESTARTED_FGMRES, BCGSTAB)
325 DEFORM_LINEAR_SOLVER= CONJUGATE_GRADIENT
326 %
327 % Preconditioner of the Krylov linear solver (ILU, LU_SGS, JACOBI)
328 DEFORM_LINEAR_SOLVER_PREC= ILU
329 %
330 % Number of smoothing iterations for mesh deformation
331 DEFORM_LINEAR_SOLVER_ITER= 300
332 %
333 % Number of nonlinear deformation iterations (surface deformation increments)
334 DEFORM_NONLINEAR_ITER= 1
335 %
336 % Minimum residual criteria for the linear solver convergence of grid deformation
337 DEFORM_LINEAR_SOLVER_ERROR= 1E-14
338 %
339 % Print the residuals during mesh deformation to the console (YES, NO)
340 DEFORM_CONSOLE_OUTPUT= YES
341 %
342 % Type of element stiffness imposed for FEA mesh deformation (INVERSE_VOLUME,
343 %                               WALL_DISTANCE, CONSTANT_STIFFNESS)
344 DEFORM_STIFFNESS_TYPE= WALL_DISTANCE
345 %
346 % ----- INPUT/OUTPUT FILE INFORMATION -----%

```

```

347 %
348 %__DIRECT__VOLUME_OUTPUT= (COORDINATES, SOLUTION, PRIMITIVE, RESIDUAL)
349 %__ADJOINT__VOLUME_OUTPUT= (COORDINATES, SOLUTION, RESIDUAL)
350 %__DIRECT__SCREEN_OUTPUT= (INNER_ITER, RMS_PRESSURE, RMS_VELOCITY-X, RMS_VELOCITY-Y,
    RMS DISSIPATION)
351 %__ADJOINT__SCREEN_OUTPUT= (INNER_ITER, RMS_ADJ_PRESSURE, RMS_ADJ DISSIPATION)
352 %__DIRECT__HISTORY_OUTPUT= (ITER, RMS_RES, SURFACE_MASSFLOW, COMBO, LINSOL, AVG_CFL)
353 %__ADJOINT__HISTORY_OUTPUT= (ITER, RMS_RES, LINSOL)
354
355 % Mesh input file
356 MESH_FILENAME= London_def.su2
357 MESH_OUT_FILENAME= London_def.su2
358 %
359 % Mesh input file format (SU2, CGNS)
360 MESH_FORMAT= SU2
361 %
362 % Restart flow input file
363 SOLUTION_FILENAME= restart.dat
364 %
365 % Restart adjoint input file
366 SOLUTION_ADJ_FILENAME= restart_adj.dat
367 %
368 % Files to output
369 % Possible formats : (TECPLOT_ASCII, TECPLOT, SURFACE_TECPLOT_ASCII,
370 % SURFACE_TECPLOT, CSV, SURFACE_CSV, PARAVIEW_ASCII, PARAVIEW_LEGACY, SURFACE_PARAVIEW_ASCII,
371 % SURFACE_PARAVIEW_LEGACY, PARAVIEW, SURFACE_PARAVIEW, RESTART_ASCII, RESTART, CGNS,
    SURFACE_CGNS, STL_ASCII, STL_BINARY)
372 % default : (RESTART, PARAVIEW, SURFACE_PARAVIEW)
373 OUTPUT_FILES= (RESTART, PARAVIEW, SURFACE_PARAVIEW)
374 %
375 % Output file convergence history (w/o extension)
376 CONV_FILENAME= history
377 %
378 % Output file restart flow
379 RESTART_FILENAME= restart.dat
380 RESTART_ADJ_FILENAME= restart_adj.dat
381 %
382 % Output file flow (w/o extension) variables
383 VOLUME_FILENAME= volume
384 %
385 % Output file surface flow coefficient (w/o extension)
386 SURFACE_FILENAME= surface
387 OUTPUT_WRT_FREQ = 50

```

**Listing 1 Configuration file in the radial-based optimization procedure.**

# BIBLIOGRAPHY

- [1] J. Wang, *Theory of flow distribution in manifolds*, [Chemical Engineering Journal](#) **168**, 1331 (2011).
- [2] B. Bajura and E. Jones Jr., *Flow distribution manifolds*, in *Gas Turbine and Fluids Engineering Conference* (1976).
- [3] M. Pan, Y. Tang, L. Pan, and L. Lu, *Optimal design of complex manifold geometries for uniform flow distribution between microchannels*, [Chemical Engineering Journal](#) **137**, 339 (2008).
- [4] S. H. Choi, S. Shin, and Y. I. Cho, *The effect of area ratio on the flow distribution in liquid cooling module manifolds for electronic packaging*, [International Communication in Heat and Mass Transfer](#) **20**, 221 (1993).
- [5] Y. Jiang, W. H. Alawee, F. A. Essa, A. s. Abdullah, Z. M. Omara, H. Ahmad, R. Ali, F. Wang, and Y. Menni, *Effect of area ratio and reynolds number on the distribution of discharge in dividing manifold*, [International Journal of Low-Carbon Technologies](#) **17**, 1271 (2022).
- [6] S. H. Choi, S. Shin, and Y. I. Cho, *The effect of the reynolds number and width ratio of the flow distribution in manifolds of liquid cooling modules for electronic packaging*, [International Communication in Heat and Mass Transfer](#) **20**, 607 (1993).
- [7] O. Tonomura, S. Tanaka, M. Noda, M. Kano, S. Hasebe, and I. Hashimoto, *Cfd-based optimal design of manifold in plate-fin microdevices*, [Chemical Engineering Journal](#) **101**, 397 (2004).
- [8] D. Kim, C.-H. Yu, S. H. Yoon, and J. S. Choi, *Effects of manifold geometries on flow distribution to parallel microchannels*, [Journal of Mechanical Science and Technology](#) **25**, 3069 (2012).
- [9] S. Kim, E. Choi, and Y. I. Cho, *The effect of header shapes on the flow distribution in a manifold for electronic packaging applications*, [International Communication in Heat and Mass Transfer](#) **22**, 329 (1995).
- [10] V. V. Dharaiya, A. Radhakrishnan, and S. G. Kandlikar, *Evaluation of a tapered header configuration to reduce flow maldistribution in minichannels and microchannels*, in [ASME 2009 7th International Conference on Nanochannels, Microchannels and Minichannels](#) (2009) pp. 771–777.
- [11] J. C. K. Tong, E. M. Sparrow, and J. P. Abraham, *Geometric strategies for attainment of identical outflows through all of the exit ports of a distribution manifold in a manifold system*, [Applied Thermal Engineering](#) **29**, 3552 (2009).
- [12] H. Yang, Y. Wang, X. Meng, D. Li, and X. Cai, *Guidelines for design of dividing manifolds with discharge uniformly distributed at different positions along the device axis*, [Journal of Fluids Engineering](#) **142** (2020), 10.1115/1.4044984.
- [13] J. M. Jackson, M. L. Hupert, and S. A. Soper, *Discrete geometry optimization for reducing flow non-uniformity, asymmetry, and parasitic minor loss pressure drops in z-type configurations of fuel cells*, [Journal of Power Sources](#) **269**, 274 (2014).

- [14] S. Kim, *A novel design method of the dividing header configuration using 3d numerical simulation for a heat exchanger with a parallel arrangement*, *Applied Thermal Engineering* **159** (2019), [10.1016/j.applthermaleng.2019.113807](https://doi.org/10.1016/j.applthermaleng.2019.113807).
- [15] H. Liu, P. Li, and J. V. Lew, *Cfd study on flow distribution uniformity in fuel distributors having multiple structural bifurcations of flow channels*, *International Journal of Hydrogen Energy* **35**, 9186 (2010).
- [16] C. Amador, A. Gavriilidis, and P. Angeli, *Flow distribution in different microreactor scale-out geometries and the effect of manufacturing tolerances and channel blockage*, *Chemical Engineering Journal* **101**, 379 (2004).
- [17] I. A. Ghani, N. A. Che Sidik, N. Kamaruzzaman, W. Jazair Yahya, and O. Mahian, *The effect of manifold zone parameters on hydrothermal performance of micro-channel heatsink: A review*, *International Journal of Heat and Mass Transfer* **109**, 1143 (2017).
- [18] J.-Y. Song, S. Senguttuvan, W.-W. Choi, and S.-M. Kim, *Effects of manifold design parameters on flow uniformity in parallel mini-channels*, *International Journal of Mechanical Sciences* **234** (2022), [10.1016/j.ijmecsci.2022.107694](https://doi.org/10.1016/j.ijmecsci.2022.107694).
- [19] G. Xia, J. Jiang, J. Wang, Y. Zhai, and D. Ma, *Effects of different geometric structures on fluid flow and heat transfer performance in microchannel heat sinks*, *International Journal of Heat and Mass Transfer* **80**, 439 (2015).
- [20] C. Anbumeenakshi and M. Thansekhar, *Experimental investigation of header shape and inlet configuration on flow maldistribution in microchannel*, *Experimental Thermal and Fluid Science* **75**, 156 (2016).
- [21] R. K. Shah and D. P. Sekulic, *Fundamentals of Heat Exchanger Design* (John Wiley & Sons, Inc., 2003).
- [22] A. L. London, G. Klopfer, and S. Wolf, *Oblique flow headers for heat exchangers*, *Journal of Engineering for Power* (1968).
- [23] J. Wang and H. Wang, *Discrete method for design of flow distribution in manifolds*, *Applied Thermal Engineering* **89**, 927 (2015).
- [24] L. F. Moody, *Friction factors for pipe flow*, *Transactions of the American Society of Mechanical Engineers* **66**, 671 (1944).
- [25] J. Xie, Y. Shao, Y. Xu, J. Yang, and S. Zhang, *Structural optimizations of u- and z-type manifolds for uniform flow distribution by applying an increaser and baffle plates*, *Chemical Engineering Technology* **38**, 2217 (2015).
- [26] S. Kim, K. Kim, and C. Son, *Optimum arrangements of guide vanes in a combining header and its effect on the performance of a tubular heat exchanger*, *Applied Thermal Engineering* **103**, 1145 (2016).